# Resolving Leads in Sea-Ice Models: New Analysis Methods for Frontier Resolution Arctic Simulations

Modellieren von Meereisrinnen:

Neue Analysemethoden für Arktische Simulationen mit

Extremen Auflösungen

PhD thesis
by

## Nils Hutter

Department 1

Physics and Electrical Engineering

Universität Bremen

April 29, 2019

# Abstract

Sea ice deforms constantly under the forcing of winds and ocean currents. Eventually the ice cover of the Arctic Ocean breaks into a multitude of ice floes. Strips of open ocean, so-called leads, and pressure ridges, where the collision of floes piled up the ice, are found along the floe boundaries. These features have a strong impact on the interaction of sea ice with the atmosphere and the ocean, as they affect heat loss and surface drag. Currently, climate models do not resolve leads and pressure ridges in simulated sea ice fields due to their coarse resolution. They parameterize the effects of leads on the Arctic climate, if at all.

The goal of this thesis is to develop Arctic simulations that reproduce leads sufficiently to be used in climate simulations. By decreasing the horizontal grid-spacing, a numerical ocean sea-ice model is shown to resolve leads explicitly. To test how realistic these lead-resolving sea-ice simulations are, the following research questions are addressed: (1) what are good metrics to evaluate the simulated leads with observational data? (2) Which observed characteristics of sea ice deformation and deformation features are reproduced by the model?

In a first step, the sea ice deformation in a 1-km lead-resolving sea-ice simulation is analyzed with a spatio-temporal scaling analysis. The simulated sea ice deformation is strongly localized in failure zones and dominated by spontaneous fracture. This heterogeneity and intermittency of sea ice deformation shows that the simulation captures the fracture processes that form leads.

In a second step, two new algorithms are described that detect and track leads and pressure ridges, combined into Linear Kinematic Features (LKFs). Both algorithms are applied to deformation data observed from satellite to establish a data set of deformation features that can be used as a reference in model evaluation. LKFs in two lead-resolving sea-ice simulations are ex-

tracted with the same algorithms, and found to agree with the LKF data set with respect to their spatial characteristics and temporal evolutions.

In conclusion, high resolution sea-ice simulations can explicitly resolve leads. These simulations reproduce the characteristics of sea ice deformation and the representation of LKFs that are both observed from satellite. In future work, these simulations could be used as prototypes for the configuration of the sea-ice component in a climate model to directly simulate air-ice-ocean interaction processes in the Arctic.

# Zusammenfassung

Meereis ist ständiger Deformation durch Winde und Ozeanströmungen ausgesetzt, die die Eisdecke des Arktischen Ozeans in eine Vielzahl von Schollen brechen. Zwischen einzelnen Schollen finden sich sowohl langgezogene Streifen offenen Ozeans, auch Meereisrinnen genannt, als auch Presseisrücken, die sich durch das Aufeinanderschieben von Eis bei der Kollision zweier Eisschollen bilden. Meereisrinnen und Presseisrücken sind für die Wechselwirkungen zwischen Eis, Atmosphäre und Ozean von großer Bedeutung, da sie z.B. die Wärmeflüsse und den Strömungswiderstand ändern. Klimamodelle bilden momentan keine Meereisrinnen und Presseisrücken ab, da ihre Auflösung zu niedrig ist. Wenn überhaupt beschreiben sie diese Effekte durch Parameterisierungen.

Das Ziel dieser Arbeit ist eine Arktische Simulation zu entwickeln, die Meereisrinnen abbildet und in Klimamodellen verwendet werden könnte. Durch Reduzieren der horizontalen Gitterweite können numerische Ozean-Meereismodelle Meereisrinnen explizit auflösen. Wie realistisch diese rinnenauflösenden Meereissimulationen sind, wird in folgenden Forschungsfragen bearbeitet: (1) Was sind geeignete Methoden um die simulierten Meereisrinnen mit Beobachtungsdaten zu vergleichen? (2) Wie gut werden Meereisdeformation, Meereisrinne und Presseisrücken im Modell wiedergegeben?

Meereisdeformation wird in einer rinnenauflösenden Meereissimulation mit einer Gitterweite von 1 km simuliert und auf räumliche und zeitliche Skalierung hin untersucht. Die simulierte Meereisdeformation zeichnet sich durch starke Lokalisierung und spontanes Bruchverhalten aus. Die nachgewiesene Heterogenität und Intermittenz von Meereisdeformation zeigt, dass das Modell in der Lage ist die Bruchprozesse, die Meereisrinnen bilden, korrekt darzustellen.

Im nächsten Schritt werden zwei neue Algorithmen beschrieben, die Meereisrinnen und Presseisrücken zu Linear Kinematic Features (LKFs) zusam-

menfassen, diese in Satellitendaten filtern und über ihre gesamte Lebenszeit verfolgen. Satellitengestützte Meereisdeformationsdaten werden mit Hilfe beider Algorithmen prozessiert, um einen LKF-Datensatz zur Modellevaluation zu erstellen. Die LKFs in zwei rinnenauflösenden Meereissimulationen werden mit diesen Algorithmen erfasst. Diese stimmen mit dem LKF Datensatz hinsichtlich räumlich und zeitlicher Eigenschaften von LKFs weitestgehend überein.

Als Fazit dieser Arbeit bleibt, dass hohe Auflösungen ein Abbilden von Rinnen in Meereismodellen ermöglichen und damit die in Satellitendaten beobachteten Eigenschaften von Meereisdeformation wiederzugeben. In Weiterführung dieser Arbeit könnten diese rinnenauflösenden Meereissimulationen in Klimamodelle integriert werden, um damit Wechselwirkungen zu simulieren, die eng mit Meereisrinnen verbunden sind.

# Contents

# 1. Introduction

*"The ice grew worse and worse, and we got no way.
Ridge after ridge, and nothing but rubble to travel
over. ... It was a veritable chaos of ice-blocks,
stretching as far as the horizon."*

Fridtjof Nansen in Nansen (1897)

The North Pole has been one of the last unvisited spots on Earth that cast
its spell on humans. The North Pole is located in a sea — the Arctic Ocean.
The surface of the Arctic Ocean is frozen due to the low temperatures, form-
ing a layer of ice. Around the beginning of the 20th century courageous ad-
venturers with bold ideas headed North, and were challenged by the extreme
environment and the harsh weather conditions. Fridtjof Nansen and his com-
panion Hjalmar Johansen had traveled with their ship "Fram" 18 month with
the ice[1], before they left it behind in March 1895 to begin their march to
the pole. The first few days they were able to ski on flat ice, however as
they expand into the ice, skiing conditions became worse. After 25 days of
travel, Nansen and Johansen were facing strongly deformed ice that Nansen
described in the citation above on the evening before they needed to turn
back. The ice was piled up in long ridges such strongly as a results of sea ice
deformation that a passage further North was impossible.

Sea ice deformation is driven by wind and ocean currents that exert drag
forces on the ice. These forces move[2], deform, and eventually break the

---

[1]Fram drifted frozen in the ice from the New Siberian Islands to Spitzbergen, but
missed the Pole by 450 km (Nansen, 1897).

[2]Nansen, actually, made use of this wind-driven motion. Dominant wind patterns
drive an ice circulation from the East Siberian Sea across the North Pole to Fram Strait.
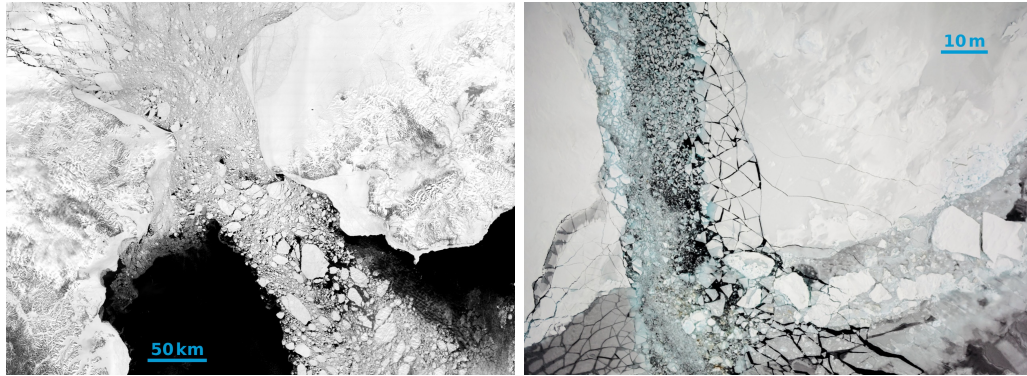This ice stream is called Transpolar drift.

**Figure 1.1:** Sea ice floes at different scales in: **(left)** a satellite image of the Bering Strait captured by MODIS in May 2000 (*NASA earth observatory*[3]), and **(right)** an areal photo of ice floes in the Weddel Sea (*Stefan Hendricks/IceCam*).

ice into a multitude of ice floes. The size of these floes ranges from a few decimeters to multiple kilometers (Fig. 1.1). In converging ice motions, the collision of floes piles up the ice along the floe boundary and so-called pressure ridges are formed. In contrast, floes are pushed apart after failure in diverging forcing conditions and stripes of open ocean are exposed. These narrow regions where the ocean is not covered by ice are referred to as leads. The result of deformation is omnipresent in the ice cover in forms of floes, leads, and pressure ridges.

The fact that sea ice is an agglomeration of floes alters its interaction with other climate components, such as the ocean and the atmosphere. During wintertime, sea ice acts as an insulator between the warm ocean and the cold atmosphere. Thereby, sea ice and especially its snow cover progressively reduce the growth rate of ice as it gets thicker. In a lead the ocean is in direct contact with the atmosphere, so that strong heat loss is initiated and consequently new ice is formed. The dark ocean in a lead absorbs more short-wave radiation than bright ice caused by the lower albedo of open ocean. A comparably warmer ocean and the lateral melting along the floe boundary accelerates the erosion of the ice floes in summer (Horvat *et al.*, 2016). This feedback accelerates the retreat of the ice edge when the swell of Arctic storms is breaking the ice (Asplin *et al.*, 2012). In addition, short-wave radiation penetrating the ocean is a source of energy for primary production (Nomura *et al.*, 2018). Furthermore, pressure ridges have also an effect on Arctic climate system: (1) pressure ridges increase the surface and

---

[3]https://earthobservatory.nasa.gov/images/657/ [Status: 25.3.2019]

underwater roughness of sea ice, which consequently alters the form drag (Arya, 1973; Tsamados *et al.*, 2014), (2) snowdrifts form near pressure ridges (Iacozza & Barber, 1999), and (3) the keels of pressure ridges are grounded in shallow regions of the Arctic Basin, so that stable and immobile ice along the coast, so-called fast-ice, is formed (Mahoney *et al.*, 2007; Lemieux *et al.*, 2015).

The role of sea ice changes in the context of global warming. The surface temperature in Arctic regions rises two times faster than the global average, which is referred to as Arctic amplification. Higher temperatures have lead to a rapid decrease in the Arctic sea ice extent over the past decades. In the period from 1979 to 2012 the minimum sea ice extent in September dropped by more than 30 % (Stroeve *et al.*, 2012) and the sea ice volume reduced by even 70-80 % (Overland & Wang, 2013). The thinning results in weaker ice that is more prone to deformation. Indeed, the mean drift of sea ice is accelerated by 17 % in winter and 8.5 % in summer, in conjunction with an increase in deformation rates of 50 % between 1979 and 2007 (Rampal *et al.*, 2009). The increased fracturing of the ice cover drives a further retreat of the ice cover because increased absorption of short-wave radiation and lateral melting intensify the melting of the sea ice. The Arctic Ocean is expected to become ice-free during summer within the first half of the 21st century (Overland & Wang, 2013).

The opening of the Arctic Ocean is "not just the best opportunity of our generation, but of the last 12,000 years"[4] says Scott Minerd, the chief investment officer of a large global investment and advisory firm[5]. He referred to the increasing economic interest in the Arctic caused by the decline of sea ice coverage such as: (1) shipping through the North Sea Route or the Northwest passage will be feasible under climate change conditions (Smith & Stephenson, 2013) and Arctic shipping increases already today (Eguíluz *et al.*, 2016). (2) Considerable amounts of the global oil and gas resources hide underneath the Arctic Ocean (Bird *et al.*, 2008). (3) Arctic tourism is growing (Hall & Saarinen, 2010; Maher, 2017). These economic activities and the Arctic climate change have a strong impact on indigenous communities and the Arctic environment and wildlife. Thus, reliable forecast systems of

---

[4]The Sydney Morning Herald, May 3rd 2014, `https://www.smh.com.au/business/arctic-investment-the-best-opportunity-of-last-12000-years-20140502-37lv2.html` [Status: 26.3.2019]

[5]Guggenheim Partners LLC, `https://www.guggenheimpartners.com` [Status: 20.4.2019]

the polar regions are strongly needed, but those currently lag behind the skill of mid-latitude forecasts due to lack of observational data (Jung *et al.*, 2016). Skillful sea-ice predictions are useful for shipping but also they are required to fully capture the impact of sea-ice on weather forecasts (Jung *et al.*, 2016; Chevallier *et al.*, 2019). The forecasting community has so far mainly focused on seasonal to decadal time-scales (Guemas *et al.*, 2016) and Pan-Arctic metrics like minimum sea-ice extent in September (Stroeve *et al.*, 2014). While such forecasts might be of interest for longterm strategic planning, necessary daily forecast of sea ice are still in the exploratory stage. Especially, short-term forecasts of regional drift, leads, and ice pressure are of particular relevance for Arctic shipping.

In summary, floes, leads, and pressure ridges are distinct features of sea ice that play a leading role in the atmosphere-ice-ocean interaction and are prerequisites for improving short-term regional sea-ice forecasts. In this thesis, I focus on the potential of state-of-the-art sea-ice models to resolve leads in sea ice and present different methods to evaluate these features. The remainder of this introduction provides a brief overview of the sea-ice observations, the sea-ice modeling, and the evaluation of sea-ice models, all three with a focus on sea-ice deformation features, followed by an outline of the scope and structure of this thesis.

## 1.1 Sea ice observations

The earliest sea-ice models were mostly constraint by in-situ observations on sea ice. Large field campaigns like the Arctic Ice Dynamics Join Experiment (AIDJEX) offered new insights and process understanding of the dynamics and thermodynamics of ice. Nowadays, in-situ observations are still essential to fill knowledge gaps and for ground-truthing of remotely sensed data. The large spatial and temporal coverage of satellite data allow us to evaluate and adjust parameters in large-scale simulations. In the following section, I summarize satellite-based data sets of leads and sea ice deformation that could be useful to evaluate lead-resolving sea-ice simulations.

The small width of leads and pressure ridges hinders their observation from space. Leads can be extracted by separating the thin stripes of open ocean from sea ice in very high resolution satellite imagery. First data sets were derived by hand-picking leads in visible range imagery (Walter & Over-

land, 1993; Miles & Barry, 1998) or automated detection of open-water pixels in advanced very high resolution radiometer (AVHRR) (Lindsay & Rothrock, 1995) and SAR imagery (Banfield, 1992; Van Dyne & Tsatsoulis, 1993; Van Dyne *et al.*, 1998). These data set are case-studies with limited use for model evaluation due to their small coverage in space and time. The combination of fully automated detection algorithms with the continuous acquisition of satellite imagery enables us to derive long-term data sets of leads from passive microwave (Röhrs & Kaleschke, 2012; Bröhan & Kaleschke, 2014), thermal (Willmes & Heinemann, 2016), and radar altimeter data (Wernecke & Kaleschke, 2015). Recently, attempts have been made to detect leads directly from SAR-images (Murashkin *et al.*, 2018). All data sets provide estimates of lead densities, while some studies also yield lead orientations (Miles & Barry, 1998; Bröhan & Kaleschke, 2014) and lead widths (Lindsay & Rothrock, 1995; Wernecke & Kaleschke, 2015).

While the studies above identified leads as open ocean, the second method to obtain lead observations is based on the dynamic origin of leads and pressure ridges. Sea-ice deformation is derived from high resolution sea ice drift fields. Leads and pressure ridges are marked by high deformation dates. Due to their elongated shape they are referred to as Linear Kinematic Features (LKFs). Sea ice drift is determined by cross-correlating tracking points in two consecutive SAR images (Kwok, 2010). Deformation events are recorded in the relative displacement of the tracked points. These imprints are independent of the width of the deformation zone. SAR images offer the high spatial resolution that is needed to provide drift estimates at 10-km resolution. In addition, they are not restricted by poor weather or nighttime. The first operational deformation data set of this kind was the RADARSAT geophysical processor system (RGPS, Kwok, 1998) covering the Amerasian basin of the Arctic Ocean during the years 1996 to 2008. This data set was continued using ENVISAT SAR data in the ENVISAT Geophysical Processor System (EGPS)[6] and GlobICE[7] for years 2007 to 2012. A follow-up operational data set is based on Sentinel-1 SAR images (Pedersen *et al.*, 2015). The temporal sampling rate of these data sets is limited by the repeat cycle of the satellite, i.e. the time until the satellite overflies the same point, which

---

[6]Arctic and Antarctic ice drift from Envisat is available at `http://rkwok.jpl.nasa.gov/envisat/index.html` [Status: 8.4.2019] and the derivation of the data set is funded by NASAs MEaSUREs program.

[7]GlobICE - Sea ice dynamics for climate research: `http://www.globice.info/index.php` [Status: 8.4.2019]

is 3 days for RGPS and GlobICE and 1 day for EGPS and Sentinel data. Drift estimates at higher sampling rate of 10 min are recorded by ship radars (Oikkonen *et al.*, 2017) but the spatial coverage is limited to the vicinity of the ships. Buoy records of the International Arctic Buoy Program (IABP) also provide drift information at high sampling rates of 1 hour. These data cover the entire Arctic and reach back until 1979 but have a sparse coverage, which makes a direct retrieval of deformation data difficult.

## 1.2 Sea ice modeling

Sea ice models describe the relevant processes that determine the evolution of sea ice by a set of mathematical equations. The first numerical sea-ice model was a 1D-models that described the thermodynamics of a column of ice, that is the heat transport through the ice and snow and the melting and freezing of the ice (Maykut & Untersteiner, 1971). To date thermodynamic sea-ice models are still the previously described column models with most of them including more detailed descriptions, such as considering melt ponds (Taylor & Feltham, 2004) or adding a vertically variable salinity profile (Turner & Hunke, 2015). Following AIDJEX, Coon *et al.* (1974) introduced the first dynamic sea-ice model that was able to describe the motion and deformation of sea-ice due to external forces. In the following section I introduce the dynamical part of sea-ice models, which will have a special relevance in the remainder of this thesis. For a full review on sea-ice modeling — thermodynamics and dynamics— I refer the interested reader to Hunke *et al.* (2010), Leppäranta (2011), and Lemieux *et al.* (2017).

Generally, two different approaches exist to model the dynamics of sea ice as a multitude of ice floes: (1) the motion of individual floes and their interaction are simulated individually in so-called discrete element sea-ice models (Hopkins & Thorndike, 2006; Herman, 2016). (2) Sea-ice is described as a continuum with material properties representative of the agglomeration of floes in a certain control volume, e.g. a grid cell in the model (Coon *et al.*, 1974; Hibler, 1979). Nowadays, sea-ice models based on the continuum assumption are used widely in Global Climate Models (GCMs) due to their numerical efficiency. Discrete element models are computationally expensive and challenging to initialize. Thus, they are mainly used in regional studies or idealized set-ups, e.g. to study ice-wave interaction (Herman, 2017). In

the following, I describe the details of sea-ice models that use the continuum assumption.

The contrast between the sea-ice thickness of a few meters and the basin-scale extent of sea ice motivates the second major assumption made by these model (besides the continuum assumption): sea ice can be described as a vertically integrated 2D continuum where vertical heterogeneity in the ice are negligible for dynamical processes. The momentum balance of sea ice reads as follows,

$$m\left(\frac{D\mathbf{u}}{Dt}\right) = -mf\mathbf{k} \times \mathbf{u} + \tau_a + \tau_o - mg\nabla H + \nabla \cdot \boldsymbol{\sigma}, \qquad (1.1)$$

where the left hand side describes the change in momentum of the ice with $m$ as the mass per unit area of the ice and the horizontal ice velocity $\mathbf{u}$. On the right hand side all forces acting on the ice are summarized: the Coriolis force (Coriolis parameter $f$ and unit vector normal to the surface $\mathbf{k}$), the atmospheric $\tau_a$ and oceanic stress $\tau_o$, the gravitational force due to the surface tilt (gravitational constant $g$ and the surface height $H$), and the ice interaction force given by the divergence of the internal stress tensor $\boldsymbol{\sigma}$ (Hibler, 1979; Feltham, 2008).

The rheology of sea ice describes how the ice deforms under given forces and thereby links the ice velocity to the internal stress in the ice. Nonlinear plastic rheologies are most commonly used to describe the material properties of sea ice. Coon *et al.* (1974) introduced an elastic-plastic rheology stating that the ice deforms elastically until the forcing stress reaches the ice strength, in which case the deformation turns plastic. Hibler (1979) proposed a viscous-plastic (VP) rheology, which has been widely adopted in GCMs due to its numerical efficiency. This rheology consists of (1) a constitutive law that relates stress and deformation rates and allows for viscous and plastic deformation, (2) an elliptical yield curve that encloses all stress states that lead to viscous deformation, while stress states on the ellipse lead to plastic deformation, and (3) a normal flow rule directing plastic deformation perpendicular to the yield curve. The ice strength is isotropic, i.e. independent of the direction of external forces, and depends on the gradual coverage of a grid cell with ice and its mean thickness. These assumptions were made having large grid cells of the order of $100 \times 100$ km size in mind such that each contains a large amount of floes and leads in all directions.

Classical VP models are successful in representing sea-ice fields at large

and medium resolution up to 10 km. These coarse resolutions, however, are not sufficient to resolve the small-scale variation of velocity fields that are the imprint of leads and pressure ridges (Lindsay *et al.*, 2003; Coon *et al.*, 2007; Kwok *et al.*, 2008). Various modifications to this rheology have been suggested to improve the representation of sea-ice deformation, most of which were based on changing the shape of the yield curve. New rheologies address especially the preferred deformation along existing leads and weaknesses in the ice: an anisotropic rheology (EAP) (Wilchinsky & Feltham, 2004), a elastic-decohesive rheology (Schreyer *et al.*, 2006), or most recently a Maxwell elasto-brittle rheology (MEB) (Dansereau *et al.*, 2016).

In addition to changes in the rheology, two parameterization handle pressure ridges and the floes in sea-ice models implicitly. The thickness of Arctic sea ice shows a wide range from thin first-year ice (centimeters to decimeters) to thicker multi-year ice (meters) to thick pressure-ridges (around ten meters). In areas as small as a model grid cell, all of these types can be present. The VP-model of Hibler (1979), however, divided a grid-cell only in fractions of open-water and ice with one mean thickness. In contrast, an active Ice Thickness Distribution (ITD) allows for more ice thickness classes, such that all ice types are described. Dynamic processes as divergence and convergence and thermodynamic processes as melting and freezing alter the ITD and redistribute the ice between the different classes (Thorndike *et al.*, 1975; Lipscomb *et al.*, 2007). Similarly to its variety in ice thicknesses, a grid cell also contains floes of different sizes. This floe size distribution (FSD) can also be parameterized to account for floe-size dependent interaction processes, e.g. lateral melting and wave fracturing (Horvat & Tziperman, 2015; Roach *et al.*, 2018).

Independently of these improvements in modeling the underlying physical processes, horizontal grid spacing of climate models is decreasing towards scales that start to resolve large floes and leads. In fact, VP models have the potential to simulate linear failure lines for a grid spacing smaller than $\sim 5$ km (Hunke *et al.*, 2010; Losch *et al.*, 2014; Hutter, 2015; Wang *et al.*, 2016). In spite of this potential, it is still unclear if any of these sea ice simulations that explicitly resolve large floes and leads are realistic and reproduce observed characteristics of sea ice. It is also unknown which modifications to the model are needed for lead-resolving sea-ice simulations given the large variety of suggested methods.

8

## 1.3 Evaluation of sea-ice models

Systematic evaluations of sea-ice models have been based on the comparison of large-scale fields like sea ice concentration, thickness, and drift (e.g., Nguyen *et al.*, 2011a; Massonnet *et al.*, 2014; Ungermann *et al.*, 2017). Continuous fields allow for direct point-by-point comparisons of observations and model outputs. Leads and pressure ridges mark discontinuities in sea-ice fields that are not necessary co-located in observations and models due to the chaotic nature of sea-ice fracture. Thus, other means of comparison are required for the evaluation of these features (Coon *et al.*, 2007).

First simulations showing deformation features have been compared to observations by qualitative description based on visual inspection (Kwok *et al.*, 2008) and by assessing the intersection angle of LKFs (Hutchings *et al.*, 2005). Due to the lack of more quantitative methods, the focus has changed to statistical methods that evaluate the strong localization of sea-ice deformation along LKFs (Girard *et al.*, 2009). These metrics make use of the multi-fractal characteristics of sea-ice deformation in space and time and determine their degree of heterogeneity and intermittency. These methods provide detailed information on sea-ice deformation, but direct inferences about specific characteristics of LKFs are not straightforward.

The position and the temporal evolution of individual LKFs is needed to deduce and compare specific properties of LKF, such as their length or lifetime. The visual extraction of leads previously used to describe their orientation in a regional study (Miles & Barry, 1998) is not feasible in the context of large-scale model-observations comparison. The automated detection of LKFs is in an exploratory phase (Linow & Dierking, 2017), but promises to process large amounts of data and allow for a comprehensive description of LKFs.

## 1.4 Scope and Structure of this thesis

In this thesis I study the potential of sea-ice models using the classic VP rheology to resolve leads at very high resolution. Here, very high resolution refers to simulations having a grid spacing of 1 and 2 km. State-of-the-art climate simulations use a grid spacing that is one magnitude larger, but my choice of resolution is meant to be representative of next-level sea-ice

simulations in the upcoming years. I focus on the VP rheology as it is used in most climate models. The overall aim of this thesis is to present lead-resolving sea-ice simulations in a framework that is easily adoptable to current climate models and to focus on the thorough evaluation of this kind of simulations. In doing so, I analyze sea-ice deformation — the driver of failure in the ice — as well as leads and pressure ridges that are the result of fracturing ice. The latter affect many interactions processes in the Arctic climate system and are thus of special relevance in climate simulations.

In a first step, I investigate whether sea-ice models using VP-rheology simulate leads in high resolution set-ups and how the explicitly resolved leads change the sea-ice deformation fields. I show that sea-ice deformation concentrates along resolved fracture lines for sufficiently high model resolution. By means of a spatio-temporal scaling analysis, I test for the heterogeneity and intermittency of sea-ice deformation, which describes how strongly deformation is localized in failure zones and how irregular the timing of fracture events is. Both characteristics are prerequisites for any deformation feature to be resolved in a physically realistic way. A proper spatial distribution and temporal evolution of leads and pressure ridges is essential to simulate interaction processes in climate models, but these characteristics are not validated by a scaling analysis of sea-ice deformation.

In a second step, I explore new ways to evaluate specific characteristics of deformation features directly. I outline an algorithm that detects leads and pressure ridges in sea-ice deformation data and present a method to track the detected features using drift data. Both algorithms are new. I then apply my algorithms to the RGPS data set to derive a large-scale reference data set of LKFs that can be used in model evaluations. Spatial and temporal characteristics of LKFs, e.g. length, density, or lifetime, are derived from the RGPS LKF data set. This allows for the first time a comprehensive description of deformation features.

Finally, I investigate if the extracted LKFs can discriminate between the realism of different model simulations and hence, if extracting LKFs is a valuable tool for model evaluation. To this end, two simulations, one using an active ITD model and one using the classical two ice-class VP-model, are compared with the RGPS LKF data set regarding the spatial and temporal characteristics of simulated LKFs. I compare the results to a multi-fractal scaling analysis testing whether the presented method provides insights complementary to established evaluation methods. With the combination of the

LKF statistics and the scaling analysis I show that deformation and LKFs are realistic in my simulations. These simulations can be used in next-level climate models to explicitly resolve leads and pressure ridges and simulate related interaction processes.

The key research questions addressed in this thesis can be summarized in the following way:

**Key research questions and goal**

- **Q1**: Can leads and individual floes be resolved with current sea-ice model that use the continuum assumption?

- **Q2**: Which aspects of sea ice deformation are reproduced in lead-resolving sea-ice simulations, i.e. do they capture the fracture processes that form leads and pressure ridges correctly?

- **Q3**: What are good metrics to evaluate simulated leads and pressure ridges with observational data given the chaotic nature of ice fracture?

- **Goal**: Present a simulation that reproduces leads and pressure ridges sufficiently to be used in forceasting systems and to study interaction processes in climate simulations.

The thesis is structured as follows: In Chapter 2, I investigate the localization and intermittency of sea-ice deformation in a 1-km lead-resoving sea-ice simulation to test for an realistic representation of ice fracture. For this purpose, I perform a spatio-temporal scaling analysis of the simulated sea-ice deformation as well as of satellite observations, and compare their results. Chapter 2 has been published in the *Journal of Geophysical Research: Oceans* by Hutter, N., Losch. M. & Menemenlis, D. (2018) under the title *'Scaling Properties of Arctic Sea Ice Deformation in a High-Resolution Viscous-Plastic Sea Ice Model and in Satellite Observations'*.

In Chapter 3, I develop two algorithms that detect leads and pressure ridges in sea-ice deformation data and track them using drift information.

Both algorithms are applied to the RGPS data set to establish a Pan-Arctic LKF dataset covering the winters from 1996 to 2008 (Hutter *et al.*, 2019). This analysis enables a comprehensive description of LKFs. Chapter 3 has been published in the journal *The Cryosphere* by Hutter, N., Zampieri, L. & Losch, M. (2019) under the title *'Leads and ridges in Arctic sea ice from RGPS data and a new tracking algorithm'*. Both algorithms are open source and publicly available on github (`https://github.com/nhutter/lkf_tools.git`, Hutter, 2019).

In Chapter 4, the LKF detection and tracking algorithms are applied to two 2-km simulations, where one uses an ITD parametrization and the other the classical two ice class model. The spatial and temporal statistics of LKFs are outlined and used to compare the detected and tracked LKFs with the RGPS data set. In doing so, I test how adapting the description of the different physical processes that govern sea-ice strength improves the representation of LKFs. Chapter 4 has been submitted to the journal *The Cryosphere* by (Hutter & Losch, 2019) under the title *'Feature-based comparison of sea-ice deformation in lead-resolving sea-ice simulations'*.

In Chapter 5, I summarize the main results of this thesis, draw conclusions, and give an outlook for possible future work.

**Remark** Chapters 2, 3, and 4 constitute unaltered papers which I have compiled together with my co-authors. Their individual contributions are acknowledged at the beginning of the respective chapters. I decided to retain the original manuscripts as published/submitted resulting in small inconsistencies with the rest of this thesis regarding style, utilization of the first person plural, and abbreviations.

# 2. Scaling properties of Arctic sea ice deformation in a high-resolution viscous-plastic sea ice model and in satellite observations[1]

**Abstract** Sea ice models with the traditional viscous-plastic (VP) rheology and very small horizontal grid spacing can resolve leads and deformation rates localized along Linear Kinematic Features (LKF). In a 1-km pan-Arctic sea ice-ocean simulation, the small scale sea-ice deformations are evaluated with a scaling analysis in relation to satellite observations of the Envisat Geophysical Processor System (EGPS) in the Central Arctic. A new coupled scaling analysis for data on Eulerian grids is used to determine the spatial and temporal scaling and the coupling between temporal and spatial scales. The spatial scaling of the modeled sea ice deformation implies multi-fractality. It is also coupled to temporal scales and varies realistically by region and season. The agreement of the spatial scaling with satellite observations challenges previous results with VP models at coarser resolution, which did not reproduce the observed scaling. The temporal scaling analysis shows that the VP model, as configured in this 1-km simulation, does not fully resolve the intermittency of sea ice deformation that is observed in satellite data.

## 2.1   Introduction

Oriented fractures scatter Arctic sea ice in all seasons. They divide the ice cover into many ice floes and narrow lineaments of open water (Marko & Thomson, 1977; Kwok, 2001; Richter-Menge *et al.*, 2002). The fragmentation of ice is caused by stress resulting from surface wind associated with weather systems, ocean eddies, geometric boundaries such as the coastline or a fast ice edge (Richter-Menge *et al.*, 2002), tides (Holloway & Proshutinsky, 2007), ocean waves (Squire *et al.*, 1995), or swell originating from Arctic storms (Asplin *et al.*, 2012). Convergent motion in the ice pack forms pressure ridges whereas stripes of open ocean, so-called leads, develop during divergent motion. These narrow and long structures are often referred to as Linear Kinematic Features (LKF) due to their formation by the kinematic processes: opening, closing, and shear (Kwok, 2001).

Systems of leads in Arctic sea ice are observed across all scales from aerial photographs to satellite images — pointing to self-similar properties (or a fractal structure) of sea ice. This impression is supported by the floe size distribution following a power-law scaling (Rothrock & Thorndike, 1984).

Power-law scaling was also observed in lead width distributions (Lindsay & Rothrock, 1995), in fracture and faulting of sea ice (Weiss, 2003), and in sea ice deformation (Marsan *et al.*, 2004; Rampal *et al.*, 2008; Stern & Lindsay, 2009).

The mean total deformation $\dot{\epsilon}_t$ at the spatial scale $L$ was found to follow a power-law,

$$\langle \dot{\epsilon}_t^q (L) \rangle \sim L^{-\beta(q)}, \tag{2.1}$$

with a scaling exponent $\beta(q)$, which is a quadratic function of the order of moment $q$ ranging from 0.5 to 3 (Marsan *et al.*, 2004). The quadratic shape of $\beta(q)$ suggests multi-fractal characteristics of sea ice deformation (Marsan *et al.*, 2004). Typical values for the first order moment scaling coefficient around $\beta(1) \sim 0.2$ for deformation rates were derived from satellite data (Marsan *et al.*, 2004; Girard *et al.*, 2009; Stern & Lindsay, 2009) and from buoy data (Hutchings *et al.*, 2011) in winter time. The spatial scaling exponent follows a seasonal cycle mainly driven by the varying ice strength. It increases during summertime as a result of weaker summer ice being more prone to local deformation (Stern & Lindsay, 2009).

In addition to spatial scaling properties, temporal scaling properties and a coupling between temporal and spatial scaling exponents were found for sea ice deformation derived from the dispersion of buoys:

$$\langle \dot{\epsilon}_d (L, \tau) \rangle \sim L^{-\beta(\tau)} \sim \tau^{-\alpha(L)}, \tag{2.2}$$

where the temporal scaling exponent $\alpha(L)$ depends on the spatial scale $L$ and the spatial scaling exponent $\beta(\tau)$ on the temporal scale $\tau$ (Rampal *et al.*, 2008; Marsan & Weiss, 2010; Oikkonen *et al.*, 2017). A review on scaling properties of sea ice deformation can be found in Weiss & Dansereau (2017).

Scaling analyses are a useful tool for evaluating small-scale sea ice deformation produced by sea ice models (Girard *et al.*, 2009; Bouillon & Rampal, 2015b; Rampal *et al.*, 2016) because they quantify the strong localization of deformation in space (heterogeneity) and in time (intermittency), which can then be compared to the observed localization in satellite (Marsan *et al.*, 2004; Stern & Lindsay, 2009; Herman & Glowacki, 2012) and buoy data (Rampal *et al.*, 2008; Hutchings *et al.*, 2011, 2012; Oikkonen *et al.*, 2017). The scaling characteristics and multi-fractality of deformation rates in a VP model with 12-km horizontal grid spacing have been found to significantly

disagree with the scaling laws that were estimated from satellite data and buoy trajectories (Girard *et al.*, 2009), even though VP models can realistically represent the large-scale sea ice drift velocity fields (Lindsay *et al.*, 2003; Kwok *et al.*, 2008). Girard *et al.* (2009) attributed this disagreement to the fact that the extreme localization of large deformation rate events, such as structural failure on sub-grid scale, is not properly represented by the VP rheology.

Girard *et al.* (2011) introduced the elasto-brittle (EB) rheology, previously used in rock mechanics simulations, in order to improve the physical representation of the brittle behavior of sea ice by including a sub-grid scale damage parameter and elastic interaction in a sea ice models. The EB rheology reproduces the strong localization in space (heterogeneity) (Girard *et al.*, 2011) and in time (intermittency) (Rampal *et al.*, 2016). It has been shown to be practical in a dynamical and thermodynamical sea ice model (Rampal *et al.*, 2016) and, especially with the extension to the Maxwell elasto-brittle rheology (Dansereau *et al.*, 2016), this rheology has the potential to improve the modeling of LKFs in coupled climate models.

Independently of these improvements in sea-ice rheology, horizontal grid spacing of climate models is decreasing towards scales that start to resolve large leads. In fact, VP sea ice model solutions show linear failure lines for a grid spacing smaller than $\sim 5\,\text{km}$ (for example Fig. 2 in Losch *et al.*, 2014). Further, Wang *et al.* (2016) compared different satellite products with sea ice model solutions obtained with an elastic-viscous plastic (EVP) rheology solver at 4.5-km grid spacing and at first glance found agreement in the regional and seasonal variation of the lead area fraction. There is, however, no thorough evaluation of the spatial and temporal scaling properties at high resolution that would test the characteristic spatial heterogeneity and intermittency of small scale sea ice deformation in these models.

In this paper, we use model results of a sea-ice ocean model with an average grid spacing below $1\,\text{km}$ in the Arctic to study the effect of resolved leads on the scaling properties of sea ice deformation in the VP model. To this end, we implement a scaling analysis, which is a combination of a spatial (Marsan *et al.*, 2004) and a temporal scaling analysis (Rampal *et al.*, 2008; Hutchings *et al.*, 2011) for gridded Eulerian data. In doing so, the spatial and temporal scaling characteristics are computed simultaneously and the coupling between both is determined. For evaluation we use the ENVISAT Geophysical Processor System (EGPS) data set. Furthermore, we examine

the seasonal and regional variability of spatial scaling properties and how they depend on the ice condition, that is, sea ice concentration and thickness.

## 2.2 Model and Observations

### 2.2.1 EGPS Data Set

We use high resolution sea ice drift data from the Envisat Geophysical Processor System (EGPS) for evaluation of the model results. The data is available at `http://rkwok.jpl.nasa.gov/envisat/index.html`. EGPS is the successor of the RADARSAT Geophysical Processor System (RGPS) but it covers different regions (Central Arctic, Canadian Arctic Archipelago, and Ross Sea in Antarctica) and the temporal sampling rate is one day, instead of three days for RGPS. In contrast to RGPS, the EGPS is not provided as an Arctic wide composite but as single drift data sets. Each drift data set is derived from two overlapping SAR images and is provided on a regular grid with 10-km grid spacing. Note that the widely-used RGPS data set has a larger spatial coverage, but is not available for the simulation period.

We compile one sea ice drift and deformation composite from all individual drift data sets in the Central Arctic (see Fig. 2.1) during the period between September 2011 and April 2012. We use the original EGPS grid with a temporal and spatial sampling of 1 day and 10 km on a Polar stereographic projection with a reference latitude of 70°. For each composite day, all data sets that overlap at least in part with the given day of the composite are identified. Strain rates are computed from velocities by finite difference for all those drift data sets and averaged with a weight corresponding to the size of the temporal overlap with the composite day. Because the EGPS data are provided on a regular grid with constant grid spacing within the polar stereographic projection, metric effects can be neglected in the computation of the velocity gradients. The start time and the time span of individual drift data sets can vary, so that one data set can contribute to more than one day in the obtained composite. Similarly, the drift data within one day composite is not necessarily recorded at exact the same time, which leads to slight differences in the mean drift within the velocity fields of the composite.
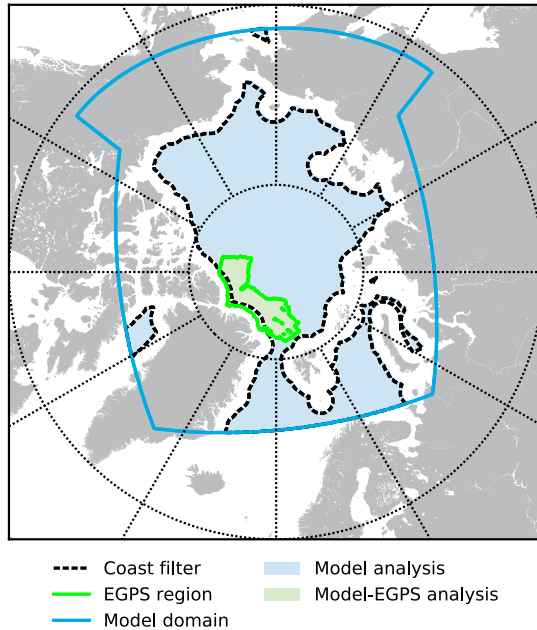
**Figure 2.1:** Model domain, region of EGPS data, and the coastline filter. The analysis regions are shaded (blue for model only analysis and green for model-observation comparison).

## 2.2.2   Model Description

The simulation we analyze is one of a series of so-called global Latitude-Longitude-polar-Cap (LLC; Forget *et al.*, 2015) simulations carried out with the Massachusetts Institute of Technology general circulation model (MITgcm, Marshall *et al.*, 1997; MITgcm Group, 2017). A $\frac{1}{12}^{\circ}$ LLC simulation is initialized on January 1, 2010 from a data constrained $\frac{1}{6}^{\circ}$ simulation provided by the Estimating the Circulation and Climate of the Ocean, Phase II (ECCO2) project (Menemenlis *et al.*, 2008a). The $\frac{1}{12}^{\circ}$ simulation is integrated for one year with ERA-Interim (Dee *et al.*, 2011) surface boundary conditions. On January 1, 2011, surface boundary conditions are switched to the 0.14° ECMWF atmospheric operational model analysis starting in 2011 (European Centre for Medium-Range Weather Forecasts, 2011). All atmospheric fields are provided at 6-hourly intervals and converted to surface fluxes using bulk formulae (Large & Yeager, 2004) and a dynamic-thermodynamic sea ice model (Losch *et al.*, 2010). Starting on January 1, 2011, surface boundary conditions also include tidal forcing for the 16 most significant components, applied as additional atmospheric pressure forcing as in Ponte *et al.* (2015). A $\frac{1}{24}^{\circ}$ LLC simulation is initialized on January 17, 2011 from the $\frac{1}{12}^{\circ}$ simulation and a $\frac{1}{48}^{\circ}$ LLC simulation is initialized on September 10, 2011 from the $\frac{1}{24}^{\circ}$ simulation. In this study, we use model output from the $\frac{1}{48}^{\circ}$ LLC simulation, hereinafter labeled LLC4320, where 4320 refers to the dimension

of the polar cap. The LLC4320 simulation is integrated with 25-s time step and prognostic model variables are saved at hourly intervals. At the time of this study, output was available for the period Sept. 13, 2011 to Oct. 8, 2012.

Published model-data comparisons for the LLC4320 simulation to date are limited to a Drake Passage study (Rocha *et al.*, 2016a), which compared along-track wavenumber spectra of kinetic energy to Acoustic Doppler Current Profiler data, and a Kuroshio Extension study (Rocha *et al.*, 2016b), which established that the upper ocean stratification and variability in that region is well captured by the LLC4320 simulation. This study is the first to examine the LLC4320 model output in the Arctic Ocean, where horizontal grid spacing is a little below 1 km. Bathymetry is from the International Bathymetric Chart of the Arctic Ocean (IBCAO) Version 2.23 (Jakobsson *et al.*, 2008). The sea ice model uses both dynamics and thermodynamics (Losch *et al.*, 2010). Ocean and sea ice parameterizations and parameters are from Nguyen *et al.* (2011b) with the following modifications: (1) the salt-plume parameterization of Nguyen *et al.* (2009) is turned off; (2) the non-local transport term in the K-Profile Parameterization (KPP) of Large *et al.* (1994) is turned off; (3) barotropic time stepping uses Crank-Nicolson instead of Adams-Bashforth; (4) no slip condition is applied at lateral boundary conditions; (5) lead closing parameter $H_0$ is 0.05 m instead of 0.61 m; and (6) sea ice strength $P^*$ is 27.5 kNm$^{-1}$ instead of 22.6 kNm$^{-1}$. Note that the LLC4320 model parameters have not yet been optimized in any way to fit observations; the above changes relative to Nguyen *et al.* (2011b) were primarily applied in order to make the LLC4320 integration numerically stable.

None of the above changes relative to Nguyen *et al.* (2011b) are essential to the sea ice model except for $H_0$ and $P^*$. A larger $P^*$ makes the ice "stiffer", but the value of 27.5 kNm$^{-1}$ is well within the accepted range, in fact, it is the value suggested by Hibler (1979). The lead closing parameter $H_0$ determines the thickness of newly formed ice (Hibler, 1979) and is a very powerful tuning parameter. The very small value used here implies very thin new ice of 0.05 m, so that a partially sea-ice free grid cell in freezing conditions can be covered by thin ice very quickly, reducing further heat flux and hence further ice growth. Essentially, low $H_0$ lead to overall thinner ice. The increased resolution and addition of tidal forcing in the LLC4320 simulation relative to Nguyen *et al.* (2011b) caused excessively thick sea ice to form with $H_0 = 0.61$ m, especially in shallow coastal regions, causing the LLC4320 simulation to go unstable. We reduced $H_0$ to 0.05 m to keep sea

ice thiner. Although this lower value of H0 allowed the integration to remain stable, it is almost certainly not the optimal value for this parameter.

### 2.2.3 Processing of modeled velocity fields

For the comparison of model results and EGPS data we sample the model fields in the same way as the EGPS data: a set of virtual buoys is initialized each day on the grid covered by the EGPS composite; for each model output step (i.e. , every 1 hour) streamlines through the virtual buoys are computed assuming a stationary velocity field within this time step, and the buoys are advected along the streamlines (Blanke & Raynaud, 1997); the virtual buoys are reinitialized every 24 h on the EGPS grid; velocity gradients and deformation rates are calculated from the drift of the virtual buoys by finite differences. Both EGPS data and the sampled LLC4320 model data set agree exactly in the regional coverage and the observation period (Sept. 13, 2011 to Apr. 8, 2012). The integration of daily trajectories emulates the EGPS sampling procedure of determining sea ice drift by tracking single points in the ice. In both cases, the EGPS and the retrieved LLC4320 composite, the final product is sea ice drift and deformation on an Eulerian grid.

## 2.3 Methods

### 2.3.1 Scaling Analysis

Except for Herman & Glowacki (2012), who used gridded Eulerian data in a spatial scaling analysis, scaling analyses of sea ice deformation are based on Lagrangian trajectories, either derived from satellite images (Marsan *et al.*, 2004; Stern & Lindsay, 2009), recorded by buoys (Rampal *et al.*, 2008; Hutchings *et al.*, 2011, 2012), or modeled in a Lagrangian framework (Rampal *et al.*, 2016). Both Lagrangian and Eulerian approach should, in theory, lead to the same spatial scaling results (if small time scales are considered where the advection of ice between two time steps is negligible), but the temporal scaling properties depend on the deformation history of individual ice flows. Eulerian averaging over a fixed box in space neglects the advection of this deformation history, so that this memory effect can only be taken into account by following one parcel of ice over time. Hence, the temporal scaling analysis requires a Lagrangian approach. However, the computation of strain rates

from Lagrangian trajectories is known to introduce errors by the choice of cell boundaries and the discontinuities in ice motion (Lindsay & Stern, 2003). These errors lead to an overestimation of the scaling exponents (Bouillon & Rampal, 2015a). Because both the LLC output and the EGPS data set are provided on Eulerian grids, the integration of trajectories from the gridded fields will introduce errors for each position on the trajectory. This position error is especially pronounced for the EGPS data, because the single data sets of the composite are recorded during different time periods leading to differences in the mean drift in the composite (see Fig. S1 in supporting information). These differences in mean drift will result in spurious deformation lines along the boundaries of single data sets. The model fields do not include these artificial velocity gradients because all velocities are computed in the same time interval, so that a Lagrangian approach will generate differences in the scaling analysis between observations and model that are not in the data but derive only from the analysis method.

We developed a method that combines both the Lagrangian tracking of ice and the computation of deformation rates on the original Eulerian grid. In doing so, trajectories of virtual buoys starting at the vertices of averaging boxes are integrated. The partial velocity derivatives computed on the Eulerian grid via finite differences are averaged in the advected boxes. After computing the deformation rates from the averaged velocity derivatives, this Lagrangian Sampling of Eulerian gridded data (LSE) provides a data set that combines the benefit of Eulerian gridded velocity data to precisely determine the deformation rates and the necessity of tracking the ice motion for temporal scaling. Fig. 2.2 illustrates the three different methods.

The virtual buoys defining the LSE averaging boxes are initialized on the corner points of the Eulerian grid of the EGPS composite. Because the EGPS data is provided as a set of drift vectors, we compute the trajectory by interpolating the drift vector at the position of the trajectory for each time step and by advecting the position accordingly. The model trajectories are computed in the same way using the retrieved LLC data to minimize sampling uncertainties. All virtual buoy positions that are closer than 150 km to the coast, or lie in regions with sea ice concentration lower than 0.15 are removed from the data, because we are only interested in the deformation of the dense ice pack. For each time step the position of each drifted averaging box in the Eulerian grid is determined. The partial velocity derivatives of all Eulerian grid cells that overlap partly or fully with the LSE averaging box
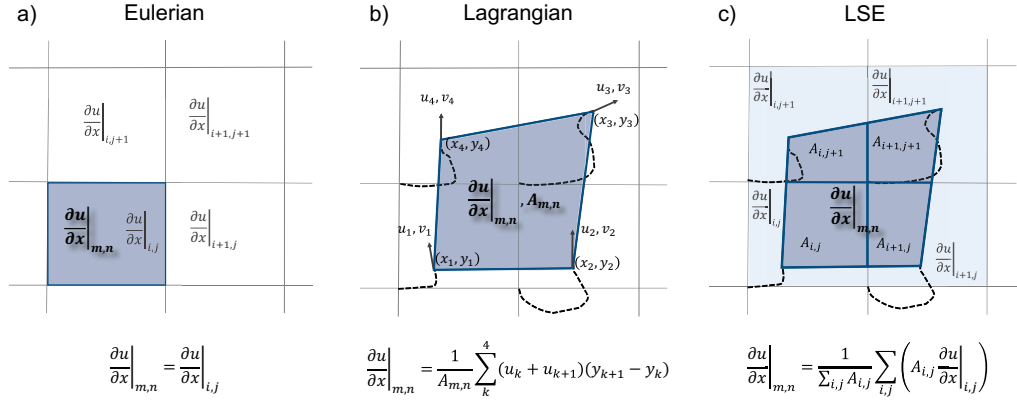
**Figure 2.2:** Overview of the three different methods of determining the velocity gradient in the scaling analysis. **(a)** In a Eulerian representation each box coincides with a grid box and the velocity gradient is computed by finite differences from the Eulerian gridded velocity data. The Lagrangian and LSE method use trajectories integrated from the velocity data that are given as dashed lines to define the displaced boxes. **(b)** In the Lagrangian method the velocities at the vertices of a displaced box are reconstructed from the trajectories and the gradient is determined by a line integral over the boundary of box (shaded in dark blue). **(c)** For the LSE method the gradients computed on the Eulerian grid are averaged over all grid cells that overlap with the averaging box (shaded in pale blue) weighted by the area of overlap (shaded in dark blue).

are averaged weighted by the overlapping area (see Fig. 2.2). As we use the corner points of the EGPS grid and four vertices per box, all LSE averaging boxes coincide with one EGPS grid cell at time zero. In the following time steps the network of averaging boxes will constantly drift and deform. The final output of the LSE method is a data-set of velocity gradients at the spatial scale of the EGPS grid of $L = 10\,\mathrm{km}$ and a temporal resolution of $\tau = 1\,\mathrm{day}$ that follows the ice parcels that are enclosed by the averaging boxes. The computation of deformation rates at larger spatial and temporal scales is then performed by the following scaling analysis.

To account for the coupling between temporal and spatial scales, we developed a method that simultaneously computes temporal and spatial scaling characteristics. To this end, a temporal component is added to the spatial scaling analysis of Marsan *et al.* (2004). In Marsan *et al.* (2004) strain rates are averaged in squares of size $L^\star \times L^\star$, to obtain strain rates at the spatial scale $L$ . Please note that there is a difference between the nominal spatial scale $L^\star$ determining the size of the box and the effective spatial scale $L$ associated with the box, as the box may not be entirely filled with data points

due to filtering and data coverage.

Prior to the spatial averaging we average the strain rates of each LSE box over the temporal scale $\tau^\star$. Strongly deformed LSE boxes are filtered by removing boxes that (1) are smaller than half the area of the initial EGPS cells $A_i < 0.5A_{org}$, (2) are larger than twice the area of the initial EGPS cells $A_i > 2A_{org}$, or (3) no longer form a quadrilateral box. The time covered by all unfiltered points is given by $T = N\Delta t$, where $N$ is the number of unfiltered data points and $\Delta t$ the temporal resolution of the data. After averaging, all grid points are removed, for which the time $T$ is below the threshold $T < 0.5\,\tau^\star$. In the next step, we compute the mean of all remaining temporally-averaged strain rates inside the $L^\star \times L^\star$ box. We define the $L^\star \times L^\star$ boxes in the first time step as a set of $\frac{L}{\Delta x}^\star \times \frac{L}{\Delta x}^\star$ neighboring LSE boxes, where $\Delta x$ defines the EGPS grid resolution. The position and shape of the averaging boxes will change with time as the defining LSE boxes will be advected and deformed by the ice motion.

Again due to filtering, the $L^\star \times L^\star$ box may not be not completely filled with valid data. If the area with valid data falls below the threshold $\sqrt{\sum A_i} < 0.5\,L^\star$, the average strain rate of this box is removed. The effective scales associated with the average strain rate of the cuboid are given by the coverage of the data after filtering, that is, for the effective temporal scale $\tau = T$ and for the effective spatial scale $L = \sqrt{\sum A_i}$.

The sampling of deformation rates following the ice motion is only necessary for scaling analyses that include temporal averaging of deformation. Whenever spatial scaling at the initial temporal scale of the drift data is computed, the tracking of single ice parcels is not necessary, and we can compute spatial averages on the Eulerian grid as done in Herman & Glowacki (2012). The second part of this paper evaluates only the spatial scaling properties of the LLC model results and all analyses will be performed on the Eulerian grid to reduce computational costs.

### 2.3.2  Evaluation of the Analysis Method

To evaluate the new scaling analysis for gridded Eulerian data, we quantify the sensitivity of the scaling properties to the method of computing spatial gradients. This information helps to assess our results and to compare them to previous results that were obtained by Lagrangian and Eulerian methods. To this end, we integrate trajectories of virtual buoys initialized on the EGPS
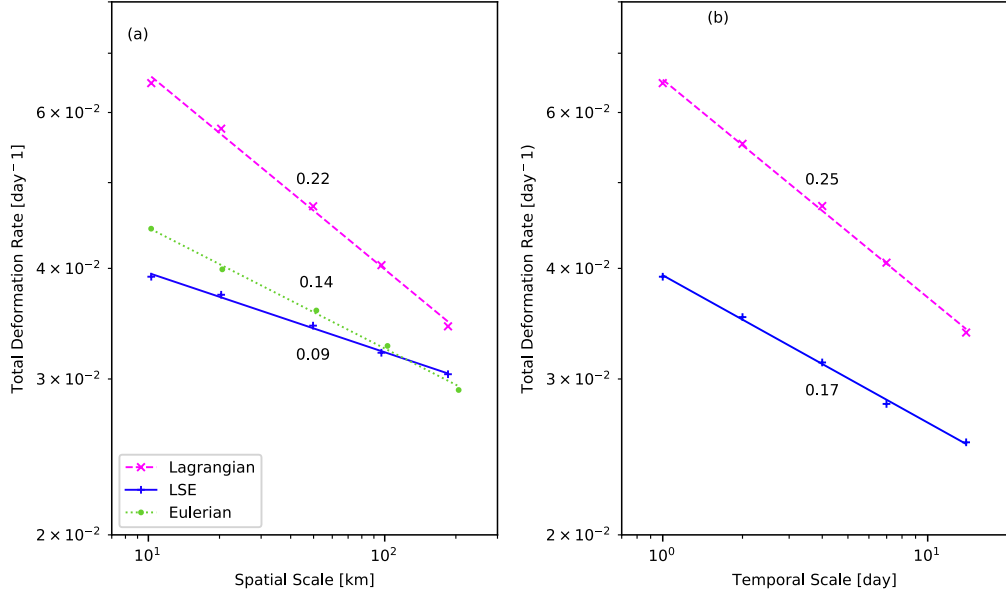
**Figure 2.3:** Scaling analyses for three different ways to compute strain rates that are LES, line integrals on trajectories (Lagrangian), and finite differences on Eulerian grid (Eulerian). **(a)** Spatial scaling analysis of Arctic sea ice deformation for the month January, February and March 2012 at a temporal scale of 1 day computed from the EGPS composite. **(b)** Temporal scaling analysis of Arctic sea ice deformation for the month January, February and March 2012 at a spatial scale of 10 km computed from the EGPS composite.

grid using the EGPS drift data as described above. Every 7 days a new set of virtual buoys is initialized for the time period from Jan. 1, 2012 to Mar. 31, 2012. The drift of each set of virtual buoys is computed for 14 day intervals. We perform the above introduced scaling analysis with (1) strain rates that are averaged using the LSE method, and (2) strain rates that are computed from the trajectories using line integrals Lindsay & Stern (2003). In addition, we compute spatial scaling at the initial temporal scale of $\tau = 1$ day using strain rates computed on the Eulerian grid (Fig. 2.3.).

As expected (Lindsay & Stern, 2003; Bouillon & Rampal, 2015a), the mean deformation rate computed from the Lagrangian trajectories is larger than the one computed on the Eulerian grid for all analyzed spatial scales. The lower mean deformation rates of LSE compared to the ones computed on the Eulerian grid are also plausible, because the partial velocity derivatives computed by LSE are averages of the Eulerian partial velocity derivatives and thereby smaller.

All three approaches lead to a power-law scaling of sea ice deformation

with regard to spatial and temporal scale. The higher spatial scaling exponents of the Lagrangian approach compared to the Eulerian approach can be explained by the overestimation of deformation rates due to the use of line integrals, and by the spurious shear lines due to the integration of composite velocity fields. Bouillon & Rampal (2015a) found that the Lagrangian method may overestimate the spatial scaling coefficient by up to 60 %; we observe 57 %. Due to the reduction of mean deformation rates, the spatial scaling exponent determined with LSE underestimates the Eulerian scaling exponent by 55 %. The temporal scaling exponents of LSE underestimate the exponents of the Lagrangian analysis by 47 %.

With this we can relate the scaling exponents of the LSE analysis to the results of other RGPS and buoy studies performed on a Lagrangian and an Eulerian grid. Although the underestimation of scaling exponents of LSE compared to the Lagrangian method complicates the comparison to previous results, we believe it is the appropriate method to analyze the Eulerian data in this study, because it avoids spurious overestimation of deformation rates and reduces the effect of varying mean drift within one time step of the EGPS composite.

## 2.4   Results

At first glance, the very high resolution VP simulation is very different from model results with coarser resolution: the deformation rates (divergence (b) and shear (c) in Fig. 2.4) concentrate along failure lines in the ice pack. These failure lines are characterized by low sea ice concentration (Fig. 2.4 (a)). We do not observe smooth variations of deformation rates over large areas as presented in Girard *et al.* (2009). In addition, the Probability Density Functions (PDF) of simulated deformation rates show power-law tails (see Fig. S3 in the supporting information). Compared to results of VP models with 4.5 km resolution (Losch *et al.*, 2014; Spreen *et al.*, 2016), there is a clear increase in the amount of detail with resolution.

### 2.4.1   Model-Observation Comparison

In the first part of our analysis we compare the model results directly to the EGPS data set. The comparison is confined to the region where the EGPS data set provides drift data for at least 14 consecutive days, that is,
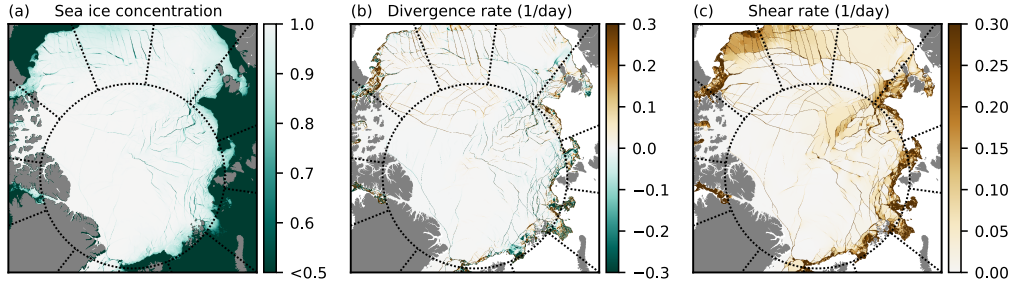
**Figure 2.4:** Sea ice concentration **(a)**, divergence rate **(b)**, and shear rate **(c)** of the LLC4320 run for Sept. 21, 2011, 2pm. The deformation rates concentrate along the leads seen in the sea ice concentration and mark Linear Kinematic Features (LKF).

the Central Arctic North of Greenland (green-shaded area in Fig. 2.1). In analogy to other scaling comparisons between model and observations (Girard *et al.*, 2009; Rampal *et al.*, 2016), our scaling analysis is limited to the winter months January, February, and March when the Arctic is fully ice covered with a dense ice pack. For April and May, satellite data are not available. We use the LSE scaling analysis on virtual buoy trajectories for this comparison, which are initialized every 7 days on the EGPS grid and last 14 days.

Broadly speaking, model results and observations agree on the order of magnitude of the deformation, but the observed deformation rates are slightly higher (Fig. 2.5). The spatial scaling exponent of the EGPS data ranges from 0.09 ($\tau = 1$ day) to 0.06 ($\tau = 14$ days). For the same temporal scales, the scaling exponents of the model data are around 0.06 and show no clear dependence on the temporal scale. Although the model reproduces the spatial scaling characteristics observed from EGPS for large temporal scales, there is no coupling of spatial and temporal scales in the modeled sea ice deformation.

With the power-law scaling of the moments (Eq. 2.1) we assess the multi-fractal characteristics of the modeled and observed sea ice deformation. For the temporal scale of $\tau = 1$ day, moments of the order $q = 0.5, 1, 1.5, 2, 2.5,$ and 3 are computed (Fig. 2.6). The structure function $\beta(q)$ is determined by a power-law fit to each moment. The structure function is quadratic $\beta(q) = aq^2 + bq + c$ with a positive curvature of $a = 0.06$ for the satellite observations and $a = 0.08$ for the model, so that $\beta(q)$ is convex, indicating multi-fractal characteristics for both data sets.

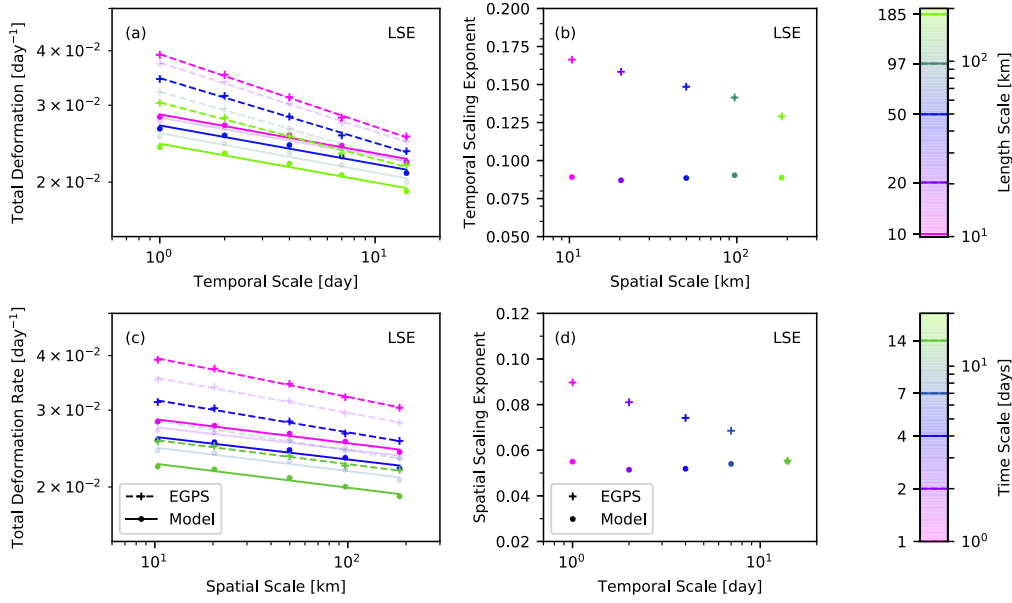The good agreement of the spatial scaling characteristics between model

**Figure 2.5:** Spatial-temporal scaling properties of model output compared to EGPS data. The comparison is confined to the area of the EGPS composite for each day and to the period of Jan. 1, 2012 to Mar. 31, 2012.



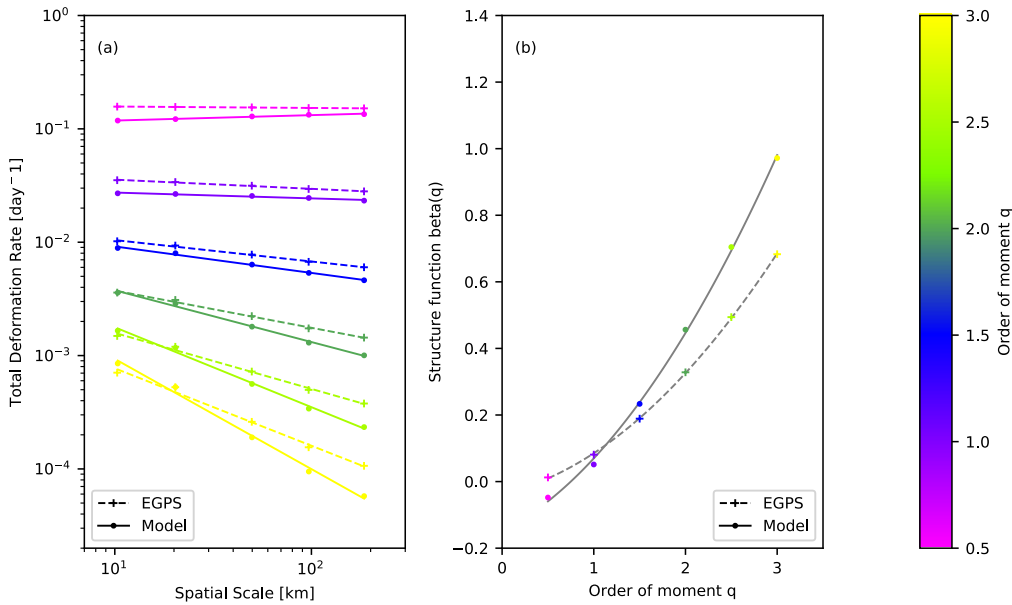**Figure 2.6:** **(a)** Spatial scaling analysis for different moments $|\epsilon_L^q| \sim L^{-\beta(q)}$ for model output and EGPS data. **(b)** Structure function $\beta(q)$ computed from linear fits to left panel. The fit to a quadratic function is given in dashed (EGPS) and solid (model) lines. Comparison is limited to the area of the EGPS data set.

and satellite data does not carry over to the Eulerian temporal scaling: for the EGPS data, the temporal scaling exponents range from 0.17 ($L = 10\,\mathrm{km}$) to 0.13 ($L = 185\,\mathrm{km}$), but the temporal scaling exponents of the model are lower with 0.9 (for both $L = 10\,\mathrm{km}$ and $L = 185\,\mathrm{km}$) and again show no dependence on the spatial scale (Fig. 2.5). The low scaling exponents imply that the model does not fully represent the intermittent character of sea ice deformation. This corresponds to our observation that leads develop slowly in the model in contrast to spontaneous failure observed from satellite, and once formed persist too long in the ice cover (see Fig. S6 in the supporting information). We note, however, that the comparison is limited to one winter and a small region North of Greenland. This region contains fast ice at the coast and high drift velocity in the export regions through Fram Strait and the comparison may be biased by the representation of these very specific sea ice states in the model.

### 2.4.2 Pan-Arctic Scaling Properties

After showing that the model at least in part reproduces the scaling characteristics observed in the EGPS data, we extend the spatio-temporal scaling analysis to the entire LLC4320 simulation. The entire model domain (blue-shaded area in Fig. 2.1) and all seasons are taken into account to study the influence of different ice conditions and the seasonal cycle of sea-ice deformation. In addition, the model-only analysis includes scales as small as $L = 1\,\mathrm{km}$ and $\tau = 1\,\mathrm{h}$.

A spatio-temporal scaling analysis tests the effect of reproduced leads on the scaling characteristics of sea ice deformation. We apply the LSE method described in Sec. 2.3.1 to all data between Dec. 1, 2011 to Apr. 30, 2012 in the entire model domain. To define the LSE boxes we integrate trajectories of virtual buoys that are initialized every 30 days on the model grid with a separation of roughly $10\,\mathrm{km}$. The deformation rates averaged by LSE are computed on the model grid with a horizontal grid spacing of $1\,\mathrm{km}$ and a temporal resolution of $1\,\mathrm{hour}$.

Figure 2.7 shows the results of this scaling analysis with the mean deformation at different spatial and temporal scales as well as the induced scaling exponents $\alpha$ and $\beta$.

The spatial scaling exponent $\beta$ ranges from 0.21 ($\tau = 3\,\mathrm{hour}$) to 0.19 ($\tau = 6\,\mathrm{days}$). Between this range, it varies approximately linearly with tem-
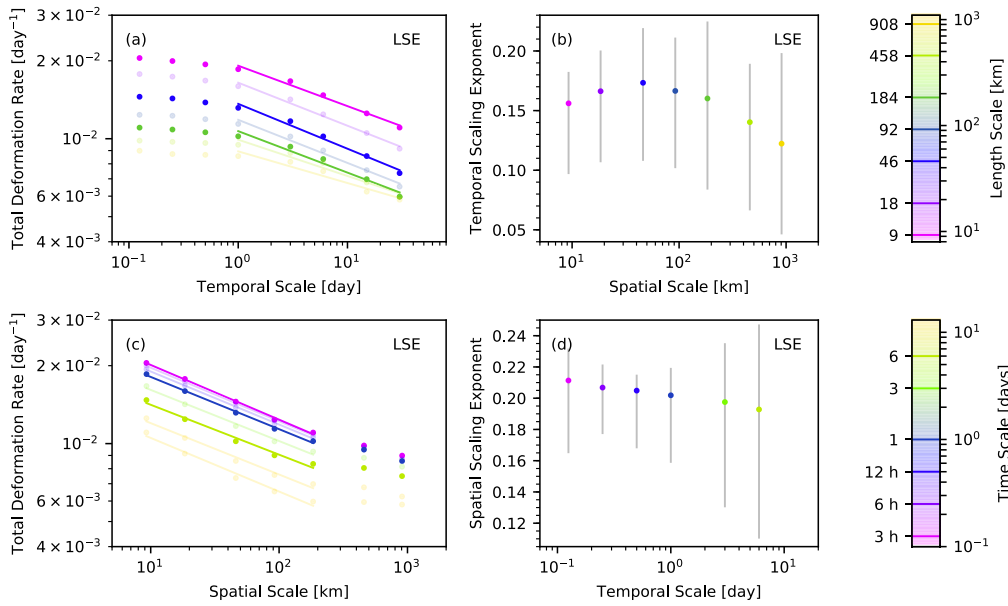
**Figure 2.7:** Spatio-temporal scaling of total deformation of the model output in the period between December and April 2012. Total deformation for different spatial and temporal scales are indicated by dots. Power-law fits to this data are presented as lines in the left panels **(a)** and **(c)**. The right panels **(b)** and **(d)** shows the power-law exponents of the fit with respect to the spatial scale and the temporal scale respectively. The error bounds of the scaling exponents are determined by the minimum and maximum slope between to successive points of the power-law fit.

poral scale. This shows that deformation is strongly localized for small temporal scales, whereas for larger temporal scales the averaging over different deformation events leads to a less heterogeneous deformation field.

The least square fit to the power laws of Eq. (2.2) in the temporal scaling analysis (Fig. 2.7 (a)) is restricted to scales larger than $\tau \geq 1\,\text{day}$. For smaller temporal scales the power-law flattens, which might be an imprint of the temporal resolution of the wind forcing of 6 hours. The flattening of the power-law is also reflected in the uncertainties of the scaling exponents in Fig. 2.7 (b). Less flattening would lead to smaller uncertainties in the fitted exponents. The temporal scaling exponent does depend linearly on the spatial scale, as it increases from 0.16 at 10 km to the maximum 0.17 at 46 km and decreases again to 0.12 at 908 km.

### 2.4.3  Seasonal Variation of Spatial Scaling

In the following three subsections, we restrict the discussion to spatial scaling properties at a temporal scale of $\tau = 1\,\text{h}$. Since no temporal scaling analysis is used in this section and only the initial time step is used, temporal averaging considering the advection of ice is not necessary. Therefore, we use deformation rates computed on the Eulerian model grid for the analysis within this section instead of LSE. We examine the seasonal cycle, the regional variation, and the dependence on the ice condition in analogy to Stern & Lindsay (2009). For this purpose, we analyze the entire LLC4320 simulation period (Sept. 13, 2011 to Oct. 8, 2012). The Arctic model domain is subdivided in boxes of size 500 km × 500 km with an overlap of 250 km. Within each box with an ice coverage of at least 25%, a spatial scaling analysis is performed for the temporal scale of 1 hour.

A clear seasonal cycle is seen in time series of both parameters of the power-law fit, that is, the scaling exponent and the mean deformation at 1 km (Fig. 2.8): while ice is freezing and the ice cover increases, the scaling exponent decreases to a minimum in April. With the onset of the melting season in May, the deformation and its heterogeneity (scaling exponent) increases to a maximum in August.

The seasonality of the deformation parameters is linked to the varying extent of the ice cover, as indicated by the apparent anti-correlation ($R = -0.92$) with the mean sea ice concentration in the model domain (Fig. 2.8). This covariation reflects the coupling of ice strength with con-
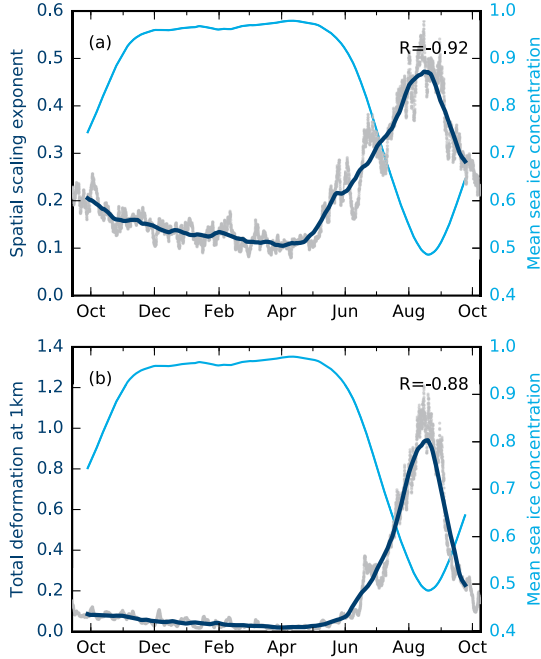
**Figure 2.8:** Seasonal variability of the power-law parameters (spatial scaling exponent **(a)** and total deformation at 1 km scale **(b)**) derived from the model output. In addition, the mean sea ice concentration averaged over all Arctic grid cells is given. The curve represents a running mean with an window size of one month.

centration (in the model, strength is proportional to $\exp[-C^*(1-A)]$). A closed ice cover at high concentration can, due to its high ice strength, support internal stress propagation over large distances. This "far field effect" leads to smaller differences of the deformation rates across the scales (Stern & Lindsay, 2009). In contrast, stress can not be redistributed in the loosely packed summer ice, and the number of deformation events increases leading to a very heterogeneous deformation field. In addition to the ice strength, two other factors, namely (1) the effect of the coastline as a boundary for an ice-filled Arctic and (2) the reduced atmospheric momentum transfer due to more stable atmospheric conditions in winter, contribute to the seasonal cycle (Kwok, 2006).

On top of the seasonal cycle, short term variations with a period of about 2 weeks are observed. We attribute those fluctuations to various weather systems passing the Arctic and initiating sea ice deformation. Herman & Glowacki (2012) showed this short-term variability to be driven by synoptic variability for RGPS data.

### 2.4.4 Scaling and Ice State

In a classical VP model, the ice strength $P = P^* h \exp\left[-C^*\left(1-A\right)\right]$ is defined by the ice condition and the two parameters $P^*$ and $C^*$ (Hibler,

1979); in our case these parameters are $P^* = 27.5\,\mathrm{kN\,m^{-2}}$ and $C^* = 20$. To examine the influence of ice strength on the spatial scaling exponent and test for different scaling behavior in multi-year and first-year ice, we study its dependence on sea ice concentration $A$ and thickness $h$. Figure 2.9 shows the mean sea ice concentration and thickness within each $500\,\mathrm{km} \times 500\,\mathrm{km}$ box (as defined in Section 2.4.3) and its corresponding scaling exponent as a scatter plot, along with the mean scaling exponent given at a certain concentration or thickness.

The lowest mean spatial scaling exponents are found for fully covered boxes. Most points range around a sea ice concentration of one and a scaling exponent of 0.08. For lower sea ice concentrations, the spatial scaling exponent increases strongly and levels off towards very low concentrations, as expected from the exponential form of the strength expression.

The mean spatial scaling exponent also decreases almost linearly with increasing sea ice thickness from 0.4 for very thin ice down to 0.1 for ice thicker than 2 m. The impact of ice thickness, however, is smaller than that of concentration and approximately linear. The variance of the spatial scaling coefficient at a given thickness is higher than the variance at a given concentration, as indicated by the wider spread of spatial scaling exponents in Fig. 2.9, bottom panel.

The trend in both curves is consistent with the ice strength parametrization, showing that the model reproduces the influence of the ice strength on the spatial scaling properties. The influence on the second scaling parameter (mean deformation at 1 km) is similar (not shown). The higher correlation coefficient between scaling exponent and concentration ($R = -0.68$) compared to thickness ($R = -0.33$) can also be explained by the functional form of the ice strength: ice strength varies exponentially with concentration, but only linearly with thickness. The difference between the correlation coefficients computed for the mean concentration of single boxes (Fig. 2.9) and of the entire Arctic (Fig. 2.8) shows that, in addition to the influence of ice strength, there is an effect of lateral (land) boundaries in an ice-filled Arctic (Kwok, 2006).

### 2.4.5   Regional Variation of Spatial Scaling

The regional variation of the scaling exponent in January 2012 is shown in Fig. 2.10. The Central Arctic is mainly characterized by very low scaling
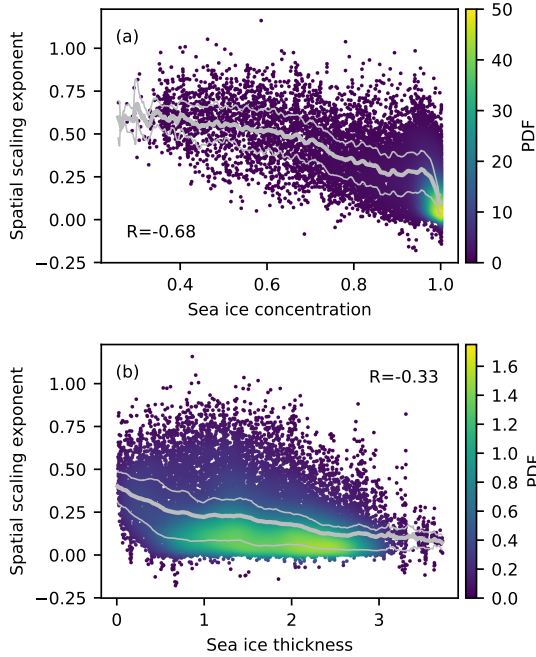
**Figure 2.9:** Spatial scaling coefficient as function of sea ice concentration **(a)** and thickness **(b)**. The thick gray line shows the running mean with an averaging window of $1\,\%$ for sea ice concentration and $20\,\mathrm{cm}$ for sea ice thickness. The thin lines show the 25th and 75th percentile. Each dot represents the coefficient of an individual grid box. The color indicates their probability density and illustrates the variance of the results (for clarity only $2\,\%$ of the data are shown for the density).

exponents ($0 < \beta < 0.09$) because the ice strength is high (high concentration and thickness). At the coast of Alaska towards the Bering Strait, the scaling exponents increase ($0.13 < \beta < 0.21$). The relatively thin ice in this region is prone to deformation leading to very heterogeneous deformation fields. The highest values are found in the Fram Strait and the Barent Sea, where scaling exponents range between 0.17 and 0.5. In those regions opening towards the Atlantic Ocean, the thin and mostly seasonal ice is continuously deformed because of high sea ice velocity shear due to the high ice speed.

## 2.5   Discussion

Before putting our results into perspective, we note once again that the LLC4320 simulation has not been adjusted or data-constrained in any way. We therefore expect differences between observations and simulation not only for the chaotic components of the circulation, for example, the location of mesoscale eddies or of cracks in the ice, but also for larger-scale properties such as sea ice concentration, thickness, and drift. The above limitations need to be kept in mind when using the LLC4320 simulation to explore the behavior of VP rheology at high spatial resolution.

The direct comparison of the model results to satellite observations is restricted to the region North of Greenland during the winter months of Jan-
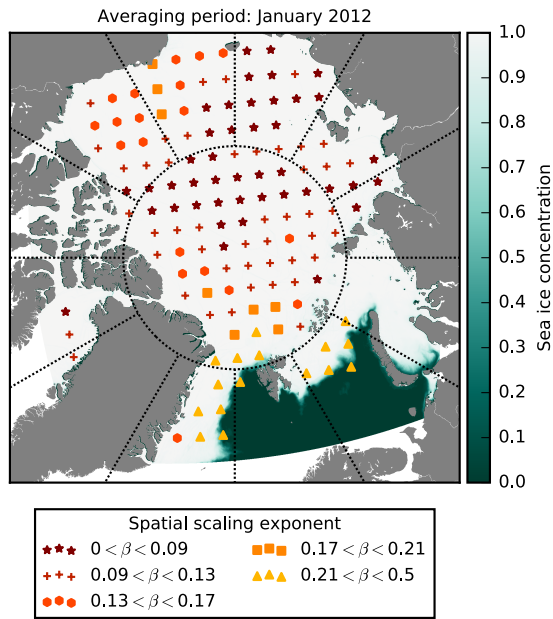
**Figure 2.10:** Regional variation of spatial scaling exponent for January 2012. The spatial scaling exponent is given by different markers and the color shading shows the mean sea ice concentration.

uary, February, and March due to limited satellite data availability. Due to the small area of satellite data the comparison could also be dominated by local effects. Because of the this data limitation, the separate analysis of the model results also needs to be taken into account when evaluating the ability of the model to reproduce scaling characteristics of sea ice deformation. The differences between spatial scaling exponents for the model output and satellite data range from 0.03 at a temporal scale of $\tau = 1\,\mathrm{day}$ to perfect agreement at $\tau = 14\,\mathrm{days}$, due to the missing coupling between spatial and temporal scaling.

The spatial scaling exponents derived from the EGPS dataset $(\beta\,(\tau = 4\,\mathrm{days}) = 0.08$ ) agree well with published numbers for the RGPS data set $(\beta\,(\tau = 3\,\mathrm{days}) = 0.20$, Marsan *et al.*, 2004; Stern & Lindsay, 2009)) considering the underestimation of the used LSE method compared to Lagrangian based referenced studies. Recall that in Section 2.3.2 the Lagrangian scaling analysis for the EGPS data set yielded spatial scaling exponents of 0.22 for the 1 day temporal scale. We observe a dependence of the spatial scaling exponents on the temporal scale in line with previous results (Rampal *et al.*, 2008; Marsan & Weiss, 2010) for satellite observations. In contrast, the model results do not show such a clear coupling in this region. Only in the Pan-Arctic scaling analysis for the model results a coupling between spatial scaling exponents and temporal scale is seen, although the coupling is weaker than for satellite observations (variation of 0.02 over a

range of two orders magnitudes for the model results in contrast to a variation of 0.03 over one order of magnitude). The space-time coupling exists, because deformation on a short timescale is likely to take place nearby as a reaction to previous deformation (Weiss, 2017), so that averaging deformation over short time periods leads to a strong localization of deformation rates around a few deformation events. Therefore, the weaker coupling in the model points to the model lacking a mechanism that links previous and current deformation. This aspect will be discussed in further detail in the discussion on the temporal scaling at the end of this section.

The spatial scaling for all moments of the modeled deformation rates agrees with the satellite data. The curvature of the structure function of the model ($a = 0.08$) and the satellite data ($a = 0.06$) are slightly lower than previously reported ($a = 0.13$) (Marsan *et al.*, 2004; Rampal *et al.*, 2016), which can be explained using LSE instead of a pure Lagrangian scaling analysis. In summary, the good agreement of the spatial scaling of the model with satellite observations shows that the VP model can reproduce deformation rates that are strongly localized in space, but we observe only a weak coupling to the temporal scale.

The sea ice deformation of the entire model domain is characterized by spatial power-scaling with $\beta = 0.20$ for a temporal scale of 3 days compared to RGPS-data-based estimates of $\beta \approx 0.2$ for a timescale of 3 days without filtering (Marsan *et al.*, 2004; Stern & Lindsay, 2009; Girard *et al.*, 2009; Hutchings *et al.*, 2011). Rampal *et al.* (2016) found the scaling exponent of filtered RGPS data to be $\beta = 0.16$ for the shear rate. Taking into account the smoothing by LSE method, the model overestimates the localization of deformation. The smoothing effect of the LSE method may explain part of the underestimation by the model in the restricted region of the model-observation comparison.

We find that the model reproduces the seasonal cycle of scaling coefficients observed by Stern & Lindsay (2009). The strong increase in the scaling exponent in May and the drop to a quasi-steady state in November are captured by the model. A comparison for the short summer period is not possible due to the summer gap of RGPS. However, a maximum at the end of August is plausible considering the minimum sea ice extent at this time.

We find that the seasonal cycle of the scaling coefficients is most likely determined by the ice condition and the ice coverage of the Arctic. The scaling coefficients depend on the ice condition through the ice strength

parametrization. Stern & Lindsay (2009) evaluated the dependence of the scaling exponent on the multi-year ice fraction and found lower exponents for more multi-year ice. Comparing this trend to our thickness dependence, the model seems to underestimate deformation rates for thin (presumably first-year) ice, which implies that changing to a higher-order ice-strength parameterization, for example $P \sim h^2$ (Rothrock, 1975), might improve the results. We did not analyze the influence of a more stable atmosphere in wintertime on the seasonal cycle, which is the third effect identified by Kwok (2006), but idealized model experiments (not shown here) show a high sensitivity to changes in the wind forcing indicating that this effect should be resolved in the simulation.

The regional distribution of scaling exponents shows that sea ice deformation localizes strongly in less confined regions of high velocities and thin ice, where the velocity gradients are largest and the low ice strength quickly leads to plastic deformation of the ice cover. Stern & Lindsay (2009) also observed the highest exponents in first year ice at the coast of Alaska and North of the Lincoln Sea. The model underestimates the scaling in regions of first year ice (coast of Alaska and Siberia), which could be addressed with an adapted ice strength parametrization (see previous paragraph).

For temporal scaling exponents, the differences between model and satellite data are larger. North of Greenland there is no coupling of the temporal scaling exponent to spatial scales in the model. In contrast, the temporal scaling exponents of the Pan-Arctic analysis show a dependence on the spatial scale. However, only for spatial scales $L > 40\,\mathrm{km}$ the temporal scaling exponent decreases with increasing spatial scale as found in satellite and buoy data (Rampal *et al.*, 2008; Weiss & Dansereau, 2017). This length scale coincides with twice the wind forcing resolution indicating that the scaling characteristics of the sea-ice model may be determined by the characteristics of the forcing wind fields rather than by the details of the rheology. The loss of temporal scaling for scales smaller than $\tau \leq 1\,\mathrm{day}$ supports this hypothesis. The spatial scaling also breaks down for spatial scales $L \leq 10\,\mathrm{km}$. This scale coincides with the spatial resolution of the wind forcing ($\sim 15\,\mathrm{km}$) (see Eulerian spatial scaling analysis, Fig. S5 in the supporting information). Our inferences are further supported by idealized model experiments with viscous-plastic sea-ice models that showed a strong impact of wind forcing resolution on scaling characteristics of sea ice deformation (Hutter, 2015).

The poor temporal scaling points towards deficits in the VP model physics,

especially as both spatial and temporal scaling emerge from an EB-model (Rampal *et al.*, 2016). When a critical stress is reached in an EB-model, brittle deformation damages the ice and instantaneously reduces the ice strength locally. The damage information is kept over a certain healing time. In VP models, exceeding the critical stress leads to plastic deformation. A permanent weakening of the ice takes place only for large deformation events with diverging ice motion, which result in a lead of at least grid scale. The reduction in sea ice concentration and thickness leads to a lower ice strength in the next time step. Weaker ice invites more deformation at lower strain rates and hence a positive feedback loop is generated. Compared to the instantaneous failure processes in the EB-rheology, this reduction is slow so that the temporal evolution of sea ice deformation is smooth and the scaling exponents are smaller. To improve this, the ice strength of a VP model could also be directly linked to plastic deformation occurring in a grid cell and by this introduce a memory of old deformation to the ice. To this end, a damage parameter in the ice strength parameterization could be introduced or the ice strength could be coupled directly to the plastic deformation of the previous time step. We further hypothesize that introducing a multi-category sea-ice thickness distribution along with an appropriate ice strength parameterization (Rothrock, 1975) would intensify the feedback-loop between ice strength and deformation. Because the standard ice strength parameterization in ice thickness distribution models (Rothrock, 1975) is determined to a large extent by the thin ice categories, the ice strength field is very heterogeneous and can lead to more deformation (Ungermann *et al.*, 2017).

Why do VP models start to reproduce leads at higher resolution? We speculate that only at high resolution there is the potential of significantly reducing sea ice concentration within a grid cell by divergent sea ice motion, which is necessary to initiate the positive feedback cycle outlined in the previous paragraph. A weaker cell leads to larger velocity gradients in the surrounding cells and to plastic deformation. In this way, lines of grid cells of reduced ice strength are produced, along which the deformation rates localize.

## 2.6    Conclusion

A sea ice model using the VP rheology with a horizontal grid spacing of $\sim 1\,\mathrm{km}$ reproduces LKFs along with many of the observed scaling properties of sea ice deformation. In contrast to previous studies with VP models (Girard *et al.*, 2009), there is appropriate spatial scaling in our model simulations. The spatial scaling agrees in the seasonal variation and regional distribution with satellite observations. The VP model as configured in the LLC4320 simulation underestimates temporal scaling exponents and the coupling between spatial and temporal scaling when compared to the observed temporal scaling of sea ice deformation. We note, however, that in this study we have not made any attempt to obtain a more accurate temporal scaling by, for example, careful adjustment of the ice strength parameterization (e.g., Bouchat & Tremblay, 2017) or application of more realistic atmospheric forcing.

The new scaling analysis presented in this paper is based on Lagrangian sampling of Eulerian gridded data (LSE) and determines spatial and temporal scaling properties simultaneously for data on Eulerian grids while taking into account the advection of sea ice. With most recent sea ice deformation data sets and the output of most sea ice models provided on Eulerian grids, the LSE approach is a robust temporal scaling analysis method for gridded Eulerian data. The method evaluation relates the obtained spatial and temporal scaling to previous scaling results using either Lagrangian or Eulerian gridded data.

The good agreement of the spatial scaling with satellite observations suggests that the VP rheology, in spite of recent criticism (Girard *et al.*, 2009), is still suitable at high spatial resolution to reproduce the spatial characteristics of sea ice deformation with its multi-fractal structure. Since subgrid-scale damage is not parameterized in the VP model, the power-law scaling is limited to scales $L > 5\,\mathrm{km}$, as some grid cells are required to resolve a deformation feature. We can not exclude that this limitation is a consequence of the low spatial resolution of the atmospheric forcing. The underestimation of scaling exponents in first year ice could be addressed with a higher order dependence of the ice strength on sea ice thickness, which would reduce the stress propagation in these thin-ice areas. In general, the sensitivity of the scaling properties to model tuning parameters such as maximum ice

strength $P^*$, shape of the yield curve, lead closing parameters, and similar, should be studied. The scaling properties could be implemented into a tuning mechanism as a measure to gauge realism of small-scale sea-ice deformation in addition to other large-scale metrics such as ice extent, concentration or mean thickness.

The temporal scaling analysis implies that the crack formation of the VP model as configured in this study is too slow compared to observations. We hypothesize that an adaptation of the ice strength parameterization, in which previous plastic deformations — in analogy to the EB-rheology — induce a reduction in ice strength over a certain time, may improve the temporal scaling properties. Nevertheless, new metrics based on the temporal evolution of individual deformation events and features would help to specify the shortcomings of the model. Without any modification relative to LLC4320 set-up, the VP rheology can be used to simulate processes where the small-scale temporal evolution of sea ice is not critical. For time-critical applications such as short-term forecasts, however, the VP rheology as configured in the LLC4320 set-up appears inadequate.

Since the VP model reproduces localized deformation in space in agreement with satellite observations but not in time, a detailed comparison with the Maxwell-EB rheology in the same modeling framework would give valuable insight into how different parameterizations impact small-scale deformation. Besides large-scale metrics, new ways of comparing simulations and observations based on statistics of sets of individual leads such as density, persistence, orientation, intersection angle, and length should be explored to directly identify the differences between different rheologies and satellite observations.

# 3. Leads and ridges in Arctic sea ice from RGPS data and a new tracking algorithm [1]

**Abstract** Leads and pressure ridges are dominant features of the Arctic sea ice cover. Not only do they affect heat loss and surface drag, but also provide insight into the underlying physics of sea ice deformation. Due to their elongated shape they are referred as Linear Kinematic Features (LKFs). This paper introduces two methods that detect and track LKFs in sea ice deformation data and establish an LKF data set for the entire observing period of the RADARSAT Geophysical Processor System (RGPS). Both algorithms are available as open-source code and applicable to any gridded sea-ice drift and deformation data. The LKF detection algorithm classifies pixels with higher deformation rates compared to the immediate environment as LKF pixels, divides the binary LKF map into small segments, and re-connects multiple segments into individual LKFs based on their distance and orientation relative to each other. The tracking algorithm uses sea-ice drift information to estimate a first guess of LKF distribution and identifies tracked features by the degree of overlap between detected features and the first guess. An optimization of the parameters of both algorithms is presented, as well as an extensive evaluation of both algorithms against hand-picked features in a reference data set. An LKF data set is derived from RGPS deformation data for the years from 1996 to 2008 that enables a comprehensive description of LKFs. LKF densities and LKF intersection angles derived from this data set agree well with previous estimates. Further, a stretched exponential distribution of LKF length, an exponential tail in the distribution of LKF lifetimes, and a strong link to atmospheric drivers, here Arctic cyclones, are derived from the data set. Both algorithms are applied to output of a numerical sea-ice model to compare the LKF intersection angles in a high-resolution Arctic sea-ice simulation with the LKF data set.

## 3.1 Introduction

The Arctic sea ice cover is an aggregation of ice floes of different size that changes continuously due to thermodynamic and dynamic processes. Thermodynamic processes slowly modify the shape of floes by freezing and melting, but rapid changes in floes shapes are caused by the deformation of the brittle ice. The drivers of these events are mainly wind, ocean currents, tides and interaction with coastal geometries.

When the ice cover breaks, leads form along floe boundaries as strips of open ocean. In such an opening of the ice cover there is strong upward heat flux from the warm ocean to the cold atmosphere, causing new ice formation and changes of the albedo. Colliding ice floes form pressure ridges and ice keels that change both the atmosphere-ice and the ice-ocean drag coefficient. Both leads and pressure ridges are usually elongated features with lengths ranging from a few meters up to hundreds of kilometers.

Multiple studies used large amounts and and a great variety of satellite imagery of the Arctic ocean to describe the characteristics of deformation features and gain insight into the underlying physics. Lead densities were derived from MODIS images in the thermal infrared for cloud-free parts of the Arctic Ocean (Willmes & Heinemann, 2016), from AMSR-E passive microwave brightness temperatures (Röhrs & Kaleschke, 2012), and from CryoSat2 altimeter data (Wernecke & Kaleschke, 2015). Bröhan & Kaleschke (2014) extracted Pan-Arctic lead orientations from passive microwave data using a Hough transform. Kwok (2001) provided a qualitative description of these deformation features based on drift observations derived from SAR imagery, combining leads and pressure ridges under the term Linear Kinematic Features (LKFs) due to their dynamic nature. All these studies avoid the problem of detecting individual LKFs by applying statistics over continuous fields such as sea ice deformation or concentration. Miles & Barry (1998) presented a 5-year climatology of lead density and orientation based on manual detection in thermal- and visible-band imagery. Manual detection was also used to study the intersection angles of LKFs and its inferences on the rheology describing sea-ice deformation (Erlingsson, 1988; Walter & Overland, 1993).

All of these studies are limited either to specific information (density or orientation) or to a short time-series due to laborious manual detection. First attempts to automatically extract LKFs from satellite data were based on skeletons to describe LKFs (Banfield, 1992; Van Dyne & Tsatsoulis, 1993; Van Dyne *et al.*, 1998), but Van Dyne *et al.* (1998) suggested "knowledge-based techniques" to further divide a skeleton into individual branches. This idea was picked up in an algorithm that automatically detects LKFs as objects in sea-ice deformation data (Linow & Dierking, 2017). Only 10 RGPS snapshots were analyzed in this way, but many more snapshots are necessary for a comprehensive description of LKFs. As the method of Linow & Dierking (2017) does not contain a tracking algorithm for LKFs, important temporal

characteristics such as lifetimes cannot be derived from their detected LKFs, but only spatial statistics.

With increasing resolution of classical (viscous-plastic) sea ice models (Hutter *et al.*, 2018) or with new rheological frameworks (e.g. Maxwell elasto-brittle, Rampal *et al.*, 2016; Dansereau *et al.*, 2016), sea-ice models start to resolve small-scale deformation with larger floes and leads. Typical measures for evaluating the modeled LKFs include scaling properties of sea-ice deformation (Hutter *et al.*, 2018) or lead area density (Wang *et al.*, 2016). An evaluation of these simulations based on individual features would be far more comprehensive and thorough and would help to improve model physics.

The objective of this study is to develop an open-source algorithm that automatically detects deformation features in regular gridded sea-ice deformation data and then tracks them using drift data. For this purpose, we present a modified version of the detection algorithm of Linow & Dierking (2017) and introduce an automatic tracking algorithm that takes into account the advection of deformation features with the overall sea-ice drift as well as growing and and shrinking features. Both algorithms are applied to the entire RADARSAT Geophysical Processor System (RGPS) drift and deformation data set to produce a multi-year LKF data-set that makes a comprehensive description of spatio-temporal characteristics of LKFs possible.

## 3.2   Data

One main requirement of the LKF detection algorithm presented in this study is that it should be applicable to both satellite observations and output of numerical sea-ice models. Thus, we use deformation data to detect LKFs rather than passive microwave data (Bröhan & Kaleschke, 2014) or thermal infrared imagery (Willmes & Heinemann, 2016), which is usually not simulated in a sea ice model. Sea ice deformation, which is derived from sea-ice drift, can be observed by satellite, ship radar, and buoys and it is also simulated by numerical models.

### 3.2.1   Deformation data

In this study, we use deformation data provided by the RADARSAT Geophysical Processor System (RGPS) (Kwok, 1998, data obtained from `https://rkwok.jpl.nasa.gov/radarsat/index.html`). This data set is based on

sea ice drift derived by tracking ice motion in SAR images. In each freezing season points are initialized on a regular 10-km grid that are tracked over the winter until the on-set of the melting season. A Lagrangian deformation data set is computed from these trajectories using line integral approximations (e.g. Lindsay & Stern, 2003). Data is available for the years 1997 to 2008 with varying spatial coverage of the Amerasian Basin. We use the gridded version of the RGPS data-set for our analysis, which is interpolated on to a regular grid with 12.5 km grid spacing.

### 3.2.2 Drift data

To track features detected by the LKF detection algorithm in RGPS deformation data, the drift between two RGPS records is required for an a-priori guess of the temporal continuation of the individual feature. In the RGPS data set the derived deformation data is published along with the original drift data that is used for the deformation rate computation. Since RGPS drift is only provided as a Lagrangian data set (Kwok, 1998, data obtained from `https://rkwok.jpl.nasa.gov/radarsat/index.html`), we interpolate the drift to the same regular 12.5-km grid on which the deformation data is provided.

### 3.2.3 Evaluation data-set

Automated object detection requires an evaluation against validation data. For this purpose, we use the data set of hand-picked LKFs presented in Linow & Dierking (2017). This data set comprises 1411 LKFs detected by human eye for 12 RGPS snapshots (December 29, 2005 to February 2, 2006). The intrinsic localization uncertainty of the visually detected features was shown to be 0.75 pixels with 1 pixel corresponding to a grid cell of size $12.5 \times 12.5$ km and the uncertainty in the line length 8% (Linow & Dierking, 2017).

Since this data set only provides LKFs for single snapshots but does not include information about the temporal evolution of LKFs between different snapshots, we need to expand the data set in this regard. In doing so, we advect the hand-picked LKFs of one snapshot using the RGPS drift to get an a priori guess of LKF position in the next snapshot. We visually compare the advected LKFs from the previous snapshot to LKFs of the next snapshot. If two LKFs overlap and agree in the entire overlapping area in position,

shape, and orientation, they are marked as tracked LKF. Furthermore, each tracked LKF is described by probability, degree of overlap, and type of shape change (no change, growing, shrinking, and branching), which are all visually estimated. In total 392 LKFs were tracked within these 12 RGPS snapshots, which corresponds to $\sim 28\%$ of the LKFs in the evaluation data set. For the remaining 1019 LKFs no matching LKF in the next record is found. Thus, these LKFs have a lifetime that is shorter than the temporal resolution of 3 days if errors in the manual tracking are not considered.

## 3.3   LKF detection

### 3.3.1   Method description

Our LKF detection algorithm consists of three parts: (1) a preprocessing step that transforms the input deformation data into a binary map of pixels that mark LKFs by using different filter steps, (2) a detection routine that splits the network of LKF pixels in the binary map into the smallest possible segments, and (3) a reconnection instance that estimates the probability of different segments belonging to one feature and then connects all segments of a LKF. The general structure of the algorithm follows Linow & Dierking (2017), although individual parts have been modified substantially. The main enhancements of the algorithm are a parallel detection of segments with a stronger constraint on the curvature and the introduction of a probability based reconnection. Further, the entire algorithm was rewritten in Python (Python Software Foundation, `http://www.python.org`) to avoid license issues with the previous code that was based on the commercial software IDL.

**Data preprocessing and filtering**

The standard input data of the LKF detection algorithm is the total deformation rate of sea ice $\dot{\epsilon}_{tot} = \sqrt{\dot{\epsilon}_I^2 + \dot{\epsilon}_{II}^2}$, where $\dot{\epsilon}_I$ is the divergence and $\dot{\epsilon}_{II}$ shear that can be derived from both satellite data and model output (Fig. 3.1a). LKFs are defined by regions of high deformation rates, because they are located along the boundaries of ice floes where most deformation takes place. The actual magnitude of deformation along an LKF, however, varies with the background deformation and the spatial scale, because of its multi-fractal properties (Weiss, 2013). Thus a simple thresholding of defor-

mation rates is not sufficient to filter LKFs. Instead, we are interested in detecting deformation that is notably higher than the local environment. As LKFs are lines of high deformation, we need to detect edges in the deformation field.

Prior to the edge detection, we take the natural logarithm of the input field (Fig. 3.1b) and perform a histogram equalization (Fig. 3.1c). Both highlight the local differences across different scales and enhance the contrast in regions of low deformation rates.

We use a Difference of Gaussian filter (DoG) following Linow & Dierking (2017) for the edge detection (Fig. 3.1d). The DoG filter subtracts two filtered versions of the same input data: the first is smoothed with a Gaussian kernel of radius $r_1 = 1$ pixels corresponding to a half-width $\sigma_1 = 0.5$, and the second is smoothed with a Gaussian kernel of radius $r_2 = 5$ pixels (half-width $\sigma_2 = 2.5$), where $r_1 < r_2$. The smaller radius $r_1$ corresponds to the smallest scale of features that will be detected by the DoG and the second radius $r_2$ provides the upper limit of the scales detected. Note that this scale limitation applies to the width of the LKFs as well as to their lengths. For edges of scale $r_1 < L < r_2$, the DoG-filtered values are positive because the local deformation rate is higher than in the environment of radius $r_2$. Pixels are marked as LKFs when the DoG-filtered pixels are larger than a positive threshold $d_{\mathrm{LKF}}$. The result is a binary map where pixels with value 1 belong to LKFs (see Fig. 3.1e for a threshold of 15). The threshold $d_{\mathrm{LKF}}$ does not have a unit as it describes the difference of two histogram equalized images, where the highest deformation rate corresponds to a pixel value 255 and the lowest to value of 0.

At this point, LKFs in the binary map are still represented in their original width. To detect which pixels belong to which LKF we add a further level of abstraction and reduce the width of all LKFs to one pixel (Fig. 3.1f). To this end, a morphological thinning algorithm reduces the binary map to its skeleton. We use the `skeletonize` function of the open-source python package `scikit-image` (van der Walt *et al.*, 2014) based on Zhang & Suen (1984). Skeletonization was used before to detect leads in original or classified, that is, preprocessed and charted, SAR images (Banfield, 1992; Van Dyne & Tsatsoulis, 1993; Van Dyne *et al.*, 1998).
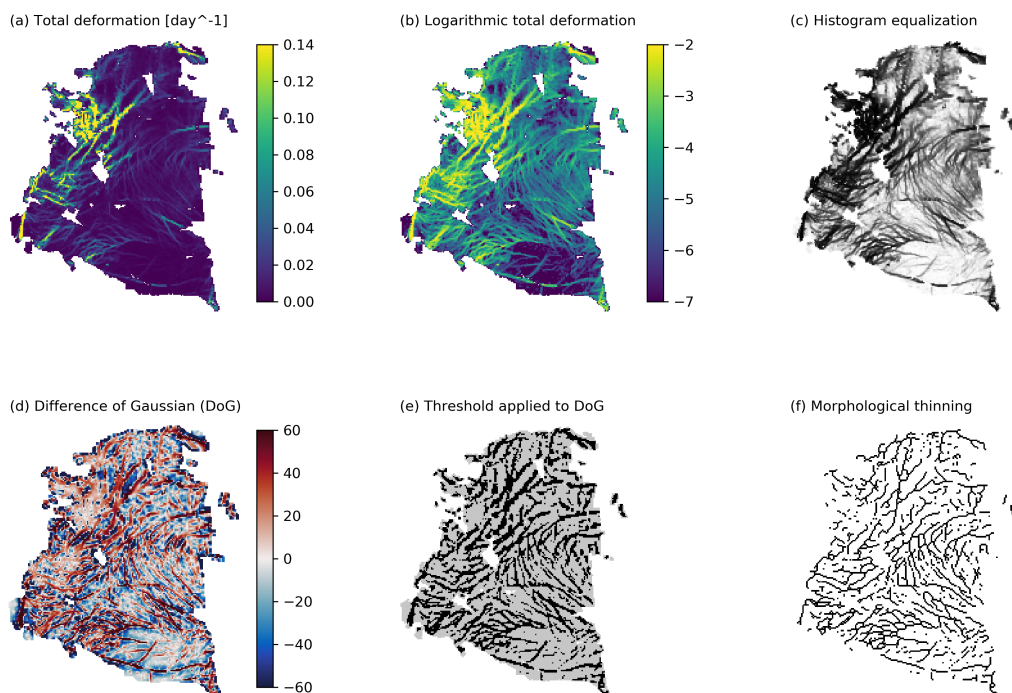
47

**Figure 3.1:** Filter sequence from **(a)** input field total deformation to **(f)** final output of the morphological thinned binary map of LKF pixels. Intermediate steps are **(b)** logarithmic deformation, **(c)** histogram equalization, **(d)** Difference of Gaussian filter, and **(e)** the thresholded output of the DoG filter. RGPS deformation data for January 1st, 2006 is used for this example.

### Segment detection

We detect small segments of pixels that contain parts of one LKF in the binary map. Based on the morphological thinned binary map, groups of pixels that form a line are detected. In this first detection step, we want to guarantee that all pixels of a detected segment belong to the same LKF. Therefore, we detect the smallest segments possible that are in the simplest case the points in between intersections of lines in the binary map (Fig. 3.1f).

As a starting point of the segment detection we use LKF pixels that have only one neighbouring cell also marked as LKF. Within each iteration, the detection algorithm proceeds to the LKF neighbour and checks again the number of neighbouring cells for LKFs. If the new cell has also only one neighbouring LKF cell (neglecting the cell from the prior iteration) the search is continued. If the new cell has more than one neighbouring LKF cell, that is, it is a junction, the detection cycle is stopped and these neighbouring points become the new starting points. Besides the number of neighbouring LKF

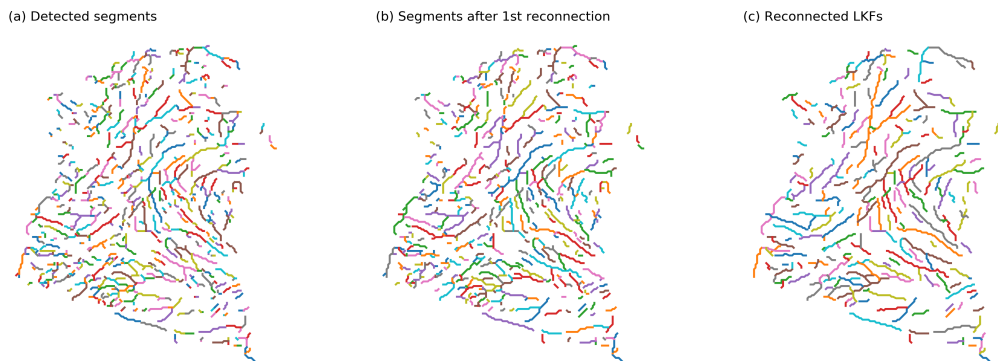**Figure 3.2: (a)** Detected segments and the results of **(b)** the first reconnection step and **(c)** the second reconnection step for RGPS deformation data from January 1st, 2006. Each color denotes a different segment or LKF. Due to a limited amount of colors, different segments or LKFs can have the same color. The output of the second reconnection step is the final output of the LKF detection algorithm.

cells, a change in direction compared to the orientation of the last 5 pixels can also terminate the detection cycle: if the angle between the line connecting the centres of the potential new cell and the current cell and the linear fit to the previous 5 pixels of the segment exceeds 45°, the detection cycle is interrupted and the new cell is marked as a new starting point. If the segment is still shorter than 5 pixels, all available pixels are taken into account. We use 5 pixels in contrast to 2 pixels used by Linow & Dierking (2017) to impose a stronger constraint on the curvature. As in the 2 pixel case, a 90° shift of direction is possible within 2 steps of the detection. Within each cycle of the detection algorithm pixels that have been assigned to a segment are removed from the input binary map to prevent double assignments. This procedure is repeated until no new starting cells are found.

After removing all linear segments, the remaining binary map contains only non-LKF pixels or LKFs forming closed contours with no starting points. The closed contours are opened by arbitrarily marking pairs of two neighbouring LKF-pixels (every $(i \cdot 100)$-th and $(i \cdot 100 + 1)$-th LKF-pixel for $i = 1, 2, 3, \ldots$) as starting points. Then the segment detection is repeated until no new starting points are found. The initialization step to open closed contours is then repeated until all LKF-pixels in the binary map are assigned to a linear segment. All segments that were detected are shown in Figure 3.2 (a) for January 1st, 2006.

**Reconnection**

The reconnection instance is designed to connect multiple detected segments that belong to the same LKF. Two segments belonging to the same LKF should have a similar orientation and deformation magnitude and they should be in close proximity to each other. Thus, we compute the probability for all possible pairs of segments to be part of the same LKF based on their distance, their orientation, and their deformation rates. The two segments of the pair with the highest probability are connected and the probabilities of pairs containing one of the two are updated. These steps are iterated until no new matches are found. This part of the algorithm represents a new feature compared to Linow & Dierking (2017).

The central element of the reconnection step is the probability matrix $\mathbf{P} \in \mathbb{R}^{N \times N}$ that stores the probabilities for all pairs of segments with N being the number of segments. The rows and columns correspond to single segments, where $\mathbf{P}(m, n)$ gives the probability of segment $m$ and $n$ being part of the same LKF. The probability is given by

$$\mathbf{P}(m,n) = \sqrt{\left(\left(\frac{\Delta D(m,n)}{D_0}\right)^2 + \left(\frac{\Delta O(m,n)}{O_0}\right)^2 + \left(\frac{\Delta \log_{10} \dot{\epsilon}(m,n)}{\dot{\epsilon}_0}\right)^2\right)},$$

(3.1)

with the elliptical distance $\Delta D$ between the two segments, the difference in orientation $\Delta O$, and the difference of the logarithm of the total deformation rate $\Delta \log_{10} \dot{\epsilon}$. We here use the common logarithm, i.e. log base 10, in contrast to the natural logarithm used in Section 3.3.1 to directly describe the difference in the order of magnitude in the total deformation of two segments. The difference in orientation $\Delta O$ is determined by the angle between the two segments, which are represented in this computation by a line connecting the start and the end point. The elliptical distance describes the distance between both segments, but takes also into account the alignment of the segments. In doing so, we decompose the vector connecting both ends of the segments $\mathbf{v}_{a \to b}$ into a orthonormal basis with one vector parallel to the first segment $\mathbf{a}_{\parallel}$ and one vector perpendicular to it $\mathbf{a}_{\perp}$ as shown in Fig. 3.3. In the same way, $\mathbf{v}_{b \to a}$ is decomposed in a basis for the second segment $\mathbf{b}_{\parallel}, \mathbf{b}_{\perp}$,

$$\mathbf{v}_{a \to b} = \left(\mathbf{a}_{\parallel}, \mathbf{a}_{\perp}\right) \cdot \boldsymbol{\alpha} \quad \overset{!}{=} \quad \mathbf{v}_{b \to a} = \left(\mathbf{b}_{\parallel}, \mathbf{b}_{\perp}\right) \cdot \boldsymbol{\beta}, \qquad (3.2)$$
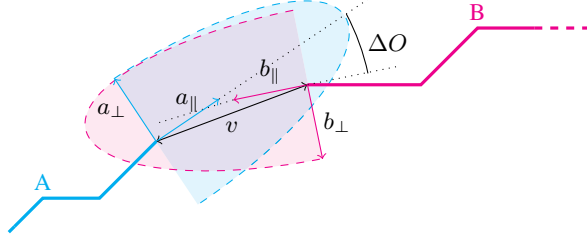
50

**Figure 3.3:** Sketch of two segments $A$ and $B$ illustrating the principle behind the elliptical distance. In the distance computation the component pointing in the direction perpendicular to the segment is weighted by a factor of $e$. Within the shaded area the elliptical distance is below a threshold $D_0$. If the endpoints of both segments lie within the area where both shaded half-ellipses overlap, they are considered for reconnection. The dotted lines indicate the orientation of lines connecting the start and end points of both segments and the angle $\Delta O$ is the difference in orientation. $\mathbf{v}$ is the vector connecting the endpoints of both segments as defined in Eq.3.2. $\mathbf{a}_\parallel$ and $\mathbf{a}_\perp$ are basis vectors aligned in the direction of the segment $A$, respectively $\mathbf{b}_\parallel$ and $\mathbf{b}_\perp$ for $B$.

where $\boldsymbol{\alpha}$ and $\boldsymbol{\beta}$ are the coefficients of the vector decomposition. In the computation of the length of the connecting vector $v$, the component perpendicular to the segment is weighted with an elliptical factor $e > 1$ and the distance computed by both bases is averaged to obtain a symmetrical elliptical distance, that is, $\mathbf{v} = \mathbf{v}_{a \to b} = \mathbf{v}_{b \to a}$:

$$
\begin{aligned}
\|\mathbf{v}\|_e &= \frac{1}{2} \left( \|\mathbf{v}_{a \to b}\|_e + \|\mathbf{v}_{b \to a}\|_e \right) \\
&= \frac{1}{2} \left( \sqrt{\boldsymbol{\alpha}^T \cdot \begin{pmatrix} 1 & 0 \\ 0 & e \end{pmatrix} \cdot \boldsymbol{\alpha}} + \sqrt{\boldsymbol{\beta}^T \cdot \begin{pmatrix} 1 & 0 \\ 0 & e \end{pmatrix} \cdot \boldsymbol{\beta}} \right) \\
&= \Delta D.
\end{aligned}
\tag{3.3}
$$

We consider only pairs of segments where the starting point of one segment lies in the direction of the other segment, that is, $\boldsymbol{\alpha}(0) \geq 0$ or $\boldsymbol{\beta}(0) \leq 0$. Thus points with same elliptical distance lie on a half ellipse centered at the endpoint of the segment as denoted in Fig. 3.3. The computed probability for a generic pair of segments $\mathbf{P}(m, n) = \mathbf{P}(n, m)$ is symmetric, because both the elliptical distance, the orientation difference and the deformation rate difference are symmetric. Thus, we only compute $\mathbf{P}(m, n)$ with $m < n$, where $\mathbf{P}$ is simplified as an upper diagonal matrix.

The parameters $D_0$, $O_0$, and $\dot{\epsilon}_0$ not only normalize the individual components of Eq. (3.1) but also serve as an upper threshold for these components.

If for one pair the elliptical distance $\Delta D$, the difference in orientation $\Delta O$, or the deformation rate $\Delta \dot{\epsilon}$ exceed the threshold $D_0$, $O_0$, and $\dot{\epsilon}_0$ it is not considered for the reconnection. The threshold values will be determined in Section 3.3.2 and are given in Table 3.1.

After initializing the matrix $\mathbf{P}$, the pair of segments with the highest probability $\mathbf{P}\,(m,n)$ is connected and the connected segment $(m \leftrightsquigarrow n)$ replaces the old segment $m$. Thereby the number of segments is reduced by one and the $n$-th row and $n$-th column are removed from the probability matrix $\mathbf{P}$. The elements of the probability matrix that correspond to the segments $m$ need to be updated and thus the $m$-th row and $m$-th column of $\mathbf{P}$ are reevaluated based on the new connected segment $(m \leftrightsquigarrow n)$. This process is iterated, where in each iteration the pair of segments with highest probability is connected, until no pair is left that satisfies the threshold values $D_0$, $O_0$, and $\dot{\epsilon}_0$.

In the final step of the LKF detection algorithm, features that fall below a minimum length $l_{min}$ are removed, because most small features are artifacts of the thinning algorithm and do not represent LKFs. With increasing minimum length, the number of detected LKFs decreases and the field of the detected LKFs shows a higher degree of abstraction. The minimum resolution of the detected LKFs, however, is determined by the minimum length used for the DoG filtering.

The presented reconnection procedure shows better results for longer segments, because the orientation and mean deformation is more sensitive for smaller segments. In theory, the best input would be segments containing all the points in the binary map that lie in between "junctions" of the lines, assuming that all those points belong to the same LKF. The segment detection instance, however, yields smaller segments due to the parallel detection that has been implemented to increase computational efficiency. Thus, we apply the reconnection algorithm twice: the first instance is meant to compensate for the tendency of the segment detection algorithm to divide segments into smaller pieces although they actually belong to the same inter-junction segment. Thus, we use very a restrictive set of threshold values (maximum distance $D_0 = 1.5$ pixels, maximum difference in orientation $O_0 = 50°$, maximum difference in deformation rate $\dot{\epsilon}_0 = 0.75 \log\left(1/\text{day}\right)$, elliptical factor $e = 1$, and minimum length $l_{min} = 2$ pixels) to ensure that only segments are reconnected that are not separated by more than one pixel and no segments are removed because they are short (Fig. 3.2b). The second reconnection in-

**Table 3.1:** List of parameters used in the LKF detection algorithm. For each parameter the lower and upper bound of the optimization is given along with the final choice of the parameter value.

| Parameter name | Symbol | Lower bound | Upper bound | Final choice | Unit |
|---|---|---|---|---|---|
| DoG filtering threshold | $d_{LKF}$ | 0 | 30 | $15^c$ | – |
| max. elliptical distance | $D_0$ | 1 | 7 | $4^b$ | pixels |
| elliptical factor | $e$ | 1 | 5 | 2 | – |
| max. difference in orientation | $O_0$ | 25 | 65 | 35 | $^\circ$ |
| max. difference in deformation | $\dot{\epsilon}_0$ | 0.5 | 1.25 | 1.25 | $\log\left(\mathrm{day}^{-1}\right)$ |
| min. length | $l_{min}$ | 3 | 7 | 3 | pixels |
| min. radius of DoG | $r_1$ | | | $1^{ab}$ | pixels |
| max. radius of DoG | $r_2$ | | | $5^{ab}$ | pixels |

$^a$ parameters that have not been optimized but taken from Linow & Dierking (2017). $^b$ parameters are related to length scales and need to be scaled with the spatial resolution of the input data. $^c$ parameters are used to suppress noise in the input data and need to be adapted individually to input data

stance with a different set of parameters is then used to reconnect segments across junctions, and to generate the final LKFs shown in Fig.3.2 (c). The choice of the set of parameters used in the second reconnection instance is discussed in Section 3.3.2.

## 3.3.2 Parameter selection

There are a number of parameters in the detection algorithm. For some of them the range of possible choices can be narrowed down with information from field and satellite observations as well as theory of ice fracture, but none of them is strictly constrained. Therefore, we attempted an optimization of the set of parameters, mainly of the reconnection step, given in Table 3.1.

The main challenge of the optimization is the strong nonlinearity of the detection algorithm. The main source of non-linearity is the fact that whether a feature is detected or not can depend sensitively on small changes of a

parameter. Another source of non-linearity is the small amount of reference data. The strong non-linearity of the problem constrains both the definition of the cost function and the optimization method to make sure that the optimized solution is the global minimum of the cost function.

We constructed different cost functions, ranging from simple counts of falsely undetected features by the algorithm to a cumulative Modified Hausdorff Distance (MHD) between all detected and hand-picked features as a cost function, in an effort to smooth the strong non-linearity. In addition, we used different non-linear optimization routines including basin-hopping (Wales & Doye, 1997) and a nested brute-force implementation. No combination of cost function and optimization method lead to a satisfying result, because in all cases the cost function was very sensitive to smaller variations of the parameters. We concluded that finding a global minimum of the cost function is impossible. Therefore, we use a set of parameters estimated with a simple brute-force algorithm that minimizes the number of not-detected features for the range of parameters given in Table 3.1, where for each parameter five equally spaced values within its range are used. We do not regard this set of parameters as the global optimum, but rather as a useful working basis given the strong non-linearity of the problem and the limited amount of reference data. The performance of the detection algorithm with this set of parameters is evaluated in detail in Section 3.3.3.

### 3.3.3 Evaluation

In the evaluation we use all data for January 2006 (11 snapshots) from the hand-picked LKF data set, the LKFs detected by the algorithm presented in this study, and LKFs detected by the original version of this algorithm (Linow & Dierking, 2017). The reference data of the original algorithm is generated with the parameters used in the evaluation section of Linow & Dierking (2017). In this way, we evaluate the overall ability of the method to properly detect LKFs but also check whether the modifications and new additions improve the performance of the algorithm. We determine to what degree the algorithms can detect the same features that were recognized by visual inspection and furthermore provide detailed information about the similarity and differences between automatically detected and hand-picked features in an element-wise comparison.

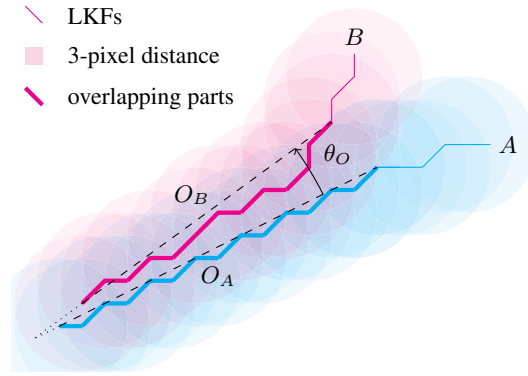The principal idea behind this evaluation is that we compare the features

**Figure 3.4:** Illustration of overlap between two LKFs $A$ and $B$.

pairwise: one LKF from the hand-picked data with the best-matching automated detected LKF. We find the best matching automatically detected feature for each hand-picked feature by minimizing the Modified Hausdorff Distance (MHD) (Dubuisson & Jain, 1994) between the hand-picked features and all automatically detected features. Next, we categorize all pairs by the degree of overlap of the hand-picked feature with its closest matching detected feature. The overlap between two features is illustrated in Fig. 3.4. The number of pixels for which the distance to the closest pixel in the matching feature is smaller than $d_O = 3$ pixels is defined as overlap, labeled as $O_A$ and $O_B$ in Fig. 3.4. To distinguish between the overlap of feature pairs that have similar shape but are displaced and pairs that overlap only due to intersection of both features, we compute the angle between overlapping parts of the matching pairs $\theta_O$. If this angle is smaller than $\theta_O < 25°$, the overlap of a matching pair is defined by the minimum of overlapping pixels of both matching partners normalized by the maximum length of both matching partners:

$$O = \min(\text{len}(O_A), \text{len}(O_B)) / \max(\text{len}(A), \text{len}(B)), \quad \text{for} \quad \theta_O < 25°. \quad (3.4)$$

Given this definition of overlap, we distinguish between three different classes of pairs: (1) *fully matching pairs* that have an overlap larger than 60%, (2) *partly matching pairs* that have an overlap smaller than 60% but larger than 0%, and (3) *not matching pairs* with overlap equal to 0%.

The overall performance of the algorithm with respect to the overlap of the detected features with the reference data-set is given in Fig. 3.5 along with the number of pairs within each class. We find that the features detected with
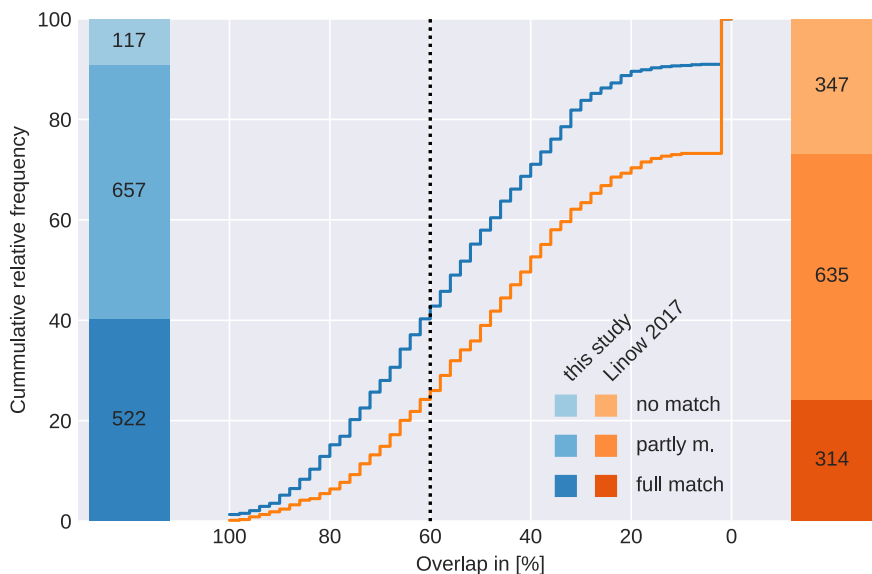
**Figure 3.5:** Evaluation of detection algorithm presented in this study and original algorithm (Linow & Dierking, 2017) against hand-picked LKFs. The cumulative frequency of occurrence of the overlap is given in the center plot. The amount of features is given in the bar plots for each class (fully matching, partly matching, and not matching).

our new algorithm overlap significantly more with the hand-picked reference data than the features detected with the original version of the algorithm (Fig. 3.5). The original version of algorithm is run with the same parameters used in the evaluation section of Linow & Dierking (2017). Our modifications to the algorithm increase the number of fully matching LKFs by 66% (from 314 to 522), along with a similar amount of partly matching LKFs (from 635 to 657), and a clear decrease of 66% for the not matching LKFs (from 347 to 117). This indicates a significant improvement of the original algorithm.

We analyze the similarity of features of all pairs within each class to test whether these improvements are made at the expense of the quality of the detected features. In doing so, we define three metrics to determine the similarity of the features: (1) the mean endpoint distance, (2) the line length error, and (3) the MHD as metrics, where the first two were introduced by Linow & Dierking (2017). The MHD is a measure of the general agreement of two shapes. It takes into account changes in both orientation and length, but also a complete change in shape. In the sea ice context, the MHD is applied,

for example, to evaluate the ice edge position in sea ice forecasts (Dukhovskoy *et al.*, 2015) or to assess the predictability of LKFs (Mohammadi-Aragh *et al.*, 2018). We here only focus on the class of full matching pairs.

For the mean endpoint distance, we determine the distance between both endpoints of the detected and the hand-picked feature for each pair and average them. For all full matching pairs with features detected by our new algorithm the endpoint distance tends to be smaller compared to features detected by the original version of the algorithm, which is indicated by the shift in the distribution towards smaller errors (Fig. 3.6a). The improved match because of the modifications to the original algorithm is also reflected in the smaller mean error (1.47 pixels as opposed to 1.96 pixels of the original algorithm). For 75% of the features detected with our algorithm, the mean endpoint distance is smaller than 2 pixels whereas this is only the case for 60% of features detected by original version.

The line length error is determined by the difference in length of the two features in a pair normalized by length of the smaller feature of the pair. For both algorithms, the distributions are similar with similar mean errors $\sim 18\%$ (Fig. 3.6b). For half of the pairs the line length error is also lower than 15% in both cases.

We find that our modifications to the original algorithm also reduce the average MHD from 1.58 pixels to 1.17 pixels (Fig. 3.6c). 73% of these pairs lie within the 5th to 95th percentile of the background MHD defined as the MHD of the reference data and the morphological thinned binary LKF field (Fig. 3.1f). Since all LKFs consist of sets of pixels from this binary field, the background MHD is an upper limit of how accurate a reconnection algorithm can get using this binary field as an input value.

In conclusion our new version of the algorithm improves the original algorithm in that it detects more features and also increases their agreement with the hand-picked reference data.

### 3.3.4 Discussion

Our adapted detection algorithm greatly improves the original version. The total number of hand-picked features that is reproduced by the algorithm increased by 66%. In addition, the quality of the detected features with respect to their mean endpoint distance, the error in line length and the MHD is improved. We attribute these improvements to two changes that
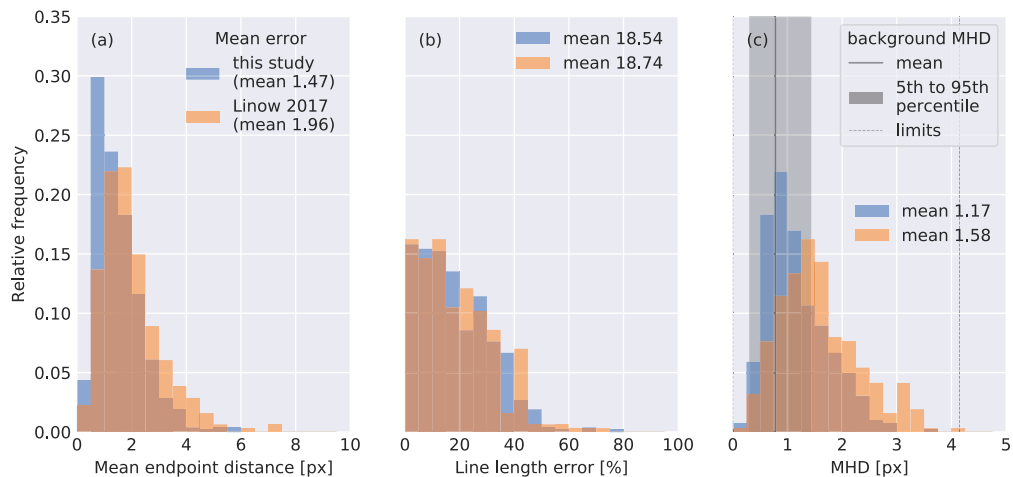
**Figure 3.6:** Statistics of all full matching pairs computed for the algorithm presented here and the original version (Linow & Dierking, 2017): **(a)** the mean endpoint distance, **(b)** the line length error, and **(c)** the Modified Hausdorff Distance (MHD). The background MHD refers to MHD calculated for the hand-picked features and the morphological thinned binary field (Fig. 3.1f).

stand out besides smaller adjustments in the code: (1) the introduction of a probability based reconnection and (2) the optimization of the DoG threshold $d_{LKF}$, which showed the highest sensitivity in the optimization. We use this threshold to filter LKFs as regions that have high deformation rates compared to the local environment. The deformation rates in RGPS are known to be prone to grid scale noise and uncertainties caused by tracking and geolocation errors (Lindsay & Stern, 2003; Bouillon & Rampal, 2015a), which can lead to a false classification of a pixel as LKF. Increasing the threshold slightly suppresses this noise, albeit at the expense of loosing features with smaller deformation rate differences. Thus the threshold needs to be optimized to balance both effects; we found $d_{LKF} = 15$ to be the best parameter choice for the RGPS data set.

In our algorithm we reconnected segments to LKFs based on a probability computed from the characteristics of the segments. Thereby those segments are reconnect that fit "the best" and in contrast to Linow & Dierking (2017) the reconnection does not depend on the order in which the reconnection algorithm runs over the list of segments. In doing so, we improve the quality of the detected features and obtain a unique and consistent solution. Both uniqueness and consistency are necessary ingredients for the ensuing application of a tracking algorithm.

In this context, we found the elliptical distance $\Delta D$ and the orientation $\Delta O$ to be the important contributers to the probability function. The optimized threshold $\Delta \dot{\epsilon}_0 = 1.25$ for differences in deformation rates is very high (as it is applied to the difference of the common logarithm of the deformation rates, a difference between deformation rates of a factor $10^{1.25} = 17.78$ is possible), so that differences in deformation rates are normalized by a large value and do not contribute much to the probability function. Omitting the deformation related part in Eq.3.1 (equivalent to setting $\Delta \dot{\epsilon}_0 = \infty$) does not change the results of the evaluation of the optimized solution very much (not shown here). The small influence of the threshold for deformation rates $\Delta \dot{\epsilon}_0$ on the performance of the algorithm may also be caused by the noise in the RPGS data along LKFs (Bouillon & Rampal, 2015a). Especially smaller segments are affected by the noisy RGPS data so that segments that belong to the same LKF may have different deformation rates.

## 3.4 LKF tracking

The dynamic nature of the ice pack with spontaneous fracture, fast propagation of failure lines, and discontinuous drift fields makes tracking of deformation features in the ice a challenge. Because most of these processes occur on time scales from seconds to days, the temporal resolution of the RGPS data set of 3 days makes feature tracking even more challenging. In this section, we present an algorithm that automatically tracks features and we compare the tracked features to hand-tracked features.

### 3.4.1 Method description

The tracking of deformation features, in fact any feature, between two time records is always a two-step problem: first, the deformation features are detected for both records separately and second, the features of both time records are connected in time by identifying features of the first record with those of the second record.

Between two RGPS time records (3 days) a deformation feature will be advected and can undergo the following changes: (1) it can become inactive, (2) it can grow, or (3) shrink, or it can undergo a combination of growing and shrinking. Thus, on top of two time records, tracking requires drift information between these records. From the same drift fields that were used

to derive the deformation data we estimate a first-guess position of each feature from the first record in the second record that neglects all effects but advection. We compute the drift first-guess position in pixel space (each feature in the first record is described by integer pixel indices) by normalizing the drift speed with the grid resolution. Thus, the computed first-guess positions are given in floating point indices of the input field of the detection algorithm.

For the following description, a tracked feature is a feature from record two with an associated feature in record one; a matching pair is a pair of associated features from records one and two; and all matching pairs are called the tracks.

A tracked feature in the second record is required to overlap at least in part with the first-guess position after growing and shrinking in between the time records is taken into account. We define a search window around the first-guess position of the feature to test for an overlap of the features with the first-guess position. The search window consists primarily of pixels for which the floating point indices of the first-guess position are rounded up and down by the python functions `ceil` and `floor`. To take into account the position uncertainty caused by the morphological thinning algorithm, we also add all neighboring pixels of the pixels with rounded indices using the mean background MHD of the morphological thinned field (Fig. 3.6c) of 0.78 pixels as an estimate for this uncertainty. All features in the second record that include a minimum number of pixels $o_{\min} = 4$ of the search window are marked as potentially tracked features. If we consider a feature that changes shape only due to advection without any growing or shrinking, the tracked feature from the subsequent time record should lie completely within the search window.

During the course of three days, however, many features grow or an opening closes at one or both ends of the detected feature. Also, in rare cases, only parts of a feature close and a new branch is formed within the position of the old feature. This will be referred to as branching. Our algorithm is designed to take into account only growing and shrinking, because to our experience there are rather few branching LKFs (10 %) and because branching is very complex to track. Thus, a feature that is considered as a tracked feature is allowed to grow at both ends compared to the first record or to shrink to only a part of the original feature. To translate this into an algorithm, we define a search area that is the area enclosed by two lines through the endpoints of
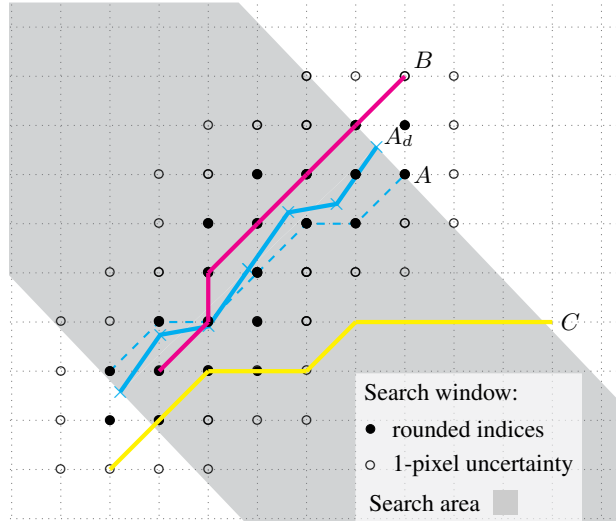
**Figure 3.7:** Principle of the tracking algorithm showing the search area and search window. $A$ is the original feature (dashed blue) and $A_d$ (blue) the first-guess position considering only drift. $B$ and $C$ are two features in the second record, where $B$ is marked as a successfully tracked feature.

the first-guess position. These lines are perpendicular to the orientation of the first-guess position (see grey shaded area Fig. 3.7). For a tracked feature, all points of this feature that lie within the search area need also to lie within the search window. Here, we implement a threshold value $p_{w/a}$ that defines the fraction of points within the search window and points within the search area for the feature to be considered as a tracked feature. Features, for which more pixels lie within the search area but not in the search window, have likely undergone branching or just intersect with the first-guess position but have a different orientation.

The last step of the tracking algorithm filters small features inside the search window that intersect with the first-guess position. Due to their short length all of their points in the search area also lie in the search window. To exclude those we compute the overlap as defined in Sec. 3.3.3 between the first-guess position and the potentially tracked feature. We use a maximum distance of pixels of $d_O = 1.5$ and an angle threshold of $\theta_O = 25°$ for the computation of the overlap. All potentially tracked features with a non-zero overlap are marked as tracked features.

For all features of the first record this procedure is repeated iteratively: (1) advect the feature using the drift information to obtain the first-guess position (2) check for features that share $o_{min}$ pixels with the search window,

**Table 3.2:** List of parameters used in the LKF tracking algorithm. For each parameter the lower and upper bound of the optimization is given along with the final choice of the parameter value.

| Parameter name | Symbol | Lower bound | Upper bound | Final choice | Unit |
|---|---|---|---|---|---|
| min. overlap in search window | $o_{\mathrm{min}}$ | 2 | 6 | 4 | pixels |
| fraction of pixels in search window and in search area | $p_{w/a}$ | 0.5 | 1 | 0.75 | – |
| max. distance of pixels for overlap | $d_O$ | 0.75 | 2.25 | 1.5 | pixels |
| max. angle for overlap | $\theta_O$ | 15 | 35 | 25 | ° |

(3) compute the fraction of pixels in the search window and in the search area $p_{w/a}$, and (4) test for non-zero overlap. The output of the tracking algorithm is a list of matching pairs of always one feature from the first record and a tracked feature from the second time record.

## 3.4.2 Parameter optimization

In the tracking algorithm the four parameters $o_{\mathrm{min}}$, $p_{w/a}$, $d_O$, and $\theta_O$ are not very well constrained, so we attempt to optimize them within plausible bounds. As we want to optimize the tracking algorithm independently of the detection algorithm, we use the hand-picked features as input for the tracking algorithm and compare the output to the hand-tracked features. We perform the same very basic optimization as in Sec. 3.3.2 facing similar problems with limited amount of reference data and a non-linear cost function. We choose equally spaced values in the range given in Table 3.2 for all four parameters and determine the number of correctly tracked features, the missed tracks, and false positives. We find that decreasing $o_{\mathrm{min}}$ and increasing $p_{w/a}$, $d_O$, and $\theta_O$ leads to an increase in correctly tracked features along with a large increase of false positives. To balance both effects, we define the cost function as the number of correctly tracked features subtracted by the number of missed tracks and the number of false positives. The final parameter set that maximizes this difference is given in Table 3.2.

### 3.4.3 Evaluation

To separate the two steps of feature tracking, and to enable an independent evaluation of the tracking algorithm, we apply the tracking algorithm on two different LKF data-sets: the hand-picked features and the features extracted by the detection algorithm for the same time span. Then, we compare both results to the hand-tracked features described in Sec. 3.2.3.

We evaluate the tracking algorithm independently by applying it to the hand-picked features and test whether the algorithm reproduces the hand-tracked features of the next time record, hereafter referred to as "only tracking". The algorithm picks 336 (85.7%) of the overall 392 hand-picked tracked features correctly and only misses 56 (14.3%). Besides the missed tracks, the algorithm detects 89 false positives. We use the information describing the type in change of shape (no change, growing, shrinking, and branching) provided for the hand-picked tracks to test the performance of the algorithm for those different types of change (Fig. 3.8a). The performance of the algorithm ranges from 85% to 88% for the different types with the branching type being an exception, for which only 56% of the features are tracked correctly. This is not surprising as the algorithm is not designed to track this type of change.

In the evaluation of both the detection and tracking algorithm, we distinguish between missed tracks that were not tracked by the tracking algorithm and tracks that were missed, because the detection algorithm was not able to detect the corresponding features in both time records. First, we test whether the detection algorithm picks both features of a hand-picked matching pair. In doing so, we separate both features into the parts that both features share and a non-overlapping part, to account for varying shapes in the non-overlapping part of detected and hand-picked feature. Then, we check whether detected features correspond to the hand-picked features using the overlap as in Sec. 3.3.3. If for one of the two hand-picked features no corresponding detected feature is found, this hand-picked tracked feature is marked as a missed tracked feature caused by the detection algorithm. Otherwise, we test whether the tracking algorithm tracks the detected features appropriately. In total, 54.1 % of the hand-picked matching pairs are detected and tracked correctly, whereas 21.6 % are not captured by the tracking algorithm, and for 24.4 % of the tracked features the corresponding features are not detected. Interestingly, these fractions do not change significantly if
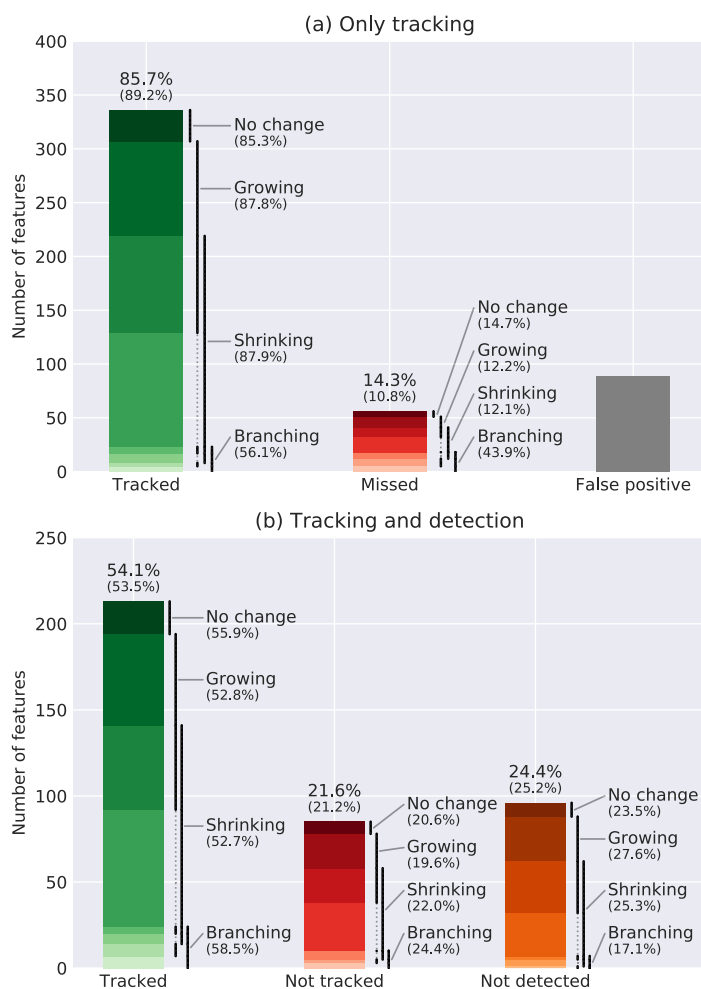
**Figure 3.8:** Evaluation of **(a)** only tracking algorithm on the hand-picked features and **(b)** combination of detection and tracking algorithm. The colored segments of each bar show the different combinations of changes in shape (no change, growing, shrinking, and branching) that are labeled by the black lines next to the bar. The missed tracks in **(b)** are separated into not detected or not tracked features. Above the bars the percentage compared to all hand-picked tracks is given for all types and for all types except branching, which is given in brackets.

sub-sampled to individual types of change. Only for the branching type of tracks, the rate of tracked features missed by the tracking algorithm exceeds the one for the detection algorithm, which is in line with the low amount of matching pairs captured by the tracking algorithm for this type of change found in the evaluation of the tracking algorithm alone.

Since not all hand-picked tracked features are tracked automatically by the presented algorithm, we need to make sure that this does not change the temporal characteristics of the automatically generated tracked features. In doing so, we compare the distributions of lifetimes (Fig. 3.9) and growth rates (Fig. 3.10) of the hand-picked tracked features (hand-picked), the automatically tracked features of the hand-picked features (only tracking), and the automatically tracked features of the automatically detected features (tracking and detection). At the beginning of the evaluation period, all features are initialized with a lifetime in the class of 0 to 3 days, where the range of the class is given by the temporal resolution of the input data. The following

**Figure 3.9:** Distribution of lifetime of all features in the first 12 RGPS snapshots in 2006 in the hand-picked reference data **(left column)**, the automatically tracked features of the hand-picked features **(middle column)**, and the automatically tracked features of the automatically detected features **(right column)**. The lower row shows the absolute number of features for a certain lifetime class, whereas the upper row is normalized by the total number of features for this time record.

time steps, all features that are marked as tracked features are assigned to the next lifetime class compared to the class of their tracking partner in the previous time record. All other features are initialized again in the lowest category 0 to 3 days. For all three different data sets, more than 99% of features have a lifetime smaller than 12 days, which can be thought of as the average spin-up time needed by the tracking algorithm. In the following, we consider only the period after those 12 days.

The distribution of lifetimes for the hand-picked tracks and automatically generated tracks of hand-picked features are very similar: (1) the number of features in the lowest lifetime category increases in absolute and relative numbers to the end of the evaluation period in a equal manner (70 % to 81 % (hand-picked) and 67 % to 78 % (only tracking)), (2) 17 % (hand-picked) and 18 % (only tracking) of the features have a lifetime of 3 to 6 days, and (3) in both cases the remaining 9 % of the features have a lifetime over 6 days. In
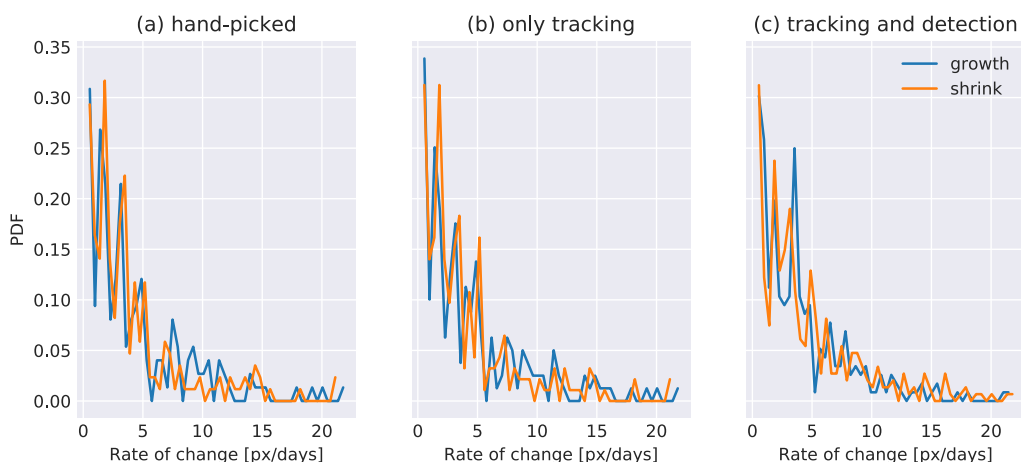
**Figure 3.10:** Probability distribution function for growth rates in **(a)** the hand-picked reference data, **(b)** the automatically tracked features of the hand-picked features, and **(c)** the automatically tracked features of the automatically detected features separated into growth for positive growth rates and shrink for negative values.

a feature-by-feature comparison for both data sets, only 10 % of the features vary in their lifetime due to uncertainties in the tracking algorithm. The root mean square error of the lifetime is estimated to be 1.55 days. For the automatically detected and tracked features the average lifetime reduces to 3.9 days compared to 4.2 days for the hand-picked features, which is driven by an increase in the amount of features in the lifetime class 0 to 3 days to 81 %. The fractions of the remaining classes are reduced accordingly, but do not change significantly relative to each other.

Besides the lifetime as the main temporal characteristic, we compute the growth rates of all tracked features, to check whether the shape of the tracked features changes in a similar manner. The growth rate is defined as the difference of the number of pixels of the feature in the second record compared to the feature of the previous record. In our analysis, we divide the growth rate into two regimes depending on its sign: growth of the feature for positive values and shrinking of the feature for negative values. The distributions of the growth rates for the "hand-picked", "only tracking", and "tracking and detection" data sets all have an exponential distribution (Fig.3.10) with half of the features changing by less than 3 pixel per day. The high order of similarity of the distributions indicates that the usage of the detection and tracking algorithm does not distort the characteristics of tracked features, even though the total number of features detected and

tracked increases by a factor of 2.3 for the detection and tracking data-set.

### 3.4.4 Discussion

The large time difference of 3 days between records of the RGPS data set significantly complicates the tracking of deformation features because they change shape and positions on shorter time-scales. With this background, the overall percentage of 85.7 % of hand-picked tracked features that were correctly identified by the algorithm is more than satisfying. The missed tracks and the false positives of the algorithm lead to a lifetime RMSE of 1.55 days, which is smaller than the uncertainty given by the 3 day temporal resolution of the input deformation data. The low percentage of correctly identified branching features is also acceptable because they only make up 10 % of all hand-picked features. We hypothesize that relaxing the constraints in the algorithm to also track branching features will most likely lead to a strong increase in false positives.

Also the combination of tracking and detection algorithm reproduces more than half of the hand-picked tracks. This exceeds the 40 % of features that were fully detected by the detection algorithm and might hint at a better performance of the algorithm for long-lived features. The hand-picking of features and tracks by only one individual also leads to a bias in the reference data. To accurately separate the uncertainty caused by the subjectiveness of the reference data from the uncertainty of the algorithm, more individuals would need to repeat the hand-picking procedure, which would exceed the scope of this manuscript. Especially, small LKFs and LKFs in regions of low deformation are harder to catch by eye (Linow & Dierking, 2017), which explains that the automatic detection picks 2.3-times more features than in the reference and the number of tracked features increases by 65 %. We assume that this bias towards small and therefore most probably short-lived features is responsible for the slightly higher percentage of features in the class with the lowest lifetime (0 to 3 days). Besides this small increase, the distributions of lifetimes for the automatically detected and tracked features are very similar, which suggests that there is no significant cumulative bias caused by the application of both algorithms. This is backed by the similar growth rates observed for both data sets.

## 3.5   LKF data-set

### 3.5.1   Generation of LKF data-set

In this section, we introduce a data-set of LKFs generated by applying the detection and tracking algorithm to all available RGPS data. The RGPS data covers the time from November 1996 to April 2008. Here, we use the available winter data from late freezing season (November/December) to the start of the melt onset (April/May). The Lagrangian drift information that is also provided in the RPGS data set is interpolated to the regular grid used for the RGPS deformation data to be used as input in the LKF tracking.

First, we apply the detection algorithm with the optimized parameters given in Table 3.1 to all deformation data. The output of the detection algorithm is a list of LKFs for each time record that includes one array for each LKF. The array stores the position (as index in the RGPS grid and in lat/lon-coordinates) and deformation (divergence and shear rate) information of all points of the LKF. Next, we feed the interpolated drift information and the detected LKFs of each year to the tracking algorithm and determine the linkages between LKFs for successive time records. The tracking algorithm with the optimized parameters given in Table 3.2 provides a list of tracked pairs. Each pair contains the indices of the LKFs in record one and two.

Overall 164 698 LKFs were detected and 35 855 tracked features were found. The yearly detection numbers range from 11 002 LKFs for the winter 2006/07, the year of a sea-ice minimum, to 16 774 LKFs in winter 2001/02. If the number of detected features is normalized by the number of observations of sea-ice deformation, we find the maximum for winter 1996/97 and the minimum in 2002/03. The number of tracks vary from 2 012 tracks in winter 2003/04 to 4 127 tracks in winter 2001/02.

The deformation, more precisely the divergence rate, which is saved for each LKF, can be used to distinguish leads from pressure ridges in the generation of an LKF. In general, leads form in divergent and pressure ridges in convergent ice motion and the converse of this relation can be used to label newly formed LKFs. Persistent LKFs can also be labeled in this way, as long as the sign of divergence does not change during the lifetime of an LKF. Consider an LKF, initially labelled as a lead in divergence, that encounters convergent motion. Depending on the magnitude of convergence, the lead may either only partly close and continue to be an open lead, or it may close

completely and even evolve into a pressure ridge, making differentiating be-
tween leads and ridges difficult. Thus, we refrain from labeling all LKFs in
the data-set into leads and pressure ridges, but provide the deformation rates
for each LKF and leave this classification and its evaluation to the informed
user. As an approximate first-guess, we estimate that 46% of the LKFs in
the data-set are leads, 41% are pressure ridges, and 13% are unclassified
(because the associated mean divergence rate along the LKF changes sign
over the lifetime of the LKF). For the classified leads and pressure ridges
the sign of divergence does not change over the lifetime. Please note, that
these estimates especially for short LKFs are likely contaminated with grid-
scale noise in the divergence data of RGPS (Lindsay & Stern, 2003; Bouillon
& Rampal, 2015a). Combining the LKF data-set with sea-ice thickness and
concentration data would allow to clearly distinguish between leads and pres-
sure ridges by using these additional constraints: (1) along a lead the sea-ice
concentration decreases within the time step, and (2) along pressure ridges
the sea-ice thickness increases.

## 3.5.2 Applications and Discussion

In this section, we present a few illustrative statistics of the LKF data-set.
In doing so, we intend to demonstrate the usefulness of the data-set but also
to check it for consistency with other studies on leads and sea-ice deforma-
tion. The statistics (Fig. 3.11) range from spatial properties such as LKF
length, LKF density and intersection angles, to temporal properties such as
LKF lifetimes. In case of the intersection angle, we give an example for a
model-observation comparison with the presented algorithms by comparing
the RGPS LKF data-set to LKFs that were detected and tracked in a 2-km
model simulation with a numerical sea-ice ocean model. In addition, we link
the number of deformation features and its corresponding deformation rates
to atmospheric drivers, in particular to Arctic cyclones.

The density of LKFs is computed for the all years of the LKF data set
as the incidences when a pixel is crossed by a LKF normalized by the overall
number of RGPS observations for this pixel. In Fig. 3.11 (a) only pixels
that have more than 500 RGPS observations are shown. We observe a fairly
homogeneous LKF density throughout the entire Amerasian basin, with a
slight increase in the Beaufort Sea. The fast ice regions in the East Siberian
Sea have the lowest densities with the fast ice edge showing up as a sud-
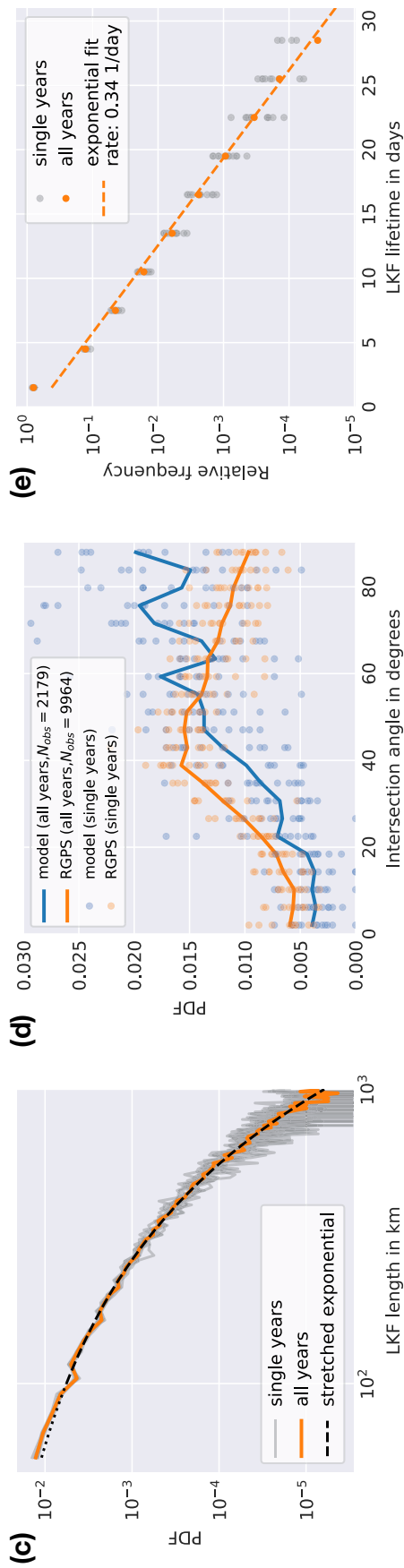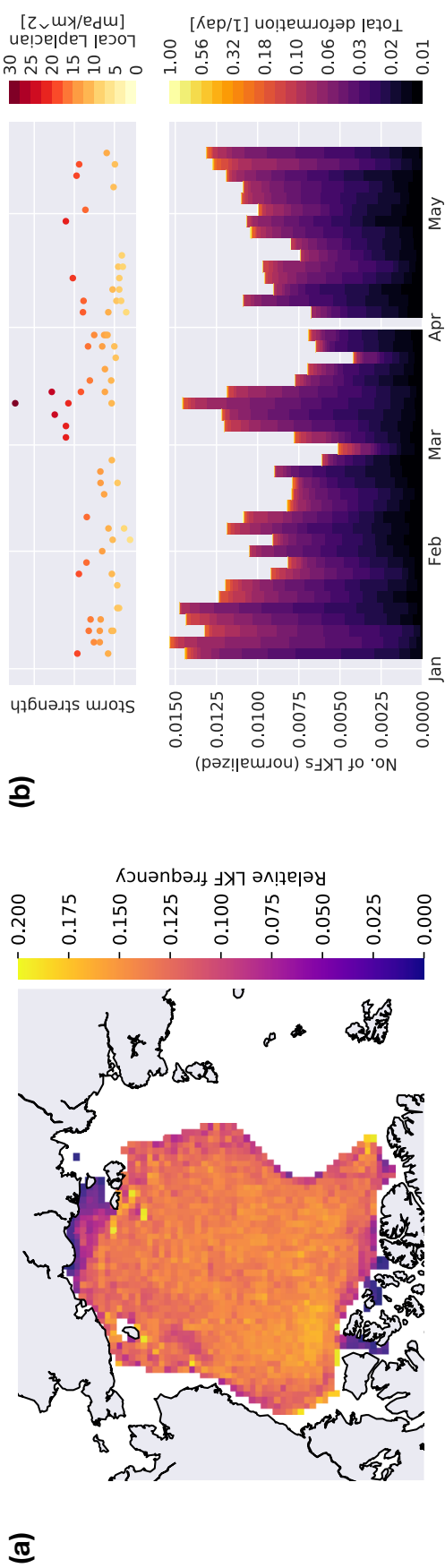
**Figure 3.11:** Statistics on LKF data-set: **(a)** LKF density computed for the all years of the data-set. **(b)** Time series of the number of LKFs separated by their deformation rates for winter 2002/03. The number of LKFs is normalized by the number of available pixels for each RGPS time record. For early April no RGPS data is available. For each time record all cyclones (Serreze, 2009) over the Arctic ocean are each shown as a dot in the upper panel. The y-axis and the color-code of the dots in the upper panel provide the local Laplacian of each cyclone as a proxy for its strength. **(c)** PDF of LKF length along with stretched-exponential fit for LKFs larger 100 km and smaller 1000 km. **(d)** Intersection angle of pairs of features that are newly formed (lifetime between 0 and 3 days) and have size of at least 10 pixels for the RGPS and a 2-km Arctic numerical model simulation. **(e)** Distribution of LKF lifetimes for all years along with a fit to an exponential tail.

den increase in LKF density. The highest LKF densities are found around the New Siberian Islands, Wrangel Island, and at the coastlines along the Beaufort Sea. This agrees very well with studies on lead densities derived from MODIS thermal-infrared imagery (Willmes & Heinemann, 2016) and CyroSat-2 data (Wernecke & Kaleschke, 2015) that show high densities in the Beaufort sea and highest values close to the coastline. A direct comparison of density values is not possible as those studies are limited to leads that are identified as an opening in the ice cover, whereas our algorithm picks regions of high deformation rates that can also include pressure ridges.

The distributions of LKF length of all single years are very similar and range from $\sim 50\,\mathrm{km}$ to $1000\,\mathrm{km}$ (Fig. 3.11c). For LKF lengths between 100 and $1000\,\mathrm{km}$, a stretched exponential, $p(x) = Cx^{\beta-1}\mathrm{e}^{-\lambda x^{\beta}}$ with $C = \beta\lambda\mathrm{e}^{\lambda x_{min}^{\beta}}$ (Clauset $et\ al.$, 2009), accurately describes the PDF. The parameters $\beta = 0.719$ and $\lambda = 0.0531$ are determined by finding numerically the maximum likelihood estimate. We perform a goodness-of-fit test for power-law distributed data that is based on the Kolmogorov-Smirnov (KS) statistic, which is the maximum distance between the cumulative distribution functions (CDF) of two different distributions (Clauset $et\ al.$, 2009). We draw random samples from the fitted distribution and compute the KS of the random samples and the fitted distribution. This simulation is repeated 1000 times. We find that the KS of the observed length scales is smaller than the 95% percentile of the random samples and thereby the observed LKF lengths are described by the fitted distribution. The stretched exponential distribution belongs to the family of heavy-tailed distributions, and is the transition of an exponential and a power-law distribution. It describes many natural phenomena that are dominated by extreme events but in contrast to power-law distribution have a natural upper limit scale (Laherrère & Sornette, 1998). We limit the range of the fit to $1000\,\mathrm{km}$ due to the varying coverage and especially smaller gaps in the RGPS data that might divide long features into multiple smaller segments. We set the lower bound to $100\,\mathrm{km}$ to account for the discrete character of the LKF length that disturbs the distribution at lower LKF lengths. As LKFs here are collections of pixels, their length is set by a linear combination of $\left(i + \sqrt{2}j\right) \cdot 12.5\,\mathrm{km}$ with $i, j \in \mathbb{N}$.

The intersection angle between two deformation features formed at a similar time is related to the rheology describing the deformation of sea-ice. From satellite imagery in the visible range for 14 days in 1991, the intersection an-

gle was found to range between 20° and 40° (Walter & Overland, 1993), which can be linked to the angle of internal friction using a Mohr criterion for failure (Erlingsson, 1988). The distribution of intersection angles of two LKFs that formed in the same time record is given in Fig. 3.11 (d), where only LKFs larger than 10 pixels=125 km are taken into account to reduce the effect of a preferred direction (45° and 90°) originating from the rectangular grid. We perform this analysis on the RPGS LKF data-set and LKFs that were detected in a 2-km Arctic numerical model simulation, whose details are given in Appendix B.1. For the RGPS data, we find that the distribution peaks at an angle of 40°−50°. Angles larger 50° occur more often than angles below 40°, and angles between 0°−20° have the lowest occurrence. The broad distribution indicates that there is not only one specific fracturing angle, but that heterogeneities in the ice cover and temperature variations (Schulson & Hibler, 2004) as well as the dilatancy effect (Tremblay & Mysak, 1997) may influence the deformation on an Arctic-wide scale. The LKFs in the model simulation intersect at larger angles with local maxima in the range 60° to 90°. The difference in the sample size might cause these strong variations for larger angles, as we find five times fewer features in the model simulation than for RGPS within the same period of time. In general, the model underestimates the probability of intersection angles smaller 55° and overestimates those of angles larger than 55°. We attribute these differences to the usage of the elliptical yield curve with normal flow rule in the simulation, because this yield curve does not have a "preferred" direction of fracture in contrast to yield curves with a Mohr-Coulomb criterion. The intersection angle may be improved by an appropriate choice of model parameters (Ringeisen *et al.*, 2019).

The distribution of lifetimes determined by the tracking algorithm shows an exponential tail with a rate parameter of $0.34\,\mathrm{day}^{-1}$ (Fig. 3.11e). Kwok (2001) described some LKF systems that were persistent in the Arctic over a period of a month for the winter of 1996/97. We also find lifetimes as high as this, but show that the majority of LKF are active in much shorter time intervals. We assume that the rapid changes in external forcing (mainly wind stress) are the reason for the high amount of short-lived LKFs.

Last, we study the link between the detected features and the wind forcing being the main driver of ice fracture. To do so, we combine a data-set of cyclones in the Northern Hemisphere (Serreze, 2009) with the distribution of LKFs in different deformation rate classes for, as an example, the winter

of 2002/03 (Fig. 3.11 b). In the freezing season, we find more deformation features (with generally higher deformation rates) caused by the thinner and therefore weaker ice during this period. With thicker ice the number of deformation features decreases followed by an increase from April onwards which we attribute to the onset of melting and the resulting weakening of the ice. This overall seasonal cycle is interrupted by a set of four strong cyclones that pass through the Arctic Oceans in March and lead to a sudden increase of the number deformation features. This confirms that weather systems with high wind speeds are a main driver of sea-ice deformation in the Arctic Ocean. The deformation rates associated with the LKFs co-varies with the seasonal cycle of the number of LKFs, which is in agreement with the seasonal cycle of the mean deformation rate (Stern & Lindsay, 2009).

## 3.6 Conclusions

The new detection algorithm presented in this study follows the structure of the original algorithm (Linow & Dierking, 2017) with classifying LKF pixels in the input deformation rates and then detecting single deformation features. In doing so, an additional degree of abstraction is added compared to studies using only skeletons of leads (Banfield, 1992; Van Dyne & Tsatsoulis, 1993; Van Dyne *et al.*, 1998). This enables not only the extraction of feature-based information such as intersection angles and LKF length but also the tracking of the features. In addition, avoiding classified, that is, preprocessed and charted, SAR imagery (Banfield, 1992; Van Dyne & Tsatsoulis, 1993; Van Dyne *et al.*, 1998) provides the opportunity to apply the algorithm to both model output and satellite observations. For instance, Koldunov, Danilov, Sidorenko, Hutter *et al.* (2019) apply the algorithm directly to sea ice thickness as an input field to study the impact of solver convergence on the cumulative effect of deformation features. Still, the algorithm can also be applied to classified imagery, if the first filtering steps are skipped and the classified imagery is used as the binary LKF map (like Fig 3.1e).

The evaluation of the detected features shows that introducing a probability based reconnection instance improves both the number of correctly detected features and their quality. Here, the input of distance and differences in orientation are the most important contributions if we consider the

high threshold for difference in deformation resulting from the parameter optimization. We only performed a brute-force optimization of the parameters of the detection algorithm for a small parameter space limited by the strong non-linearity of the detection itself and the small amount of reference data. For a thorough optimization a larger reference data-set is required.

The design of a new tracking algorithm is outlined. The tracking algorithm handles the dynamic nature of sea ice as well as the low temporal resolution of satellite drift data. The algorithm takes advection as well as growth and shrinking of deformation features appropriately into account (86 % of the hand-picked tracks are found correctly). The algorithm recognizes the opening of secondary leads (branching) at a lower rate (56 %), but one needs to bear in mind the higher uncertainty of those features in the hand-picked data set and their generally smaller number. The performance of the combination of detection and tracking algorithm is also satisfactory and does not bias the statistics of the features. Roughly 20-30 % of the detected features are tracked. Consequently, the remaining 70–80% of the features persist for less than 3 days. Sea-ice deformation at higher sampling rates, for example, derived from ship radar with a sampling rate of up to 10 minutes (Oikkonen *et al.*, 2017), would be necessary to study LKF lifetimes at these shorter time scales.

We split the task of finding a deformation feature and following it with time in a spatio-temporal deformation data-set into two subroutines: (1) detection features in the deformation field of one time step and (2) finding the temporal connection between individual detected features of subsequent time steps. In doing so, both subroutines are independent of each other, although we speculate that information of the temporal evolution of sea ice deformation could in turn improve also the detection of features. For this task, machine learning techniques, which have recently attracted attention in the climate science context (see for instance Ashkezari *et al.*, 2006, for oceanic eddy detection), are a promising tool to explore.

The LKF data-set generated by automated LKF detection and tracking from the RGPS sea-ice deformation data includes $\sim 165\,000$ LKFs from 12 winters. These are significantly more deformation features than can be found in previous, hand-picked lead data sets (e.g. Miles & Barry, 1998). Due to the use of drift observation derived from SAR-imagery, the data-set is also not limited to clear-sky conditions. This object-based data set enables statistics of both the overall LKF field, like LKF density, and of

single LKFs, like length, intersection, curvature, etc. In addition, all of these statistics can be combined, linked and used as filter criteria. Along with the age estimated by the tracking algorithm, the data-set makes a comprehensive and quantitative description of deformation features in Arctic Ocean possible and complements qualitative studies (Kwok, 2001).

The algorithms are designed in a flexible way so that they can be applied to any sea-ice drift and deformation data, or classified imagery. For example, the current RGPS LKF data-set could easily be extended until today with operational drift data derived from Envisat and Sentinel-1 (Pedersen *et al.*, 2015). Also, resolved leads in high-resolution Arctic model simulations can be analyzed to compare LKF properties to the LKF data set. We have shown a first example of comparing intersection angles of LKFs. Comparing the characteristics of deformation features directly makes a thorough evaluation of lead-resolving sea-ice models possible instead of focusing on only one property such as lead density (Wang *et al.*, 2016) and also facilitates the complicated interpretation of scaling analysis of sea-ice deformation that has been used for this purpose so far (Rampal *et al.*, 2016; Hutter *et al.*, 2018).

# 4. Feature-based evaluation of sea-ice deformation in lead-resolving sea-ice simulations[1]

**Abstract** The sea-ice modelling community progresses towards Pan-Arctic simulations that explicitly resolve leads in the simulated sea-ice cover. Evaluating these simulations against observations poses new challenges. A new feature-based evaluation of simulated deformation fields is introduced and the results are compared to a scaling analysis of sea ice deformation. Leads and pressure ridges – here combined into Linear Kinematic Features (LKF) – are detected and tracked automatically from deformation and drift data. LKFs in two Pan-Arctic sea-ice simulations with a horizontal grid spacing of 2 km are compared with an LKF data set derived from the RADARSAT Geophysical Processor System (RGPS). One simulation uses a 5-class Ice Thickness Distribution (ITD). The simulated sea-ice deformation follows a multi-fractal spatial and temporal scaling as observed from RGPS. The heavy-tailed distribution of LKF lengths and the scale invariance of LKF curvature, which points to the self-similar nature of sea-ice deformation fields, is reproduced by the model. Interannual and seasonal variations of the number of LKFs, LKF densities, and LKF orientations in the ITD simulation are found to be consistent with RGPS observations. The lifetimes and growth rates follow a distribution with an exponential tail. The model overestimates the intersection angle of LKFs, which is attributed to the model's viscous-plastic rheology with an elliptical yield curve. In conclusion, the new feature-based analysis of LKF statistics is found to be useful for a comprehensive evaluation of simulated deformation features, which is required before the simulated features can be used with confidence in the context of climate studies. As such it complements the commonly used scaling analysis and provides new useful information for comparing deformation statistics. The ITD simulation is shown to reproduce LKFs sufficiently well to be used for studying the effect of directly resolved leads in climate simulations. The feature-based analysis of LKFs also identifies specific model deficits that may be address by specific parameterizations, for example, a damage parameter, a grounding scheme, and a Mohr-Coulombic yield curve.

## 4.1   Introduction

Current efforts in the sea-ice modeling community push sea-ice models to Pan-Arctic lead-resolving sea-ice simulations. In these simulations, the Arctic ice cover consists of individual "floes" that are formed by strongly localized

deformation along the emerging floe boundaries. There are two approaches to obtain such a behaviour: (1) a very fine grid-spacing ($< 5\,\text{km}$) and the classic viscous-plastic (VP) rheology (Hutter *et al.*, 2018; Wang *et al.*, 2016; Spreen *et al.*, 2016) or (2) new rheological frameworks (e.g. Maxwell elasto-brittle (MEB), Dansereau *et al.*, 2016). The emergence of deformation features, which can be identified as leads and pressure ridges, calls for a proper evaluation of model simulations against observations. This is challenging because ice mechanics are non-linear and chaotic. A direct comparison of deformation fields bears similar issues as comparing eddy resolving ocean model simulations to high-resolution satellite observations. Therefore, it should not be attempted (Mourre *et al.*, 2018). Still, proper LKF characteristics in sea ice models are important in the context of Arctic climate.

Resolving leads in sea-ice simulations opens up new possibilities in Arctic climate research and sea-ice forecasting. Leads are openings in the sea-ice cover where direct atmosphere-ocean processes are strong. A sea-ice component including leads allows for the direct simulation of these interactions in regional or global climate models. The distribution of leads also has a strong impact on the local drift field. Reliable short-term sea-ice drift forecasts will therefore depend on the model's capacity to simulate and initialize fields with localized deformation. The increasing economic interest in the Arctic (e.g. shipping, Eguíluz *et al.*, 2016) requires skillful predictions in these remote regions (Jung *et al.*, 2016) to prevent environmental catastrophes and to organize search and rescue operations. A realistic representation of deformation features in sea-ice models is the prerequisite of both applications.

In the past, high-resolution sea-ice simulation were mostly evaluated with respect to their simulated deformation fields. Here, calculating scaling characteristics of sea-ice deformation was the most common method (Girard *et al.*, 2009; Rampal *et al.*, 2016; Spreen *et al.*, 2016; Bouchat & Tremblay, 2017; Hutter *et al.*, 2018). The scaling statistics make use of the observed power-law scaling of sea-ice deformation (Marsan *et al.*, 2004) and determine the degree of heterogeneity and intermittency of sea-ice deformation for satellite observations and model simulations (Rampal *et al.*, 2016; Hutter *et al.*, 2018). The underlying idea of these metrics is that the presence of extreme values and strong localization in sea-ice deformation indicates a realistic representation of deformation features.

While scaling characteristics give insight into the underlying material properties of sea ice, their interpretation with respect to deformation features

is not straightforward (Bouchat & Tremblay, 2017; Hutter *et al.*, 2018), so that these metrics cannot be used for evaluating the simulated deformation features themselves. A comprehensive description of deformation features requires the detection of single deformation features to extract statistics such as density, orientation, intersection angle, and persistence. A new LKF detection and tracking algorithm (Hutter *et al.*, 2019) identifies single LKFs in deformation data both derived from satellite observations and simulated by sea-ice models. The resulting data set provides ample opportunity to compare various spatial characteristics and the temporal evolution of LKFs.

The objective of this paper is to establish a feature-based evaluation of sea-ice deformation in lead-resolving sea ice simulations. We apply the LKF detection and tracking algorithm of Hutter *et al.* (2019) to two different sea-ice simulations with a horizontal grid-spacing of 2 km, of which one uses an Ice Thickness Distribution (ITD). We compare the extracted LKFs to an LKF data set derived from RADARSAT Geophysical Processor System (RGPS) deformation data (Hutter *et al.*, 2019) with respect to their Pan-Arctic distribution (density and orientation), their spatial properties (length, curvature, and intersection angle), and their temporal characteristics (persistence and growth rates). In addition, we test which inferences for the overall appearance of LKFs can be made from a spatio-temporal scaling analysis (following, e.g. Rampal *et al.*, 2016; Hutter *et al.*, 2018) of sea-ice deformation. By analyzing two different model simulations, we study how changes to the model physics, in our case the explicit ridging processes in an ITD model, affect the simulated LKFs, and how the different analysis methods pick up that difference.

## 4.2 Methods

### 4.2.1 LKF detection and tracking algorithms

Our LKF detection and tracking algorithms (Hutter *et al.*, 2019) splits the detection of LKFs in sea-ice deformation fields into three steps: (i) the algorithm classifies pixels with locally higher deformation rates as LKF pixels, (ii) it separates the LKFs in a global binary map into minimal LKF-segments, and (iii) it re-connects multiple minimal segments into individual LKFs based on a probability that is determined by their distance, their orientation relative to each other, and their difference in deformation rates.

The tracking algorithm combines the detected LKFs of two subsequent time records with the drift information between the two records to track individual LKFs over time. First, the algorithm advects the LKFs from the first time record according to the drift information to obtain a first-guess positions for the LKFs. Then, tracked LKFs in the second record are identified by the degree of overlap between the advected LKFs and the detected LKFs of the second time record.

## 4.2.2  RGPS LKF-dataset

The deformation data of the RADARSAT Geophysical Processor System (RGPS, Kwok, 1998) was processed by the LKF detection and tracking algorithms (Hutter *et al.*, 2019) to produce a comprehensive data set (`https://doi.org/10.1594/PANGAEA.898114`, Hutter *et al.*, 2019). The data set contains LKFs in the winter months (November to May) from 1996 to 2008 and covers large parts of the Amerasian Basin in the Arctic Ocean. In total the data set contains 165 000 detected LKFs and 36 000 tracked LKFs.

## 4.2.3  Model simulations

### Model configurations

Both simulations in this paper are based on a regional Arctic configuration (Nguyen *et al.*, 2012) of the Massachusetts Institute of Technology general circulation model (MITgcm, Marshall *et al.*, 1997; MITgcm Group, 2017), but with a refined horizontal grid spacing of 2 km. The number of vertical layers is reduced to 16 with the first five layers covering the uppermost 120 m to decrease computational cost associated with the ocean model component as we are only interested in sea-ice processes. The Refined Topography data set 2 (RTopo-2) (Schaffer & Timmermann, 2016) is used as bathymetry for the entire model domain. The lateral boundary conditions are taken from the globally optimized ECCO-2 simulations (Menemenlis *et al.*, 2008b). We use the 3-hourly Japanese 55-year Reanalysis (JRA-55, Kobayashi *et al.*, 2015) with a spatial resolution of 0.5625° for surface boundary conditions. In the baseline simulation, the ocean temperature and salinity are initialized on January 1st, 1992 from the World Ocean Atlas 2005 (Locarnini *et al.*, 2006; Antonov *et al.*, 2006). The initial conditions for sea-ice are taken from the Polar Science Center (Zhang *et al.*, 2003). Ocean and sea ice parameteriza-

tions and parameters are directly taken from Nguyen *et al.* (2011a) with the ice strength $P^\star = 2.264 \cdot 10^4 \, \text{Nm}^{-2}$. The baseline simulation uses the classical discrimination of two ice classes: thin and thick ice (Hibler, 1979). The momentum equations are solved by an iterative method and Line Successive Relaxation (LSR) of the linearized equations following Zhang & Hibler (1997). In each time step ($\Delta t = 120\,\text{s}$), 10 non-linear steps are made and the linear problem is iterated until an accuracy of $10^{-5}$ is reached, or 500 iterations are performed. The baseline simulation is run from January 1st, 1992 to December 31st, 2012. The analysis is based on daily averages of sea ice drift, ice thickness and concentration.

On October 17th, 1995 we branch off a simulation with an ice thickness distribution (Thorndike *et al.*, 1975) with 5 thickness categories separated by boundaries at $0.0\,\text{m}$, $0.64\,\text{m}$, $1.39\,\text{m}$, $2.47\,\text{m}$, and $4.57\,\text{m}$. In doing so, the initial sea-ice thickness and concentration of all thickness categories need to be determined from the 2-category simulation for each grid-cell. Most commonly this conversion is done by assigning all ice in one grid cell to the category with the same ice thickness. Then, some years of spin-up time are used to redistribute the ice into different categories (Ungermann & Losch, 2018). Due to the high resolution in our simulation a multiyear spin-up is not affordable. Therefore, we describe the ITD of each grid-cell by a log-normal distribution with a mode of 2/3 of the mean thickness. The mean thickness and concentration over all categories remain unchanged. With this initialization of the ITD-simulations, the spin-up of the ice thickness distribution is reduced to one year. We use the ice strength formulation of Rothrock (1975) and the smooth partition and redistribution functions of Lipscomb *et al.* (2007). The simulation with ITD is integrated from October 17th, 1995 to December 31st, 2012. In the following we refer to this simulation as **ITD** and to the baseline simulation as **noITD**. Both models provide data in the RGPS period of 1996 to 2008.

## Sampling and LKF extraction

The RGPS data set is originally provided as a Lagrangian data set that consists of trajectories of points that were followed throughout a winter season in consecutive SAR imagery. For each time record in this data set, vertices are constructed for four neighboring trajectories to approximate the deformation rates from the drift of a vertex by using line integrals. This results in

Lagrangian deformation rates. Then, the Lagrangian data are interpolated onto a regular Eulerian grid that is the basis of the RGPS LKF data set.

This Lagrangian nature of the RGPS data set confounds the comparison to Eulerian model output. Different approaches have been used to overcome this issue: (1) generate Lagrangian trajectories by on- or offline advection of artificial buoys in the model simulation that are initialized at the initial position of RGPS trajectories (Rampal *et al.*, 2016; Hutter *et al.*, 2018), (2) interpolate simulated drift speeds to the position of the RGPS vertices (Spreen *et al.*, 2016), or (3) just compare directly Eulerian gridded deformation rates with RGPS (Wang *et al.*, 2016; Bouchat & Tremblay, 2017). If one is interested in the accurate magnitude of the deformation rates and in particular in its temporal scaling, only the most sophisticated option (1) can be used as it takes the advection of ice into account and handles the boundary definition error (Lindsay & Stern, 2003) consistently for model and RGPS.

The LKF detection algorithm used here does not depend directly on the magnitude of deformation rate itself but on the local variations of the deformation rates (Hutter *et al.*, 2019). Therefore, the detection algorithm can be applied directly to the deformation rates on the output grid assuming it is a regular grid. Thus we avoid complicated sampling strategies that involve expensive post-processing of model output. The advection of ice is taken into account by the tracking algorithm.

Deformation rates are computed from daily mean velocity output following the spatial discretization of strain-rates as formulated in the model code (Losch *et al.*, 2010). We reduce the spatial resolution of the input fields of the detection algorithm by a factor of 3 to $6.75\,\mathrm{km}$ by taking only every third pixel into account to reduce computational costs. As deformation features in the simulations show a width of $\sim 5\,\mathrm{pixels}$ this can be done without missing features in the detection. We detect features every three days to agree with the temporal resolution of RGPS. The parameters used in the detection algorithm are the same as in Hutter *et al.* (2019, their Tab. 1), where all parameters marked with [b] are scaled to the reduced model resolution by multiplying with a factor of $12.5\,\mathrm{km}/6.75\,\mathrm{km} = 1.85$. The detected features are tracked with the tracking algorithm using the parameters of Hutter *et al.* (2019, their Tab. 2). The drift required for the tracking of LKFs is obtained by the integration of the mean daily velocities over a three day period.

### 4.2.4 Spatio-temporal scaling analysis

Sea-ice deformation is known to depend on spatial and temporal scales following a power-law (Weiss, 2013),

$$|\dot{\epsilon}(T,L)| \sim L^{\beta(T)}, \tag{4.1}$$

$$|\dot{\epsilon}(T,L)| \sim T^{\alpha(L)}, \tag{4.2}$$

where $|\dot{\epsilon}(T,L)|$ is the mean deformation rate for the temporal scale $T$ and the spatial scale $L$. These scaling properties have been used to compare the self-similarity of sea-ice deformation in satellite observations and various model simulations (Rampal *et al.*, 2016; Spreen *et al.*, 2016; Hutter *et al.*, 2018; Bouchat & Tremblay, 2017). Higher moments of the deformation rate also follow a power-law scaling (Marsan *et al.*, 2004; Weiss & Dansereau, 2017),

$$|\dot{\epsilon}(T,L)^q| \sim L^{\beta(q)}, \tag{4.3}$$

$$|\dot{\epsilon}(T,L)^q| \sim T^{\alpha(q)}, \tag{4.4}$$

with $q$ being the order of the moment. Here, the scaling exponents vary with the moment order and follow quadratic structure functions $\beta(q) = aq^2 + bq$ and $\alpha(q) = cq^2 + dq$ to show the multi-fractal intermittency and localization, that is, larger deformation events are more localized and intermittent that low deformation rates (Rampal *et al.*, 2019).

The spatio-temporal scaling analysis performed in this paper is based on the offline integration of trajectories from daily averaged velocity output of the model. Trajectories are initialized on the RGPS grid on November 1st of each year covered by RGPS (1996-2007). The artificial buoys are advected until mid-May of the following year and daily positions are recorded. Note that the trajectories agree with RGPS drift data in their initial position but not in their entire path. We use the initial position of the trajectories on the regular RGPS grid to define rectangular cells of 4 buoys to compute deformation rates. These cells are followed over the entire winter. The deformation rates at the finest (initial) scales of $L_0 = 10\,\mathrm{km}$ and $T_0 = 3\,\mathrm{days}$ are determined from the drift of the vertices using line integrals (Lindsay & Stern, 2003). In this computation, cells are removed that change their size by a factor of two or more.

The deformation rates for larger spatial and temporal scales are obtained by averaging the original deformation rates — a method referred to as coarse-graining (Marsan *et al.*, 2004). First, we average $n^*$ deformation rates in the temporal domain to obtain the deformation rates for $\dot{\epsilon}\,(T, L_0)$. The actual temporal scale of this average is determined by the number of valid deformation rates at initial scale $n \leq n^*$ with $T = nT_0 \leq n^*T_0$. Averages for which $n \leq n^*/2$, that is, less than half of the deformation rates in the interval, are available, are removed. Next, the deformation rates are averaged in space. In doing so, we average $m^* \times m^*$ temporal averages of deformation rates to $\dot{\epsilon}\,(T, L)$. The spatial scale $L$ of the average is determined by the square-root of the area that is covered by valid deformation rates where $L \leq m^*L_0$. All cells that are less then half filled $L < L_0/2$ are removed.

## 4.2.5 Irregular temporal sampling of RGPS

The RGPS drift data sets consists of a set of points that are followed in time in consecutive images of RADARSAT. Therefore, the temporal sampling of position updates depends on when the satellite passes over a particular area. The RADARSAT repeat cycle is 3 days during which it covers the Arctic Ocean. The repeat cycle is also the general temporal resolution of RGPS.

Each time an image is available in a region (smaller than the entire Arctic) with RGPS drifters, the drifter positions are updated. The time stamp of the record of all RGPS drifters within one image is the same, but the time stamp of the next (subsequent) image is slightly delayed by the time it takes the satellite to fly to this neighboring region. Note that in this way the positions of drifters that are on both images are updated twice within a time period much shorter than 3 days. The time difference within one over-fly, called a stream in RGPS data, is small compared to the time difference between those streams. This irregular time sampling complicates the computation of deformation rates using line integral approximations on polygons constructed of RGPS drifters, because all vertices (RGPS drifters) contained in the polygon need to have position records at the same time.

Comparing the deformation rates of RGPS data to model output leads to a second problem: we use trajectories initialized at RGPS positions and advected with daily mean model velocities as described in Sec. 4.2.4. The positions of these trajectories are saved in 3-day intervals, so that all deformation rates computed from model data cover a 3-day period and start and

end at the same time. The deformation rates computed from RGPS data, however, have varying start and beginning time and varying time intervals.

Hence, the RGPS deformation rates need to be converted to regular 3-day intervals to set-up a common framework for a comparison. Rampal *et al.* (2019) used simple nearest neighbor interpolation to do so and glosses over temporal details. For a more accurate conversion, we take the following processing steps for each stream: (1) we form rectangles from all RGPS drifters using their initial position. (2) For each rectangle, we check the time records of all vertices for time records that are shared by all four vertices with a tolerance of $\pm 3\,$h. (3) From these common time records we compute velocity gradients if the time between two common records is larger than $1.75\,$days and smaller than $7\,$days. (4) The computed velocity gradients are then averaged in the fixed 3-day intervals weighted by the time they overlap with the fixed 3-day interval. The set of 3-day grided deformation rates for each stream is merged into a composite for the Arctic. In a region where two streams overlap, we choose the data of the stream that has a larger temporal coverage and remove the data of the other stream.

## 4.3 Scaling in sea-ice deformation

The mean deformation rates in the RGPS data set and both simulations decrease with the increasing spatial scale (Fig. 4.1a). This decrease follows a power-law (Eq. 4.3) showing that the deformation is strongly localized. The ITD simulation shows higher deformation rates than the RGPS data across all spatial scales, whereas the noITD simulation underestimates deformation rates. The spatial scaling exponents of the ITD simulation agree very well with RGPS observations. The noITD simulation shows a slightly weaker localization of deformation rates than the RGPS data. The scaling exponent increases with the moment order following a quadratic structure function for all three data sets (Fig 4.1b). This shows that strong deformation events are more strongly localized than weak deformation events, which indicates multi-fractal spatial scaling of deformation rates. The structure functions have curvatures of $c = 0.14$ (RGPS) and $c = 0.15$ (both model simulations) consistent with previously published results ($c = 0.13 - 0.14$; Marsan *et al.*, 2004; Rampal *et al.*, 2016). The remarkable agreement of the curvature in RGPS data and model simulations implies that not only do the model
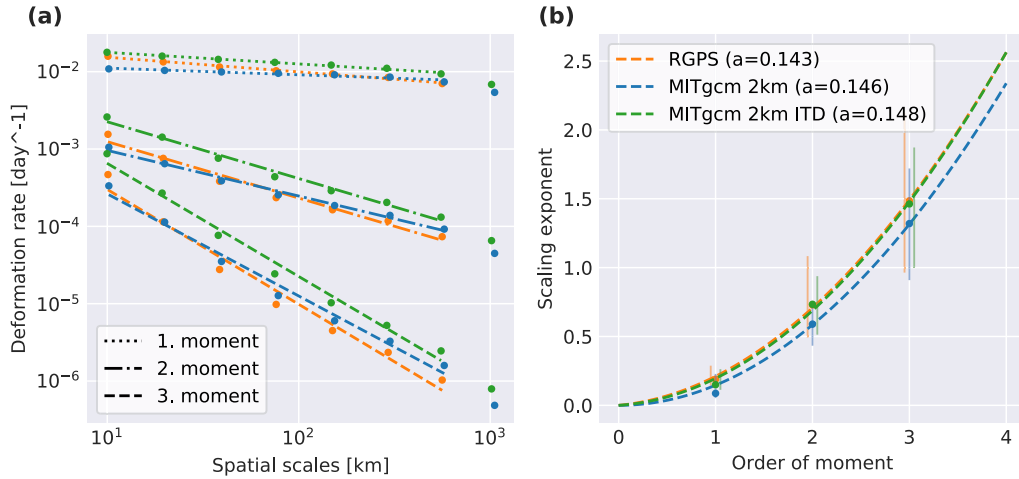
**Figure 4.1:** **(a)** The first three moments of sea-ice deformation rate as a function of the spatial scale for RGPS and both model simulations. **(b)** The spatial scaling exponents as a function of the moment order. A quadratic structure function $\beta(q) = aq^2 + bq$ is fitted (dashed lines). The curvature of the fit is given in the legend. The error bounds of the scaling exponents are determined by the minimum and maximum slope between successive points of the power-law fit.

simulations reproduce the spatial heterogeneity of deformation rates, but also the stronger localization of extreme deformation events.

The temporal scaling analysis (Fig. 4.2) shows that the sea-ice deformation is governed by the multi-fractal temporal scaling: (1) the moments of sea-ice deformation decrease with increasing temporal scale following the power-law of Eq. (4.4). (2) The temporal scaling exponents vary quadratically with the order of the moments. Again, the structure functions of the model simulations resemble the structure function found for RGPS data and the obtained curvatures $c = 0.13$ (ITD) and $c = 0.11$ (RGPS, noITD) agree with previous studies ($c = 0.12$, Weiss & Dansereau, 2017). Again, a positive curvature of the structure function implies that the high deformation events are more strongly localized in time than small deformation events.

The multi-fractal scaling properties of sea-ice deformation imply a space-time coupling for both the RGPS data and model simulations, that is, the degree of localization changes with temporal scale and the degree of intermittency changes with spatial scale (Fig. 4.3). We find that for model simulations the curvature of the structure function of the spatial scaling exponent decreases with increasing temporal scale at a rate similar to the RGPS data (Fig. 4.3a). Note, that this was not possible with the MEB-rheology (Ram-
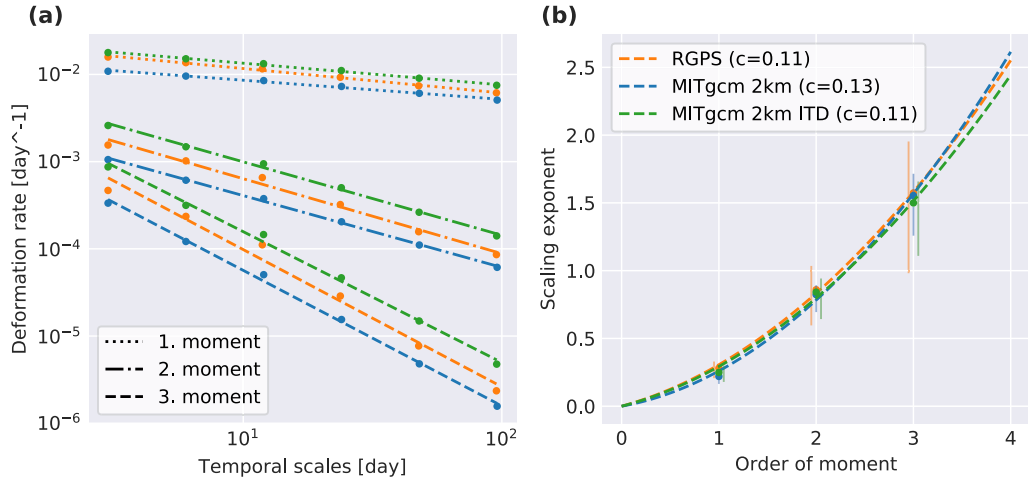
**Figure 4.2: (a)** The first three moments of sea-ice deformation rate as a function of the temporal scale for RGPS and both model simulations. **(b)** The temporal scaling exponents as a function of the moment order. A quadratic structure function $\alpha(q) = cq^2 + dq$ is fitted (dashed lines). The curvature of the fit is given in the legend. The error bounds of the scaling exponents are determined by the minimum and maximum slope between successive points of the power-law fit.

pal *et al.*, 2019). The curvature of the structure function of the temporal scaling exponent also decreases with increasing spatial scale (Fig. 4.3b). The curvature of the structure function of the temporal scaling exponent follows a power-law (Fig. 4.3b) as suggested by Rampal *et al.* (2019), but for the spatial scaling this fit is not as good (Fig. 4.3a).

Comparing the spatio-temporal scaling of both model simulations, we find that deformation rates as well as spatial and temporal scaling exponents for the first moment of scaling deformation are higher in the ITD simulation compared to the noITD simulation. This supports the hypothesis of Hutter *et al.* (2018) that the ice strength formulation in the ITD run intensifies the feedback cycle of ice strength and deformation. This intensification in the ITD simulation is caused by the ice strength being more dependent on the concentration of the thinnest ice class. In the case of divergence, newly formed ice in open water fills this thinnest class and reduces the ice strength.

In summary, the spatio-temporal scaling analysis shows that both model simulations reproduce the observed multi-fractal heterogeneity and intermittency of sea-ice deformation (Marsan *et al.*, 2004; Rampal *et al.*, 2008; Weiss & Dansereau, 2017; Oikkonen *et al.*, 2017) equally well as more sophisticated models that were specifically designed to generate these characteristics
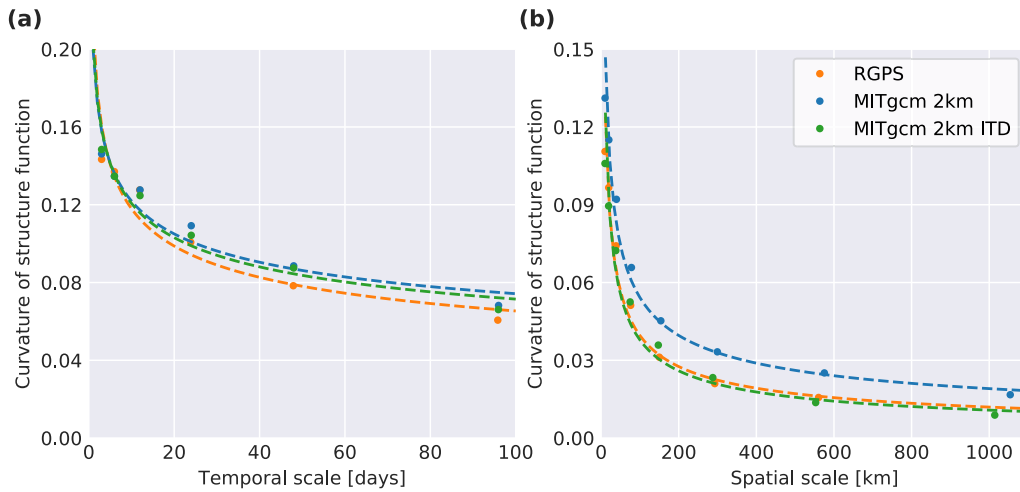
**Figure 4.3:** Spatio-temporal coupling of multi-fractal scaling: **(a)** The curvature of the structure function of the spatial scaling exponent as a function of temporal scale for RGPS data and both model simulations. **(b)** The curvature of the structure function of the temporal scaling exponent as a function of spatial scale. The dashed lines provide power-law fits to the decay of the curvature.

(Girard *et al.*, 2011).

## 4.4  LKF statistics

We split the analysis of the detected and tracked LKFs into three different parts: (1) the Pan-Arctic distribution of LKFs that describes the overall number of LKFs, the density and orientation of LKFs, (2) spatial properties of LKFs, that is, the length and curvature of LKFs as well as the angle at which they intersect, and (3) the temporal evolution of LKFs as described by their persistence and their growth rates. Each metric is presented and discussed in a separate subsection for RGPS data and both model simulations. The overall quality of LKFs in the simulations and the link between LKF statistics and scaling analysis is discussed in the separate Section 4.5.

This comparison includes some metrics that are sensitive to the coverage of the LKF data set. While the coverage of the model is Pan-Arctic and constant in time, the coverage of the RGPS data varies with time. We mask the LKFs of the model simulations with the RGPS coverage of the corresponding record. As some LKFs are removed in part or entirely, this filtering affects also the tracking of the features. The tracking algorithm is, therefore, run once again on the filtered features. We label the masked

89

version of model LKFs in the legend of the corresponding plots.

### 4.4.1 Pan-Arctic distribution of LKFs

In the following section we test whether the model simulations reproduce (1) the number of features for different years and seasons, (2) the regional distribution of deformation features, and (3) the mean orientation compared to the RGPS LKF data set.

**Number of LKFs**

The first and most obvious metric for testing whether a model simulates LKFs in agreement with observations is the number of features detected in model simulations and observations. This metric was used for the optimization of solver parameters (Koldunov *et al.*, 2019) and provides some valuable first insights. The number of detected features in RGPS data and both model simulations are given in Fig. 4.4. We, here, use the version of the LKF data set for both model simulations that has been filtered by the RGPS coverage and normalize the number of LKFs by the number of RGPS observations to account for the varying RGPS coverage.

The RGPS LKF data set shows a decrease of deformation features for the period from 1996 to 2004 (from 0.015 to 0.0125 LKFs per RGPS observation). In the winter of 2004/2005 the number of features increases again to 0.0135 and levels off. There is no significant seasonal variability in feature numbers for the RGPS data (Fig. 4.4b). The cumulative length of all LKFs, defined as the sum of all LKF lengths in one record, shows seasonal variations (Fig. 4.4d). The cumulative length decreases as the ice advances and reaches a minimum in mid March implying that in this season the area is smaller where atmosphere-ice-ocean interaction processes take place. This difference in the seasonal cycle shows that in the freezing season (November to January) LKFs tend to be larger than in the remaining part of the year.

The number of detected LKFs in the ITD simulation agrees on average very well with RGPS except for the last two winters (Fig. 4.4a). The interanual variability in LKF numbers, however, is larger by a factor of 2 compared to the RGPS data (shaded standard deviation in Fig. 4.4b). The number of features is higher than for the RGPS data in the early freezing period in November and after mid April. Starting in late spring, the ice cover seems to
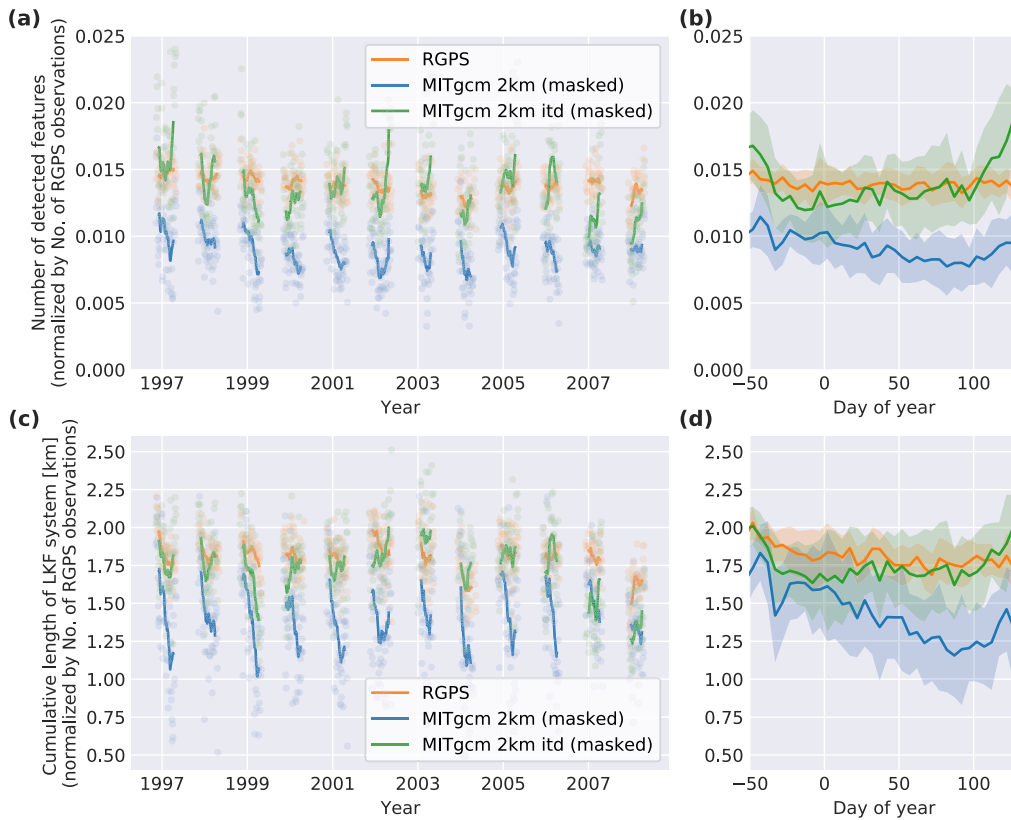
**Figure 4.4:** **(a)** The number of LKFs detected for entire observing period (1996 to 2008). The lines are running means with a window size of 17 days of the individual daily numbers represented by the light-colored dots. **(b)** Seasonality of the number of LKFs. The lines are running means with a window size of 5 days. The shaded areas show the standard deviation of the individual years. **(c)** Same as **(a)** but showing the cumulative length of the system of all LKFs, defined as the sum of all LKF lengths in one record. **(d)** The seasonal cycle of the cumulative length of the LKF system. For the analysis presented in this Figure the LKF data sets of both simulations are filtered for RGPS coverage.

be too weak in the simulation so that there are more LKFs and a generally too large LKF network.

In the noITD-simulation, there are $\sim 30\,\%$ fewer detected features than for the RGPS data set and the cumulative LKF length is shorter by $\sim 20\,\%$. This simulation reproduces the weak seasonal cycle of the numbers of LKFs in the RGPS data, but numbers are generally too low and then they slightly increase in April (Fig. 4.4b and d). For the cumulative LKF length, however, the magnitude of seasonal cycle is twice as strong for the model than for the RGPS data (Fig. 4.4c), which shows that the average LKF length in the simulation is more variable. The noITD simulations shows a higher average

LKF length compared to RGPS data before March and a lower average LKF length afterwards.

**LKF density**

The number of LKFs only provides insight about the temporal development of LKFs, but the LKF densities (i.e. their relative frequency of occurrence) show how the simulated LKFs vary in space compared to the RGPS data. In the RGPS data (see also Hutter *et al.*, 2019), we find the highest densities along the shorelines of islands such as the New Siberian Islands and Wrangel Island (Fig. 4.5a; for geographical reference see Fig. 4.5b). The highest densities within the ice pack are found in the Beaufort Sea. Low densities stand out in the fast-ice region in the East Siberian Sea with a sharp fast-ice edge. Similar distributions were found for lead densities derived from MODIS thermal-infrared imagery (Willmes & Heinemann, 2016) and CryoSat-2 data (Wernecke & Kaleschke, 2015).

In both simulations, the regions of high LKF densities are similar, but the ITD simulations has generally higher densities. Here, LKFs concentrate along small islands and coastlines as in the RGPS data. Besides Wrangel Island and the New Siberian Islands, Severmaya Zemlya and Franz Josef Land are preferred starting points of LKFs. The highest densities along the coastlines are found at Barrow (Alaska) and at North-Eastern tip of Greenland, consistent with remote sensing data estimates (Willmes & Heinemann, 2016). These high densities along the coast of Alaska are not resolved in the RGPS data set, because the detection algorithm cannot identify LKFs that are located at the edge of the RGPS coverage. The general overestimation of coastal deformation in the model simulations combined with an underestimation in the pack-ice compared to RGPS data suggests stress propagation to the coast in the model due to a lack of inhomogeneities in the pack-ice that serve as seeding points for failure.

In both simulation we observe distinct fast-ice regions with low LKF densities only in the Eastern Laptev Sea, but not in the East-Siberian Sea. Further, the simulated LKFs do not accumulate at the Hanna Shoal as the RGPS LKF densities. In this shallow region, keels of pressure ridge frequently ground which initiates the formation of leads (Mahoney *et al.*, 2012). Both the missing landfast ice in the East-Siberian Sea and the missing effect of grounded ice may be improved by implementing a grounding scheme
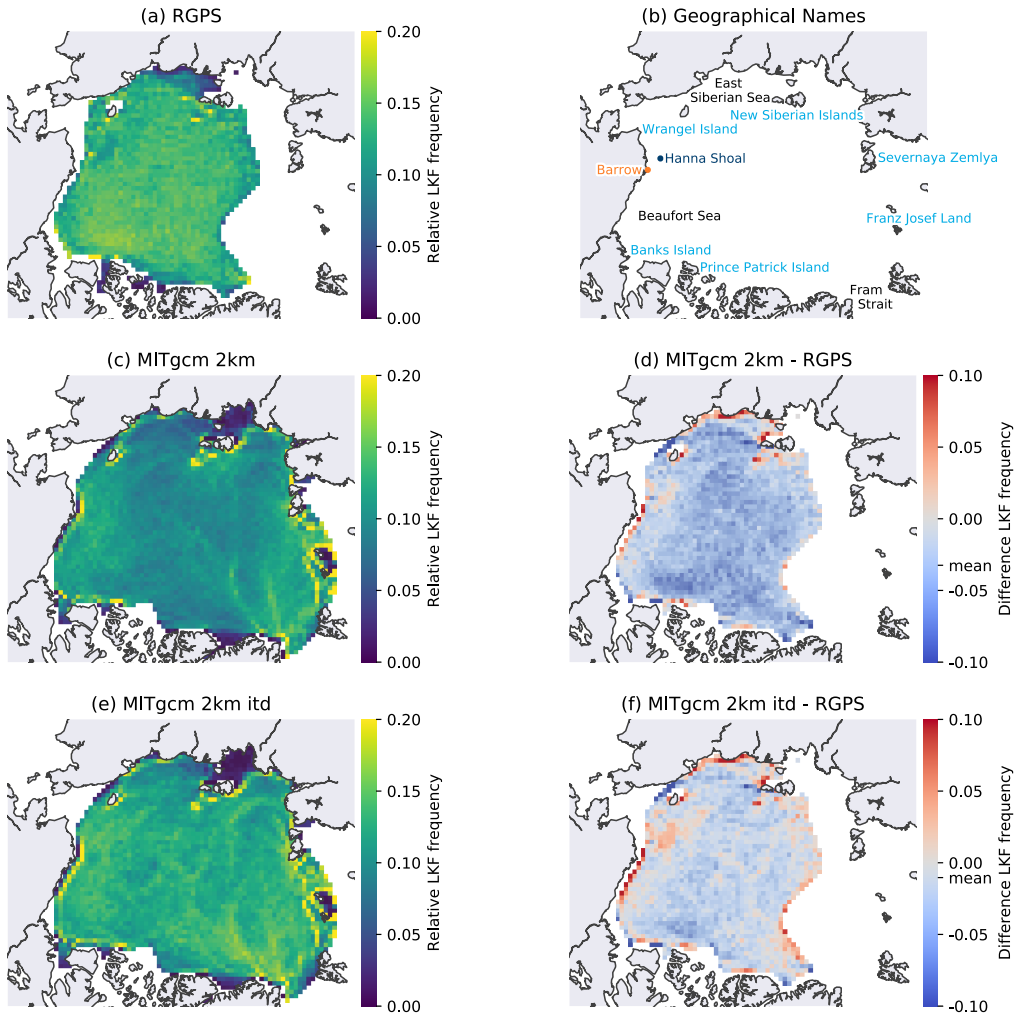
**Figure 4.5: (a,c,e)** The density of LKFs in the RGPS data set and the two model simulations for the winters between 1996 and 2008. The absolute frequency of LKF pixels in a cell is normalized by the number of deformation observations. Only cells with more than 500 deformation observations are shown. **(d,f)** The difference in density between both model simulations and RGPS. **(b)** The geographical locations that are referenced in the text.

(Lemieux *et al.*, 2015).

For the RGPS data, a band of enhanced LKF activity connecting Hanna Shoal and Wrangel Island (Fig. 4.5) is consistent with results based on Advanced Very High Resolution Radiometer (AVHRR) (Mahoney *et al.*, 2012). In the RGPS data, we observe lower LKF densities north of this band. Neither the band nor the region of low LKF densities can be found in either simulations. We speculate that in the model there are no stress locators in the form of grounded ice, which leads to a spatially broader distribution of

failure and LKFs.

The elevated LKF densities in the Beaufort Sea in the RGPS data are another prominent feature within the pack ice. These have been attributed to the shear induced by the Beaufort Gyre circulation (Willmes & Heinemann, 2016). We do not observe the increased probability in LKF formation in either simulations, which may suggest too weak Beaufort Gyre circulation or issues with the simple ice-ocean drag parameterization that does not take into account keels and sails in deformed multi-year ice (Tsamados *et al.*, 2014; Castellani *et al.*, 2018).

**LKF orientation**

A preferred LKF orientation indicates frequently occurring forcing conditions. We compute the orientation of LKFs clustered in $200\,\text{km} \times 200\,\text{km}$ boxes in the Arctic. Within each box, the orientation of the part of each LKF that overlaps with the box is determined. From these orientations we compute the mean orientation (Fig. 4.6a-c) following Bröhan & Kaleschke (2014). In addition, we determine the modes of the orientation distribution within each box (Fig. 4.6d-f), as the mean orientation is misleading for multi-modal distributions. We find the modes of multi-modal distributions of LKF orientations by determining local maxima in the Probablitiy Density Function (PDF). First, we estimate the PDF of the distribution using a Kernel Density Estimation (KDE) with von-Mises kernels that can be seen as the analogue of the Gaussian distribution on a circular domain (Borradaile, 2003). The modes of the distribution are given by the local maxima of the PDF estimated by the KDE. To test whether the obtained orientation distributions are significantly different from a random distribution, we draw 10,000 random orientation samples of the same size and perform a $\chi^2$-test (Bröhan & Kaleschke, 2014). We mark points where the mean probability of the $\chi^2$-tests is less than $1\,\%$ as statistically significant. We take into account only LKFs with an average total deformation rate of $0.5\,\text{day}^{-1}$ to agree with visually identified LKFs (Kwok, 2001).

Both the mean orientation and the first mode of orientation are generally parallel to the coastline (Fig. 4.6a and d). The LKFs orientated in this direction are most likely flaw leads between the fast ice along the coast and the mobile pack ice. The model simulations reproduce this behavior along all coastlines. The parallel orientation to coastlines is consistent with lead ori-
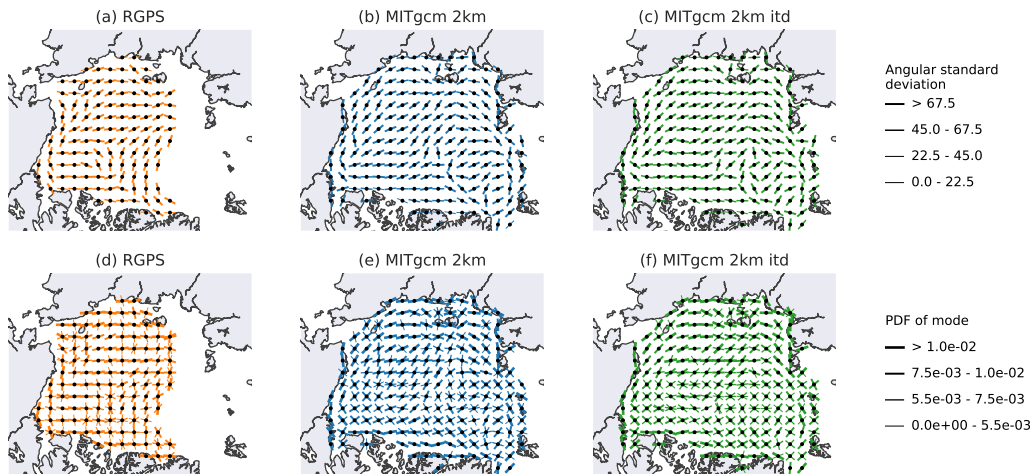
**Figure 4.6: (a,b,c)** Mean orientation of LKFs for RGPS and two model simulations. We follow the definition of mean and standard deviations for circular data from Bröhan & Kaleschke (2014) for lead orientations. The line width indicates the standard deviation of the distibrution within the cell. Orientation distributions that are statistically significantly different from a random distribution are marked by a black dot. Only cells that contain more than 500 LKFs are shown. **(d,e,f)** Modal orientation of LKFs for RGPS and two model simulations. The three largest modes of the distribution of orientation are plotted for cells with including more than 500 LKFs. The probability (PDF) of each mode is shown by the line length, where a PDF value of $5.5 \cdot 10^{-3}$ corresponds to the mean PDF value of a random distribution.

entations reported earlier (Miles & Barry, 1998; Bröhan & Kaleschke, 2014).

In the east Siberian Sea the mean LKF orientation is from east to west in the RGPS data as well as in both model simulations. This is also the orientation of the local fast-ice edge. The mean orientation shifts towards the north-south direction in the Beaufort Sea, again for the observations and both simulations. This general pattern of LKF orientation is consistent with the orientations derived from visually detected leads in thermal- and visible-band imagery of the years 1979–1985 (Miles & Barry, 1998). Interestingly, there are substantial differences to more recent results with predominantly east-west orientations in the Beaufort Sea (Bröhan & Kaleschke, 2014). These differences may appear because Bröhan & Kaleschke (2014) used data from a different time period (years 2002–2011) or because they used a more sophisticated statistical method (Hough transform). We note that although RGPS data and simulations agree in the mean LKF orientation in these regions, the model shows a spread in the modal values, which points towards too

95

large LKF intersection angles that lead to two peaks in the distribution of orientations.

In the Central Arctic, the mean orientation of LKFs in the RGPS data suggests a circular deformation pattern that originates in North-East Greenland, circles the North Pole and heads towards Severnaya Zemlya. The pattern is reminiscent of a basin-scale ice arch formed by the main sea ice export pathway through the Fram Strait. In the modal representation of LKF orientations, this arch is barely visible in the model simulations. In the Fram Strait, we find modes parallel and perpendicular to the outflow direction, indicating the build-up of flow blockages similar to ice arches together with shearing zones between the exported sea ice and the fast-ice along the coast of Greenland.

### 4.4.2 Spatial LKF properties

**LKF length**

LKFs in the Arctic have length scales from a few meters up to the basin-scale ($1000\,\mathrm{km}$). Given that automated lead detection is challenging and hand-picked lead data sets have a limited sampling size, the first quantitative estimates of LKF length have been published only very recently (Linow & Dierking, 2017; Hutter *et al.*, 2019). From 10 RGPS records Linow & Dierking (2017) inferred an exponential distribution of LKF lengths. Length measurements of lead skeletons, again from a small sample-size, were also distributed exponentially (Van Dyne *et al.*, 1998). The distribution of LKF lengths from the entire RGPS data set contains more extreme values (Hutter *et al.*, 2019) and is described by a stretched-exponential distribution: $p(x) = Cx^{\beta-1}\mathrm{e}^{-\lambda x^{\beta}}$ with $C = \beta\lambda\mathrm{e}^{\lambda x_{\min}^{\beta}}$ (Clauset *et al.*, 2009). Stretched-exponential distributions belong to the family of heavy-tailed distribution, but in contrast to the power-law distribution have a natural upper limit scale (Laherrère & Sornette, 1998). Here, the upper limit scale is the finite size of the Arctic Ocean.

We determine the PDF of LKF lengths from RGPS data and both model simulations (Fig. 4.7a). We fit a stretched exponential distribution to all data sets using Maximum Likelihood Estimators and perform a goodness-of-fit test (Hutter *et al.*, 2019). We find that all distributions are accurately described by stretched exponentials (RGPS: $\lambda = 1.69 \cdot 10^{-2}, \beta = 0.719$, noITD: $\lambda =$
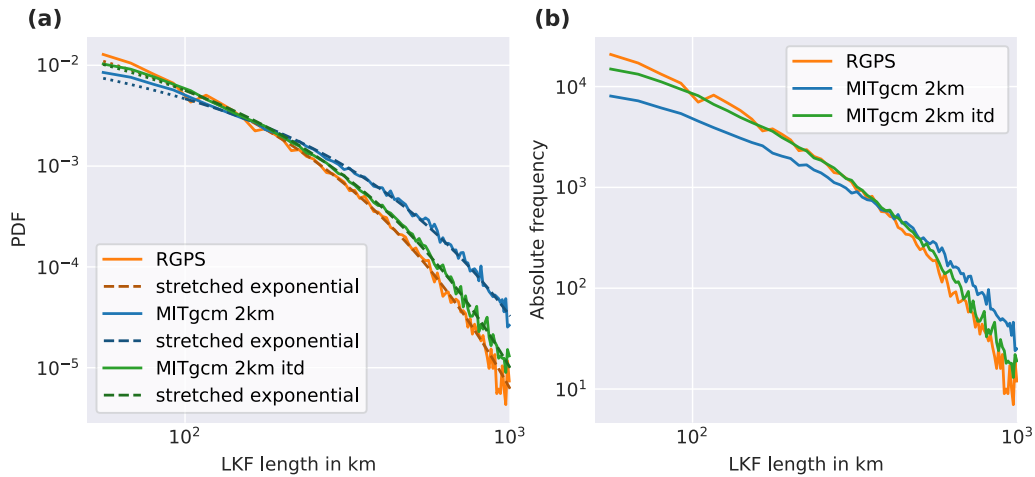
**Figure 4.7:** **(a)** PDF of LKF lengths for RGPS data and both simulations along with fits to stretched exponential distributions. **(b)** Absolute frequencies of LKF lengths in RGPS data and both simulations. For the analysis presented in this Figure the LKF data sets of both simulations are filtered for RGPS coverage.

$0.90 \cdot 10^{-2}, \beta = 0.761$, and ITD: $\lambda = 1.38 \cdot 10^{-2}, \beta = 0.741$). The PDF of the ITD simulation agrees remarkably well with the RGPS PDF; only for LKFs longer than 150 km, the probabilities are slightly higher. In the noITD simulation large LKFs ($> 300$ km) have a higher probability than in the RGPS data or in the ITD simulation. From the absolute frequencies of LKF lengths (Fig. 4.7b), it becomes clear that these high values in the (normalized) PDF are to a large extent a consequence of too few small LKFs. From the deficit in small-scale deformation features in the noITD simulation one may infer that there are too few inhomogeneities in the ice cover that can initiate failure. The ITD sub-grid model allows for more small-scale variations in the ice thickness distribution that are reflected in the ice strength and in turn lead to stronger localized deformation.

## LKF curvature

As their name implies, Linear Kinematic Features are mostly linear with only little curvature (Kwok, 2001). Linow & Dierking (2017) introduced the dependence of the distance between both endpoints on the LKF length as a metric for the curvature of an LKF. This ratio is 1 for perfectly linear features and 0 for circular ones. We apply this metric to all LKFs detected in the RGPS data and both simulations and plot the distance between LKF endpoints against the LKF length (Fig. 4.8). For perfectly linear LKFs, all
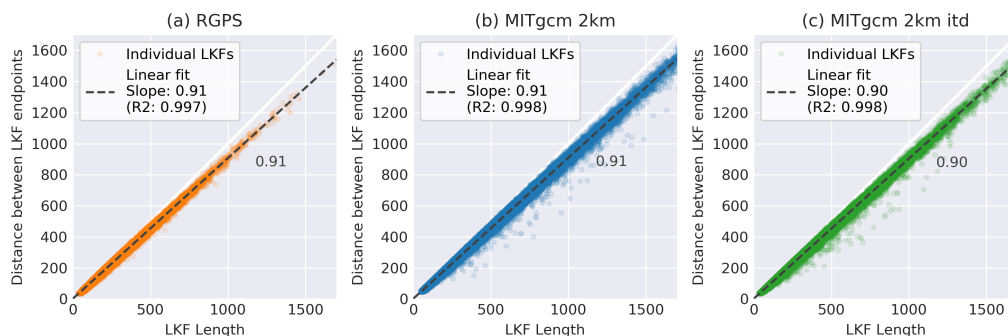
**Figure 4.8:** The distance between the endpoints of an LKF plotted over its length. We find that all observations fit a linear line. The slope of the fitted linear relationship is given next to the fitted line.

points converge to a line with a slope of 1 (the diagonal of the plot). We find that all LKFs clearly fall on a line with slopes of 0.91 (RGPS and noITD) and 0.90 (ITD) for all length scales from up to 1700 km. Thus, the shape of the LKFs does not change with spatial scale, which agrees very well with the self-similar properties of sea-ice shown for the size of ice floes (Stern *et al.*, 2018) and deformation features (Weiss, 2003; Marsan *et al.*, 2004; Wernecke & Kaleschke, 2015). Both simulations reproduce the curvature of the features itself and its scale invariance. We, here, note that this fairly simple metric does not allow further inferences about the shape of LKFs, but it has the advantage that it can be applied in a straightforward manner to a large variety of LKFs.

**LKF intersection angles**

The intersection angle of LKFs is strongly related to the material properties, more precisely to the yield curve of the rheology (Erlingsson, 1988; Wang, 2007), but only intersection angles of conjugate faults, where intersecting LKFs form instantaneously under the same forcing conditions, provide direct information about the yield curve. Therefore, we limit the analysis of intersection angles to pairs of LKFs that form in the same time record. In addition, we require the length of both LKFs to be larger than 125 km to exclude the effect of a preferred direction along the pixels of the image.

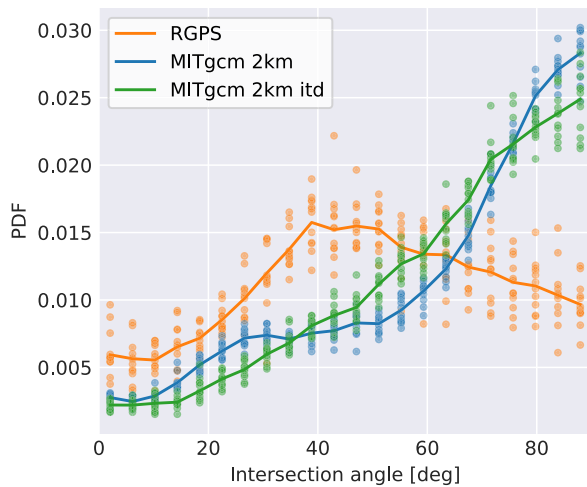The PDF of intersection angles for RGPS data peaks around 40°–50°

**Figure 4.9:** The PDF of intersection angles of LKFs in RGPS data and both simulations. The analysis is limited to pairs of LKFs that formed in the same time record and have a length larger 125 km. Individual years are plotted as colored points and the multi-year mean is given as a solid line.

(Fig. 4.9). This peak agrees with typical intersection angles of 30°–50° inferred from satellite imagery (Walter & Overland, 1993; Schulson & Hibler, 2004; Wang, 2007). We find the lowest probabilities for angels smaller than 20°. Angles larger than 50° occur more often than angles smaller than 40°. The distributions of intersection angels in both model simulations are very different from the RGPS data and peak at 90°. Intersection angles smaller than 60° are less frequent in the model simulations than in the RGPS data. The differences between both simulations are small.

According to theoretical considerations, the intersection angle is determined by the slope of yield curve (Pritchard, 1988; Wang, 2007). As both simulations use the same elliptical yield curve with a normal flow-rule (Hibler, 1979) similar intersection angles of LKFs are expected. We attribute the small differences in Fig. 4.9 to sea ice fields with a different amount of LKFs. Ringeisen *et al.* (2019) derived for idealized compression experiments that it is impossible to obtain intersection angels smaller than 60° with an elliptical yield curve. This explains the deficit of small intersection angles in our simulations.

### 4.4.3 Temporal evolution of LKFs

The temporal evolution of LKFs has not been studied very much. In-situ field observations of individual leads breaking individual floes (e.g. Dempsey *et al.*, 2012) suffer from space and time limitations. Qualitative evaluations of the persistence of lead patterns on the order of a month (Kwok, 2001) did not focus on individual leads to deduce these temporal characteristics
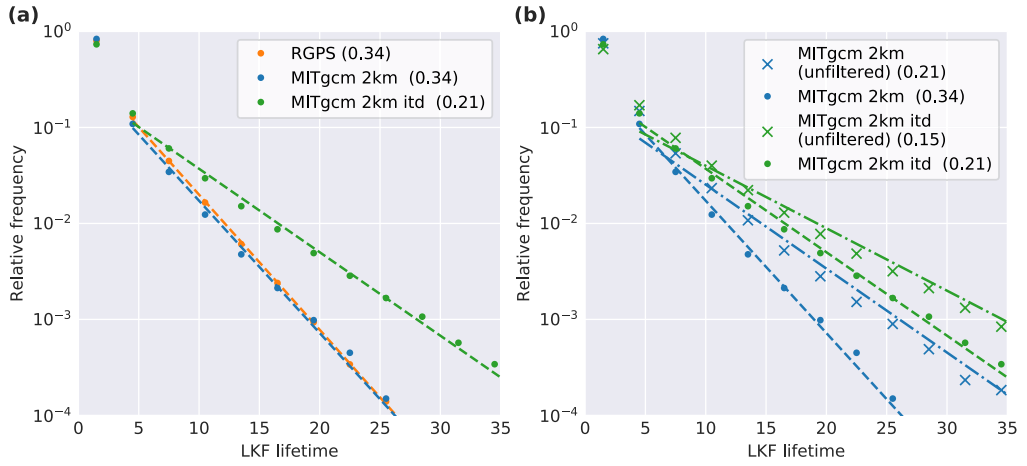
**Figure 4.10:** **(a)** The relative frequency of lifetime of LKFs in RGPS data and both simulations. The LKFs detected and tracked in the simulations are reduced to the RGPS coverage. The dashed line are fits to exponential tails. The rate of the exponential tail in day$^{-1}$ is given in the legend. **(b)** Lifetime of modeled LKFs reduced to the RGPS coverage (dots and dashed lines) and unfiltered (crosses and dash-dotted lines).

of LKFs and are necessarily inaccurate. Hutter *et al.* (2019) combined the large coverage of the RGPS data with a tracking algorithm to provide first qualitative estimates of LKF lifetimes. Here, we use the same method to study the persistence and the growth rates of LKFs.

## LKF persistence

We determine the lifetime of an LKF by counting how many times we track a feature. The lifetime estimates are binned into 3-day intervals, that is, the temporal resolution of the deformation data. We compute the lifetime of LKFs in RGPS data and in both simulations. For the simulations we provide two calculations each: one after reducing the simulation data to the RGPS coverage (Fig. 4.10a) and one for the full data sets (Fig. 4.10b). All lifetime distributions have an exponential tail. For the comparison with LKF lifetimes in the RGPS data we use the reduced versions of the model simulations (Fig. 4.10a). The lifetime distribution of the noITD simulation and the RGPS data have the same rate of the exponent tail of $0.34\,\text{day}^{-1}$. The ITD simulations overestimates the lifetime of LKFs with an exponential tail decaying with the rate of $0.21\,\text{day}^{-1}$.

The long LKF lifetimes in the ITD simulation can be caused either by too

homogeneous forcing fields or a too strong memory of past deformation, both of which favor continuous deformation of ice. Given the high temporal and spatial resolution of the atmospheric forcing data, too homogeneous forcing fields are unlikely to be the only cause. In the ITD simulation, deformation events imprint on the ice thickness distribution of a grid cell, which has an effect on the ice strength and hence leads to fast feedbacks on the deformation itself. In this sense, these changes in the ice thickness distribution can be regarded as a memory in the ice. Interestingly, this extra memory with the ice strength of Rothrock (1975) improves the agreement with the number of LKFs (Sec. 4.4.1) and the LKF density (Sec. 4.4.1) in the RGPS data set, but reduces the agreement with the RGPS data set in terms of LKF lifetimes. This suggests to improve the sea-ice model by decoupling the ice memory in the model from the ice thickness distribution.

The varying spatial coverage of the RGPS data introduces an unknown bias in LKF lifetimes. With our simulations we can estimate this bias by comparing the lifetimes of filtered LKFs to unfiltered LKFs (Fig. 4.10b). The difference for the noITD simulation, which agrees almost perfectly with RGPS data when masked by RGPS coverage (Fig. 4.10a), suggests that the amount of long lifetimes is reduced by the varying coverage with the rate of the exponential tail decreasing to $0.21\,\mathrm{day}^{-1}$, which corresponds to an increase in mean lifetime of $\sim 50\,\%$. For the ITD simulation the effect is similar.

**LKF growth rates**

Failure propagates quickly through the sea ice cover. This propagation can be modified or even stopped by changing forcing conditions. The growth rates of persistent LKFs provide information about these processes. We define the growth rate as the change in length of an LKF divided by the time between two records. In detail, we compute the area where both LKFs of a tracked pair overlap following the definition of overlap from Hutter *et al.* (2019) to determine how much of the change in length is attributed to growth and shrinking. This overlapping area is the part of the LKF that is seen in both time records. All parts of the LKF from the first time record that do not lie in the overlapping area are parts of the LKF that become inactive in the next time record. We associate the shrinking rate to these changes. Analogously, the LKF grows by the parts of the LKF in the second time record that
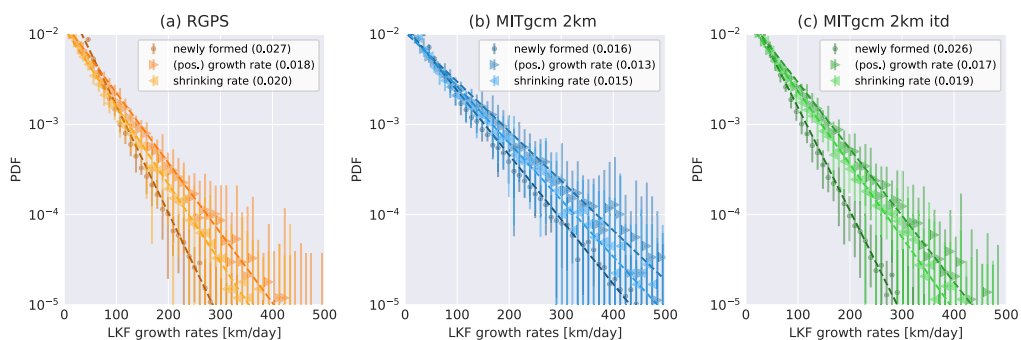
**Figure 4.11:** Mean (symbols) and standard deviation (vertical bars) of the growth rates of LKFs in RGPS data and both simulations. We differentiate between the growth rate, the shrinking rate, and the growth rate of newly formed LKFs. The dashed lines are fits to exponential tails, the rate parameter of which is given in the legend. For the analysis presented in this Figure the LKF data sets of both simulations are filtered for RGPS coverage.

lie outside of the overlapping area. These changes are associated with the (positive) growth rate. For completeness we also compute the growth rates of newly formed LKFs as their initial length divided by the temporal resolution.

All three growth rates follow an exponential distribution for the RGPS data and both model simulations (Fig. 4.11). Positive growth has the largest growth rates and the slowest decay of the exponential tail. The growth rate distributions of newly formed LKFs have the steepest exponential tails, but a higher probability of small growth rates ($< 50 \, \mathrm{km/day}$). This implies that it is more likely for an existing LKF to grow longer than for a new one to form. From a physical point of view, this is plausible because an existing LKF is a weakness in the ice, where, with constant forcing, stress can accumulate which facilitates further deformation. Both model simulation contain this effect.

The shrinking rates of persistent LKFs are smaller than their growth rates and larger than the growth rate of newly formed LKFs. The physical interpretation is that the fracture of ice acts on much smaller time scales than the healing of the ice cover. Therefore, breaking the ice and opening a lead takes less time than closing the lead by refreezing or convergent ice motion.

Both mechanisms — higher growth rates of persistent LKFs and slower closing of LKFs — are present in RGPS data and both model simulations. However, only the ITD simulation reproduces the higher rate parameters of

the exponential tails of RGPS observations. The tails for the noITD simulation decay more slowly for all three growth rate distributions. We attribute these differences to two effects: (1) the feedback between deformation and thickness that accelerates the formation of LKFs is slower without the ITD due to the different strength formulation. Therefore, higher stress builds up before plastic deformation takes place, and consequently larger LKFs are formed. (2) The low LKF density in the noITD simulation leaves enough space for LKFs to grow larger. There are two plausible ways of stopping an LKF from growing: either the stress is too small for further growth, or the LKF intersects another LKF. Thus, higher LKF densities lead to lower growth rates.

The low temporal resolution of 3 days cannot resolve true growing or shrinking rates of the LKFs, because the formation or destruction of a deformation features may take place on much shorter time scales. Therefore, the growth rates computed here cannot be compared to fracture speeds of sea ice determined from acoustical measurements. These fracture speeds range from 100 to 1100 m/s (Stamoulis & Dyer, 2000) and can be regarded as an upper limit of the LKF growth rates. In-situ measurements of lead propagation times can also be used as an upper limit: Dempsey *et al.* (2012) recorded a time of 10 s to break a 80 m ice floe which corresponds to a fracture speed of $\sim 690$ km/day. A higher temporal sampling rate is needed to directly compare our LKF growth rates with fracture speeds, which could be achieved by a higher output frequency for the model but is not possible for satellite observations.

## 4.5   Discussion

In this section we discuss how the new feature-based evaluation of LKF statistics is linked to the scaling analysis and what insights can be gained from LKF statistics for further model development.

Both simulations with and without ice thickness distribution (ITD) model agree remarkably well with satellite observations with respect to the representation of LKFs and spatio-temporal scaling analysis of sea ice deformation. We find that the simulated sea-ice deformation reproduces the multi-fractality in both spatial and temporal scaling, as well as the spatio-temporal coupling of multi-fractal characteristics, which remained a challenge even for

103

simulations with the MEB-rheology (Rampal *et al.*, 2019). Hence, our simulated sea ice deformation is characterized by strong heterogeneity and intermittency. Our present analysis is the most extensive scaling analysis so far for simulations with the VP-rheology and completes a set of previous scaling analyses (Bouchat & Tremblay, 2017; Spreen *et al.*, 2016; Hutter *et al.*, 2018) that show that previous findings about VP-simulations not being able to reproduce observed scaling properties at coarse grid resolution (Girard *et al.*, 2009) cannot be generalized (especially not to high grid-resolution simulations). For mean sea-ice deformation (first order moment $q = 1$) the simulation with an ITD leads to scaling exponents closer to the ones retrieved from RGPS, that is, sea-ice deformation is more strongly localized in space and time compared to the simulation without an ITD. We attribute this result to the ice strength parameterization of Rothrock (1975) in the ITD run that favors a fast evolution of plastic deformation.

Consistent with the scaling analysis in Section 4.3, we find that the ITD simulation has a larger number of LKFs compared to the noITD simulation. In general, the LKFs in the ITD simulation agree better with RGPS data in terms of the LKF statistics. The LKF lifetime is the only exception. We note that both simulations reproduce all observed characteristics: heavy-tailed distribution of LKF lengths, exponential tails in the distribution of LKF lifetimes and growth rates, and scale invariance of the LKF curvature. The distribution of intersection angles, however, is not reproduced in either simulations.

By combining the scaling analysis and the feature-based evaluation, we test which inferences from the scaling properties can be made about the representation of LKFs. We discuss in the following how the results of both analyses are linked in our special case, but stress that one analysis cannot replace the other. Nevertheless, their combined use may provide new insights from previous scaling studies.

The largest difference in LKFs between the simulations is that the noITD simulation produces considerably fewer LKFs compared to the ITD simulation. In Sec. 4.4.2, we discussed how this overall underestimation influences LKF properties such as LKF length and growth rates. In addition, deformation fields that include fewer features of localized deformation obviously will be smoother in both space and time. We attribute the lower scaling exponents for the noITD simulation largely to the lower numbers of LKFs. The multi-fractal spatial scaling for both simulations is consistent with the

heavy-tailed distribution of LKF lengths and the scale invariance in LKF shapes that suggest self-similar deformation patterns.

The difference in temporal scaling exponents also seems to be largely caused by the difference in LKF numbers because the noITD simulation reproduces the distribution of LKF lifetimes remarkably well (Fig. 4.10a) in spite of a lower temporal scaling exponent (Fig. 4.2). In contrast, the rate parameter of the LKF lifetime distribution in the ITD simulation is too low (Fig. 4.10) despite the better temporal scaling exponent. The absolute number of short-lived LKFs in the ITD simulation, however, is higher and thereby closer to estimates from RGPS data just because of the higher number of LKFs. In this case, linking the results of the temporal scaling analysis to the representation of LKF lifetimes as attempted in Hutter *et al.* (2018) appears to be incorrect.

With the LKF statistics, we identified some issues in the simulated deformation fields that could be addressed by specific parameterizations. A general theme in the discussion of LKF characteristics is the low LKF density in the simulations, which we attribute to too few inhomogeneities in the ice that can act as a starting point for fracture. With an ITD, the number and density of LKFs increase significantly. In the ITD simulation shear and divergence have a strong impact on the thin thickness classes which immediately feeds back into the ice strength facilitating further deformation. Therefore, inhomogeneities introduced by deformation in the thickness fields are much stronger compared to the standard VP simulation.

Simulated LKF densities in the pack ice away from the coast are too low compared to RGPS data and the distribution of LKF lifetimes is biased towards long-lived LKFs. The results imply that introducing inhomogeneities by using an ITD model may be one way of improving the model, but not necessarily the best one. The increased presence of long-lived LKFs in the ITD simulation suggests that one should reduce the strong feedback between ice thickness change and ice strength and instead introduce a damage parameter. This damage parameter would act as the memory of past deformation and would also feed back into the ice strength, similar to the one used in EB/MEB models (Girard *et al.*, 2011; Dansereau *et al.*, 2016). In doing so, a properly parameterized healing time could be tuned independently from parameters of the ITD formulation. We stress that a systematic parameter optimization (e.g. Massonnet *et al.*, 2014; Ungermann *et al.*, 2017) is beyond the scope of this paper and also not possible due to limited computing

resources.

The underrepresentation of fast-ice and LKFs that start from anchor points at shoals could be addressed with a grounding scheme (e.g. Lemieux *et al.*, 2015). As the missing anchor points at shoals lead to an overestimation of LKF densities in the Chukchi Sea, this parameterization may also have an impact beyond improving the representation of fast-ice and LKFs at shoals.

Although the model reproduces most LKF statistics, it completely fails to simulate the observed distribution of LKF intersection angles. This deficit can be traced back to the yield curve. The result motivated a dedicated study about the dependence of the intersection angle on the yield curve (Ringeisen *et al.*, 2019), which showed that, with a VP-rheology and classical elliptical yield curve, it is impossible to simulate intersection angles below 60° in compression, and hence to reproduce the observed intersection angles. Ringeisen *et al.* (2019) suggested to use a Mohr-Coulomb yield curve, but also note numerical implementation hurdles. We hypothesize that the density of LKFs could also increase by improving the simulated intersection angle, because with sharper intersection angles more LKFs can be accommodated in the same area.

## 4.6 Conclusion

The LKF statistics in this paper provide valuable information about which characteristics of LKFs are reproduced by the model and which modifications to the model are necessary to further improve these simulations. The model simulations, especially the one with an ITD, have LKF fields that are in remarkable agreement with satellite observations from RGPS. This reproduction of realistic deformation features is the prerequisite for regional climate studies that directly resolve atmosphere-ocean interaction processes along leads. In general, our model configuration could be used to predict deformation features in the ice. When the orientation of leads is of special interest, for example for navigation, modifications to the rheology seem in place to obtain more realistic intersection angles.

So far, scaling analyses are the main tool found in the literature to evaluate lead-resolving sea-ice models and provide insight into the material properties that govern ice dynamics. With our simulations it becomes clear that these analyses cannot discriminate between significantly different model

physics in Pan-Arctic simulations (i.e., by comparing our scaling analysis results to Rampal *et al.*, 2019). This suggests that in these scaling analyses the effect of different physics is confounded by external factors such as wind and ocean forcing or interactions with coastlines. Hence, we propose idealized experiments (e.g. as in Dansereau *et al.*, 2016; Weiss & Dansereau, 2017) to study and isolate individual mechanical properties. For the evaluation of deformation features in Pan-Arctic simulations, the direct comparison of these features should be the first choice.

We find that the computed spatio-temporal scaling exponents are mainly linked to the number of LKFs, whereas other direct inferences on other LKF properties are not obvious. For example, high temporal scaling exponents imply high intermittency, but we find that the simulation with higher scaling exponents also tends to have longer LKF lifetimes, which at first glance suggests lower intermittency. Therefore, we do not see our new method as a substitute for existing scaling analyses, but as a complement. The presented LKF statistics offer the opportunity to directly evaluate simulated deformation features. A scaling analysis tests for the material properties of ice dynamics. The decision about an appropriate metric or a combination of both metrics will always depend on the application.

# 5. Summary, conclusions and outlook

**Summary**

**Chapter 2** focuses on the statistics of sea-ice deformation in a lead-resolving sea-ice simulation. With a spatio-temporal scaling analysis I show that the simulated sea-ice deformation is strongly localized in failure zones and dominated by spontaneous fracture, i.e. that it is heterogeneous and intermittent. From the comparison with deformation data observed from satellite, I find that the observed degree of heterogeneity is reproduced by the model. Deformation is more strongly localized in summer and in regions with high drift speeds. In thick winter ice and in the Central Arctic, fewer deformation features are simulated due to the higher ice strength. The temporal variability of deformation is underestimated in the simulation. I attribute this underestimation to the lack of feedback mechanisms in the model that would allow for progressive damage in the ice. This could be addressed by the implementation of a damage parameter that reduces the ice strength based on previous deformation.

**Chapter 3** explores new ways of evaluating deformation features that account for the chaotic nature of fracture and the strong anisotropy in sea-ice deformation fields. I describe two algorithms that detect and track leads and pressure ridges, which are combined as LKFs. The detection algorithm identifies areas of high deformation rates and extracts individual LKFs. The second algorithm tracks the detected LKFs using additional drift information. Both algorithms can be applied to any drift data on a regular grid. I find that the results of both algorithms agree with hand-picked reference

data. I process all available wintertime RGPS data and compile the first multi-year data set of leads and pressure ridges in the Arctic. This LKF data set makes a comprehensive description of LKFs possible: as examples I present the distributions of LKF length, lifetime and density. A strong link of the number of LKFs to atmospheric drivers, here Arctic cyclones, is also found. Furthermore, I show the potential of these metrics of being used in model evaluation: I compare the intersection angles of LKFs in a high-resolution Arctic sea ice simulation with the RGPS LKF data set.

**Chapter 4** evaluates two high resolution sea-ice simulations in depth with the newly developed LKF metric. One of the simulations uses an active ITD model that differs in the ice strength formulation from the classical VP model. This formulation is known to lead to more heterogeneous strength fields and I test if that also results in more simulated fracture. The other simulations uses the classical two ice-class VP-model. LKFs are automatically extracted from both simulations using the algorithms presented in Chapter 3 and their spatial properties and temporal evolution are compared to the RGPS LKF data set. Interannual and seasonal variations of the number of LKFs, LKF densities, and LKF orientations in the ITD simulation are found to be in line with RGPS observations. The heavy tail of the LKF length distribution and the scale invariance of LKF curvature in both model and RGPS observations point to the self-similarity of the LKF system, which is in line with the results of a scaling analysis that show multi-fractal spatial and temporal scaling. The model overestimates the intersection angle of LKFs, which is attributed to the viscous-plastic rheology with an elliptical yield curve. The new feature-based analysis of LKF statistics is found to be useful for a comprehensive description of deformation features. As such it complements the commonly used scaling analysis, as it provides additional valuable information when comparing deformation statistics. In summary, I show that the ITD simulation reproduces the LKFs sufficiently well to study the effect of directly resolved leads in climate simulations.
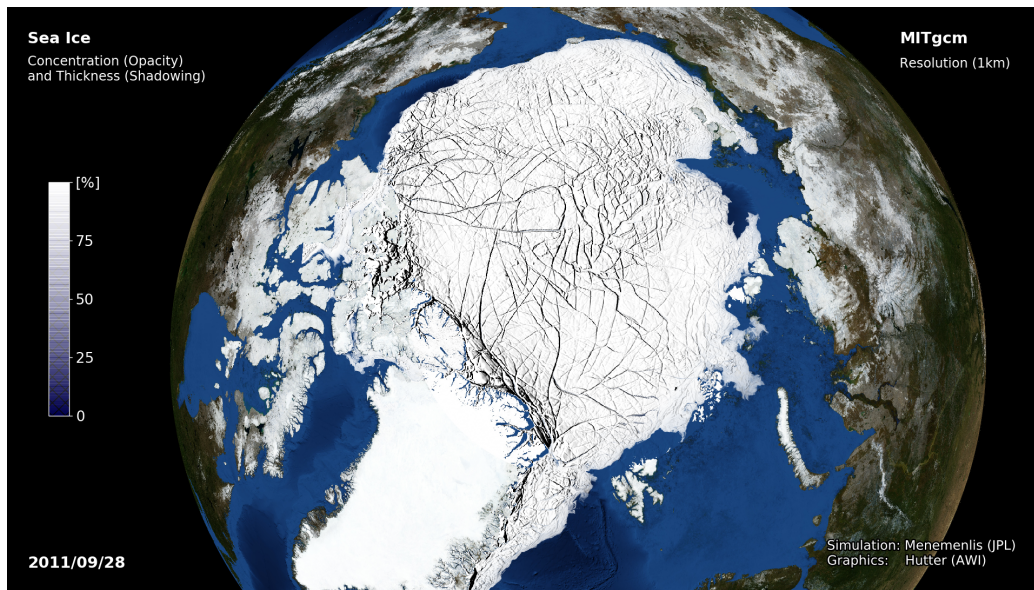
**Figure 5.1:** Leads in the 1-km sea-ice simulation presented in Chapter 2. The opacity of the ice cover illustrates its concentration and sea ice thickness is illustrated by shadowing. NASA blue marble high resolution images[1] are used as background.

## Conclusions

This thesis shows that sea-ice models using a classical viscous-plastic rheology can resolve deformation features that not only appear strikingly realistic (Fig. 5.1), but also agree in their characteristics with satellite observations. Two conditions are required for this: (1) very fine horizontal grid spacing, in this thesis 1 to 2 km, and (2) a high accuracy in solving the dynamic equations[2]. The good agreement between simulated deformation fields and satellite observations indicates that VP-models can be run at such high resolutions that individual floes are resolved despite the underlying continuum assumption (Question **Q1**, page 11). In Chapter 2, I show that simulated sea ice deformation is scale invariant. This scale invariance suggests that the common deformation physics model initially described for large scales is also valid on smaller scales. Indeed, the geometry of fracture of

---

[1]NASA Visible Earth: `https://visibleearth.nasa.gov/view_cat.php?categoryID=1484` [Status: 10.4.2019]

[2]My solver settings for VP-rheology are described in Chapter 4. For the EVP-rheology, which is more commonly used in climate models, converging solutions can be achieved following Koldunov, Danilov, Sidorenko, Hutter *et al.* (2019).

a multitude of floes resembles the cracking of a single floe or even laboratory scale ice samples (Schulson & Hibler, 1991, 2004). Even higher resolution simulations show reasonable results (Ringeisen, Losch, Tremblay & Hutter, 2019, Heorton *et al.*, 2018). This suggests that the continuum assumption does not set an upper limit for increasing the resolution, but it is likely that the 2D assumption will do so in the future. For grid spacings in the range of sea ice thickness, i.e. typically meters to tens of meters, also vertical forces need to be taken into account.

The resolved deformation structures require a thorough validation to differentiate between physically meaningful features and numerical artifacts. In this thesis, I suggest a two level validation for lead-resolving sea-ice simulations to answer Questions **Q2** and **Q3**. Firstly, the sea ice deformation is evaluated whether leads are formed by the correct physical processes. Secondly, the spatial characteristics and temporal evolution of leads and pressure ridges themselves are deduced and compared to satellite observations. In Chapter 3, I outline a detection and tracking algorithm for deformation features. The various statistics of LKFs presented in Chapter 4 test spatial and temporal properties of leads and pressure ridges that are believed to be crucial for small-scale sea-ice predictions and simulating interaction processes in climate studies. Both evaluation steps are complementary: I show that the new feature-based evaluation approach also allows to discriminate between simulations that agree in the scaling analysis, but show differences in LKF characteristics that are important in climate simulations, e.g. LKF density and lifetime.

The feature-based analysis of LKFs and the spatio-temporal scaling analysis indicate some model deficits: VP-models do not fully resolve the intermittency of sea ice deformation (see Chapter 2) and LKFs densities are found to be too low (see Chapter 4). Both can be attributed to a lack of inhomogeneities in the sea ice fields that seed the fracture of ice. An active ITD model that introduces more small-scale variability in the ice and a faster feedback between deformation and ice strength improves the intermittency of sea ice deformation and LKFs densities, but also results in too persistent deformation features. A further solution to enable progressive damage in the VP-rheology may be a new damage parameter that increases in plastic deformation and affects the ice strength as it was suggested for the MEB rheology (Girard *et al.*, 2011; Dansereau *et al.*, 2016). The misfit of the intersection angles of our simulated LKFs is caused by the standard elliptical

yield curve used in this thesis. This overestimation motivated a study by Ringeisen, Losch, Tremblay & Hutter (2019). They showed that it is impossible to reproduce the small intersection angles observed in satellite data with an elliptical yield curve and suggested to use a Mohr-Coulomb yield curve instead. In addition, I expect the implementation of grounding scheme to improve the spatial distribution of deformation features and fast ice in shallow and coastal regions in the Arctic.

The overall **goal** of this thesis to present a lead-resolving sea-ice simulations that is ready to be used in climate simulations is achieved by the comprehensive model evaluation presented in Chapters 2 and 4. In particular, the simulation using an active ITD model in Chapter 4 reproduces the deformation features that are observed by satellites. Thus, sea-ice models with similar configurations can be used in coupled climate models in order to study interaction processes along the resolved features. Since the temporal evolution of deformation features becomes more important in short-term forecast systems, modifications allowing for progressive damage will be key.

**Future perspectives**

Possible directions for future work with a focus on the sea-ice modeling components in this thesis are as follows:

- The multi-fractal scaling characteristics of the simulations in Chapter 4 agree with both RGPS and results presented for MEB (Rampal *et al.*, 2019). Note, that the MEB rheology was especially designed to fit these characteristics (Girard *et al.*, 2011), because Girard *et al.* (2009) found that the VP-rheology is not able to reproduce observed scaling properties at coarse grid resolution. Backed up by other scaling analyses (Bouchat & Tremblay, 2017; Spreen *et al.*, 2016; Hutter *et al.*, 2018) our results show that these findings cannot be generalized (especially not to high grid resolution simulations). However, it also poses the question which rheology actually represents the physics of sea-ice deformation best. Up to now, there is no thorough comparison of the different rheologies that are used in climate models. The Sea Ice Rheology Experiment (SIREx) in the framework of the Forum of Arctic Modeling and Observational Synthesis (FAMOS) co-led by Amélie Bouchat (McGill University, Montreal, Canada) and myself is

designed to answer this question. Eleven models employing four different rheologies (VP, EVP, MEB, and EAP) are compared with RGPS following the two-level approach as suggested in this thesis: firstly by means of their scaling properties (prelimiary results, Bouchat & Hutter, 2018) and secondly by the characteristics of the resolved deformation features (prelimiary results, Hutter & Bouchat, 2018).

- Chapter 2 and 4 conclude that the sea-ice deformation simulated with the VP rheology could be improved by adding a damage parameter. This would allow for progressive damage in the VP models and increase the number of LKFs. The effect of multiple differences between the VP and MEB rheology could be disentangled by implementing this damage parameterization in a VP model framework (if feasible together with the implementation of the MEB rheology in the same framework).

- The model evaluation presented in this thesis is mostly limited to wintertime from November to May. Chapter 2 highlights that sea-ice deformation in summer differs from winter deformation. A new operational data set of sea-ice deformation based on Sentinel-1 data (Pedersen *et al.*, 2015) has the potential to fill the summer gap and extend the presented evaluation up to date.

- I made the LKF detection and tracking algorithms available as open-source code offering the sea-ice model community the possibility to use the new feature-based metric for the validation of simulations and the tuning of model parameters. For example, Koldunov, Danilov, Sidorenko, Hutter *et al.* (2019) used the detection algorithm to adjust free parameters of the solver to fit the majority of LKFs. The new evaluation method could also be integrated in semi-automatic parameter optimization routines to include information on small-scale deformation. Most current parameter estimates in sea-ice models are based on coarse resolution configurations, although an increase in resolution changes the dynamic model behavior for constant model parameters (Hutter, 2015; Williams & Tremblay, 2018). Thus, lead-resolving simulations will call for such systematic parameter optimizations in the near future.

- As indicated by the title of this thesis, "Resolving leads in sea-ice models", I focus mainly on leads that are reproduced in high-resolution
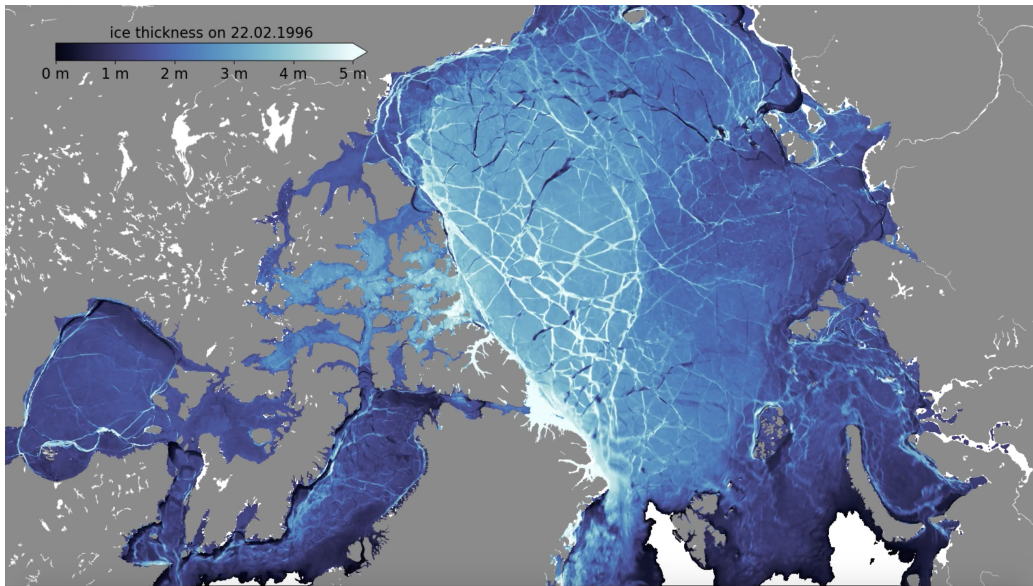
**Figure 5.2:** Pressure ridges in the 2-km sea-ice simulation presented using an active 5-class ITD model in Chapter 4. Leads are shown as dark features and pressure ridges as bright features.

configurations. The simple reason for this is that leads can be identified in lead-resolving simulations as both localized deformation and reduced sea-ice concentration and thickness (see Fig. 2.4). Thickness changes caused by pressure ridges, however, are not found as a localized increase in the mean thickness field of the simulations using the standard two-ice-class model of Hibler (1979). Using an active ITD model, I identified features that show higher mean thicknesses than their vicinity and resemble pressure ridges (Fig. 5.2). These simulated features could be compared to high-resolution thickness data (Haas *et al.*, 2008, 2010; Lindsay & Schweiger., 2013), providing valuable insights in the choice of redistribution functions and ice strength formulations in ITD models. Furthermore, they would also allow direct roughness estimates for drag formulations.

Sea-ice models that reproduce directly leads and pressure ridges have many potential applications in regional climate studies and prediction systems. The most important are listed below:

- Reliable short-term forecasts at regional scale are crucial for tactical decisions in Arctic shipping and economic operations. To forecast sea-ice fracture and drift, prediction systems depend on the proper representa-

115

tion of localized sea-ice deformation. Preliminary estimates of the pre-
dictability of deformation features (Hutter, 2015, Mohammadi-Aragh,
Goessling, Losch, Hutter & Jung, 2018) might need to be revisited in
the light of the reported short-comings in the temporal evolution of
simulated sea-ice deformation. Small-scale sea-ice forecasting requires
modern data-assimilation capabilities that provide initial conditions for
localized sea-ice deformations.

- Interaction processes between different climate components that are re-
  lated to leads and pressure ridges are of major importance in the Arctic
  climate. The opportunity to directly simulate these processes may have
  a similar potential for sea ice modelling as first eddy-resolution simu-
  lations had for ocean models. In high resolution climate simulations,
  heat and moisture transport, propagation of shortwave radiation, new
  ice growth and salt rejection would take place to a large part in leads.
  The surface roughness estimated from the presence of leads and pres-
  sure ridges could change the atmospheric and oceanic drag with feed-
  backs on atmospheric and oceanic circulation. Climate simulations of
  this kind require high-resolution in all components, which may become
  computationally feasible within the next decade.

- In these climate simulations, the detection and tracking algorithms
  presented in Chapter 3 could be used to detect the areas where the
  interactions of different climate components take place. Such an anal-
  ysis would allow to assess the interaction of sea-ice deformation with
  its atmospheric and oceanic drivers.

These examples demonstrate that lead-resolving sea-ice simulations open
new perspectives and have bright prospects in future climate simulations and
prediction systems. This thesis provides instructions for configuring such
simulations and evaluating them with observational data.

**Overall summary**

- Sea-ice models using the standard VP-rheology reproduce leads and pressure ridges at high resolution.

- I have developed a new method to evaluate these deformation features against satellite observations and combined it with the commonly used scaling analysis of sea-ice deformation.

- Sea-ice deformation localizes in the resolved deformation features showing multi-fractal heterogeniety and intermittency.

- The simulated leads and pressure ridges agree with satellite observations in their spatial characteristics and temporal evolution. Hence, simulations using an active ITD-model can be used as prototypes for the configuration of the sea-ice component in a climate model in order to directly simulate air-ice-ocean interaction processes in the Arctic.

# A. Supporting Information to Chapter 2 [1]

## A.1 Introduction

In the supporting information, we provide additional information about results and the comparison of three different scaling analyses (computation on a Eulerian grid, on a Lagrangian grid, and by using the LSE method presented in the paper). In addition, the different temporal evolution of sea-ice deformation observed in the EGPS data and in the model is illustrated in an example.

## A.2 Comparison of Eulerian, Lagrangian, and LSE scaling analysis

In the paper, we discuss three different approaches computing deformation rates at different spatial and temporal scales: (1) by averaging the strain rates computed on the Eulerian grid within fixed boxes in space and time in the Eulerian grid (abbreviated as EUL), (2) by computing strain rates from integrated virtual buoy trajectories using line integrals and thereby considering the advection of sea ice in the temporal averaging (abbreviated as LAG), and (3) by averaging the strain rates computed on the Eulerian grid within averaging boxes that are advected with the sea ice (abbreviated as LSE). For a detailed description please refer to the paper.

The total deformation fields for different time steps are shown in Fig. A.1.

---

[1]This is the supporting information to Chapter 2 which was published along with the paper '*Scaling properties of Arctic sea ice deformation in a high-resolution viscous-plastic sea ice model and in satellite observations*' by Hutter *et al.* (2018) in the journal *Journal of Geophysical Research: Oceans.*

The deformation fields of LSE and EUL (Eulerian) look very similar (sometimes the LSE method gives lower estimates), whereas larger deformation rates for LAG (Lagrangian) are clearly visible in regions of high deformation. Due to the averaging of velocity gradients over one grid cell in LSE, the velocity gradients are smoothened and the deformation rates are smaller, and hence potentially underestimated. The temporal evolution of the mean and the maximum total deformation along with the PDFs of all three approaches is shown in Fig. A.2. The mentioned spurious overestimation of the divergence rates for LAG (Lindsay & Stern, 2003; Bouillon & Rampal, 2015a) is found for EGPS. The Lagrangian method LAG is known to overestimate the true divergence rates (Lindsay & Stern, 2003; Bouillon & Rampal, 2015a); we can see that indeed the LAG divergence rates for EGPS are the largest. This overestimation might be intensified by the artificial deformation lines caused by the inhomogeneous drift composite. The latter also results in an overestimation of the shear rate for EGPS. In comparison the deformation rates computed by LSE generally agree well the original Eulerian data, although they can be slightly lower. The comparison using the same three methods on the model output is given in Fig. A.3. Please note that the PDFs of the modeled deformation rates show clearly power-law tails, which is another indication that deformation rates are strongly localized in high resolution viscous-plastic sea-ice models.

A spatio-temporal scaling analysis based completely on Lagrangian grids is provided in Fig. A.4 for both EGPS data and model results. Please note that this analysis overestimated deformation rates especially for the EGPS data due to the spurious velocity gradients in the EGPS composite. The Lagrangian scaling analysis works as follows: First we define grid cells with four virtual buoys as vertices. From the displacement of the buoys in one time step the velocities of all four vertices are computed. Next, the velocity gradients are determined using line integrals over the boundary of the cell as described in the RGPS user handbook by R. Kwok (`https://rkwok.jpl.nasa.gov/documents/RGPS-users-handbook_v2.0.pdf`, page 25). The velocity gradients of one gird cell are then averaged over different temporal scales T. To obtain strain rates at different spatial scales L, we average over a set of neighbouring grid cells, i.e. for the spatial scale of $50\,\text{km}$ we average $5\,\text{x}\,5$ neighbouring cells as one grid cell is $\sim 10\,\text{km}\,\text{x}\,10\,km$. Spatial and temporal averages are computed with an overlap of T/2 and L/2.

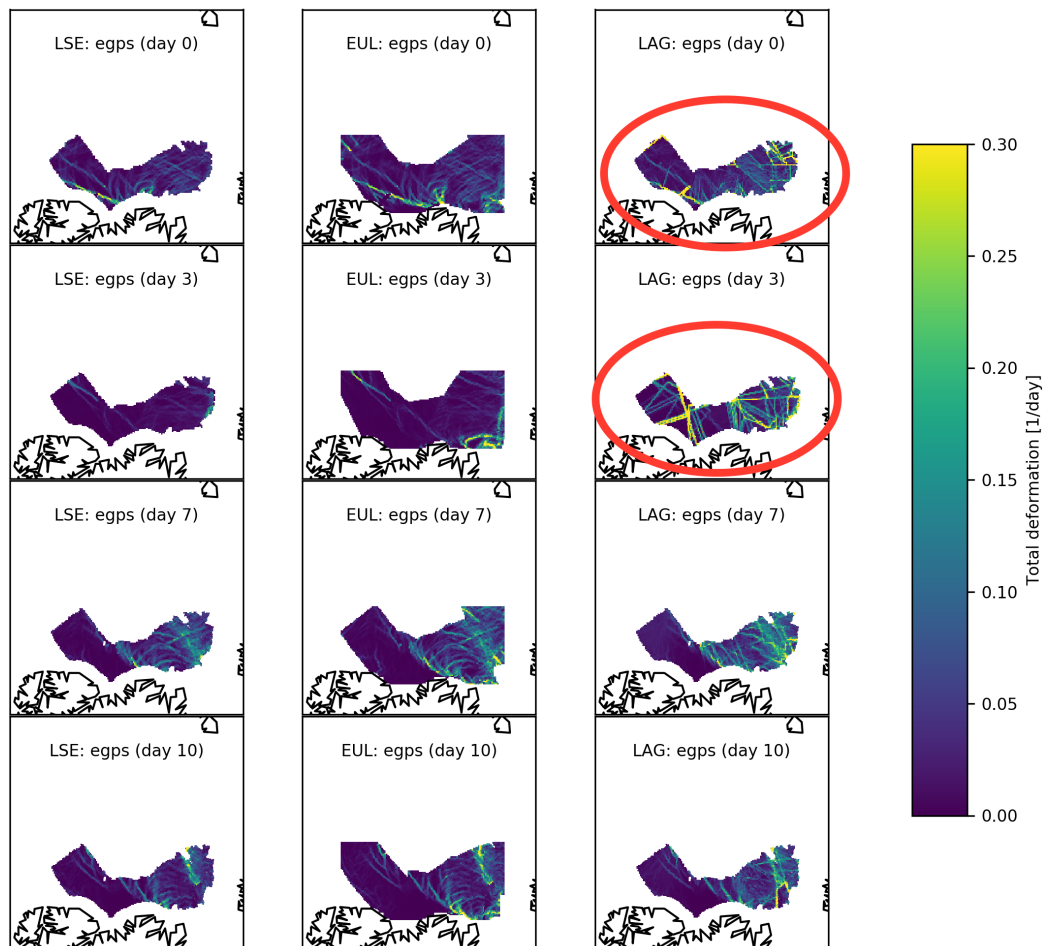An Eulerian spatial scaling analysis of the model output for the temporal

**Figure A.1:** Maps of total deformation computed by using the developed LSE method, on Eulerian grids (EUL), and by using Lagrangian trajectories (LAG). For the Lagrangian approach, the spurious deformation lines along the sub scene boundaries of the composite are marked in red. Day 0 corresponds to January 15th, 2012.
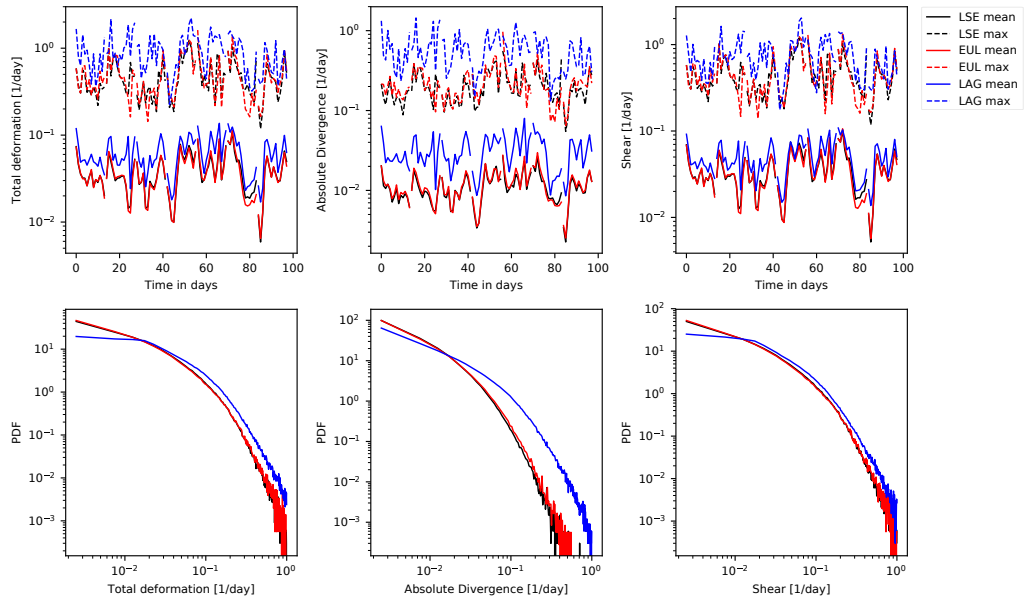
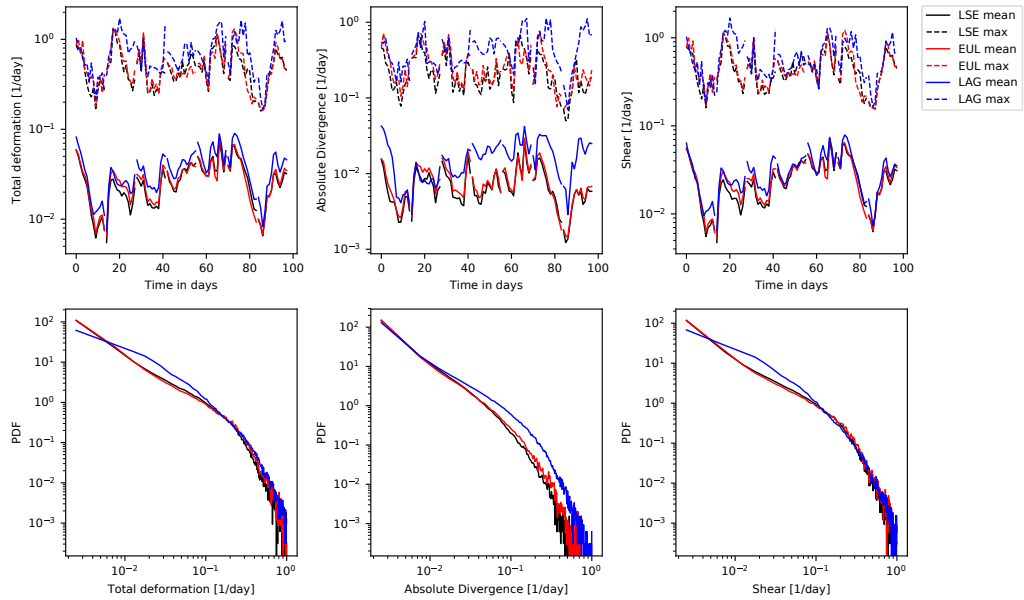**Figure A.2:** Comparison of deformation rates for EGPS data computed by different methods.



**Figure A.3:** The same comparison of deformation rates computed with three different methods but for the model output. The upper row shows the time series of maximum and mean deformation rates for January, February, and March. In the lower row the PDFs for the complete time span are given. Day 0 corresponds to January 1st, 2012.
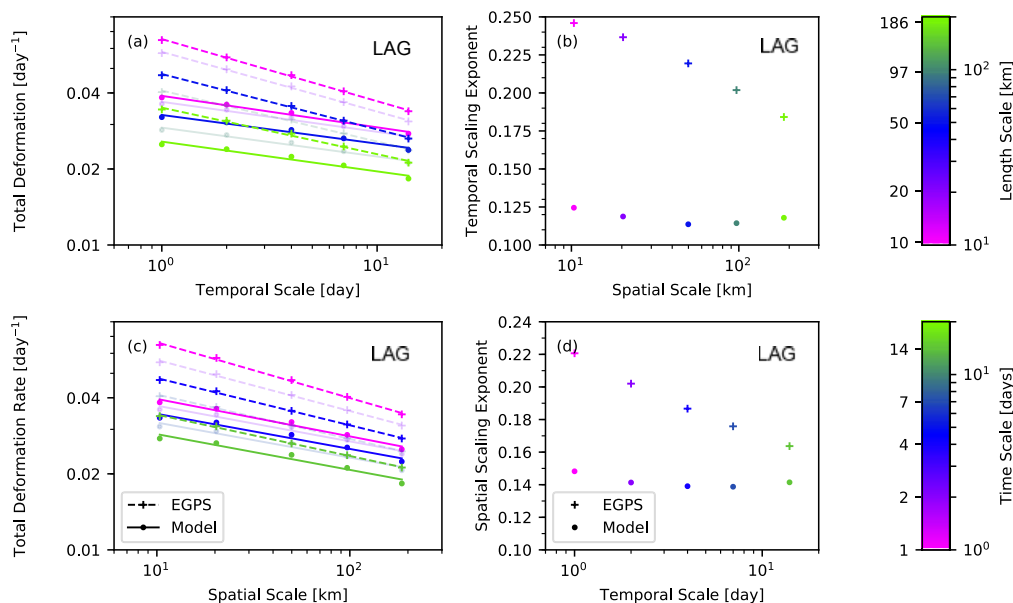
**Figure A.4:** Spatial-temporal scaling properties of model output compared to EGPS data using a Lagrangian scaling analysis. The comparison is confined to the area of the EGPS composite for each day and to the period of Jan. 1, 2012 to Mar. 31, 2012.

scale of 1 hour is given in Fig. A.5. The power-law scaling flattens for spatial scales smaller than $L < 10$ km. This flattening may reflect the spatial resolution of the wind forcing resolution or that the model requires multiple grid cells to properly represent a lead. This is discussed in the paper.

## A.3 Temporal evolution of sea-ice deformation

Figure A.6 illustrates the temporal evolution of sea-ice deformation observed in the EGPS data and in the model. Since the fracturing of sea ice is very sensitive to changes in the ice condition and the wind forcing, finding the "same" deformation line in the satellite and model data for comparison, i.e. at a similar location, and with similar orientation and time of formation, is difficult. We found a distinct feature of two parallel deformation lines forming in both satellite data and the simulation at a comparable location and time. These two parallel deformation lines are shown in the highlighted regions for the EGPS data and the model output in the time between day

123
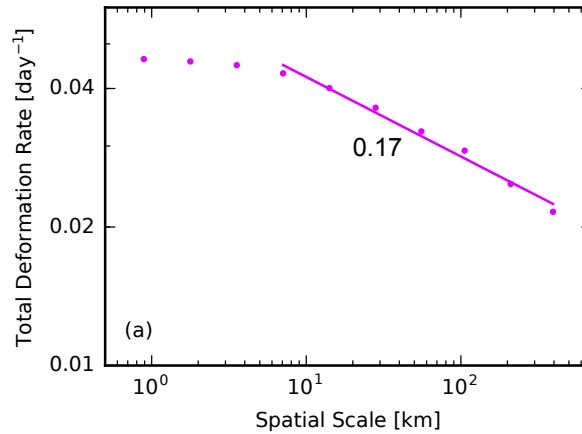
**Figure A.5:** Spatial scaling properties of model output using a Eulerian scaling analysis for the temporal scale of 1 hour. The analysis is confined to the months December to April and covers th entire model domain.

25 and 36 of the simulation (Fig. A.6). In the EGPS data, the deformation line forms within day 26 and 27. The feature persists for two days (day 28 and 29). In the following days, parts of the deformation line are reactivated. In the model the formation of both features takes more time (day 26 to 31) and it persists until day 34. Thus, the time for formation and the persistence of these deformation features is roughly two times longer in the numerical model than in the satellite observations.
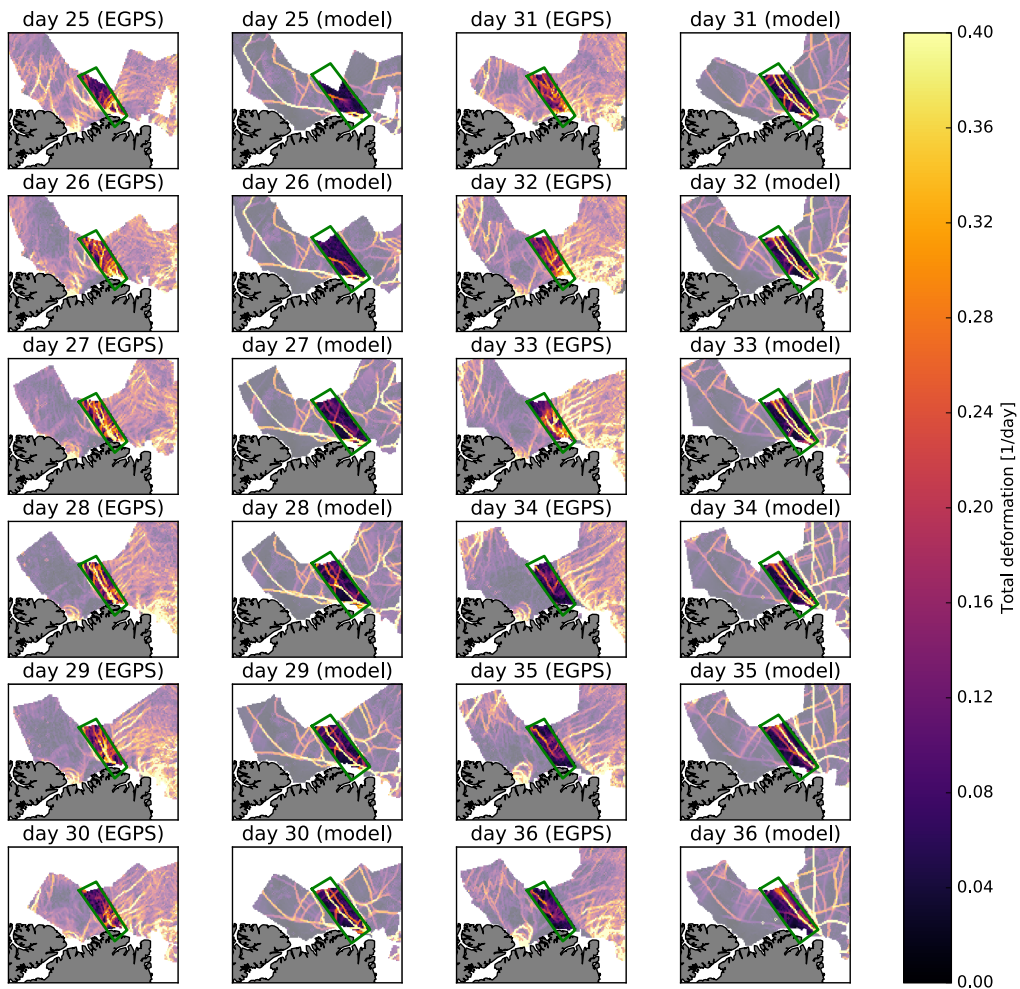
**Figure A.6:** Temporal evolution of total deformation for EGPS data and the drift data set generated from the model output using the same sampling as EGPS. Day 1 refers to the first day of the simulation that is Sept. 13, 2011.

# B. Appendix of Chapter 3 [1]

## B.1 Details on the Arctic simulation

The Arctic simulation with a refined horizontal grid spacing of 2 km using the MITgcm is based on a regional Arctic configuration (Nguyen *et al.*, 2012). The number of vertical layers is reduced to 16 with the first five layers covering the uppermost 120 m to reduce computational cost as we are only interested in sea-ice processes. The Refined Topography data set 2 (RTopo-2) (Schaffer & Timmermann, 2016) is used as bathymetry for the entire model domain. The lateral boundary conditions are taken from globally optimized ECCO-2 simulations (Menemenlis *et al.*, 2008b). We use the 3-hourly Japanese 55-year Reanalysis (JRA-55) (Kobayashi *et al.*, 2015) with a spatial resolution of 0.5625° for surface boundary conditions. The ocean temperature and salinity are initialized on January 1st, 1992 from the World Ocean Atlas 2005 (Locarnini *et al.*, 2006; Antonov *et al.*, 2006). The initial conditions for sea-ice are taken from the Polar Science Center (Zhang *et al.*, 2003). Ocean and sea ice parameterizations and parameters are from Nguyen *et al.* (2011a) with the ice strength $P^\star = 2.264 \cdot 10^4 \, \mathrm{Nm}^{-2}$. The momentum equations are solved by an iterative method and Line Successive Relaxation (LSR) of the linearized equations following Zhang & Hibler (1997). In each time step (120 s), 10 non-linear steps are made and the linear problem is iterated until an accuracy of $10^{-5}$ is reached, or 500 iterations are performed.

---

[1] This is the appendix of Chapter 3 which was published along with the paper '*Leads and ridges in Arctic sea ice from RGPS data and a new tracking algorithm*' by Hutter *et al.* (2019) in the journal *The Cryosphere*.

# C.  Co-author papers related to this thesis

The work presented in this thesis has been used to address other scientific questions outside the scope of this thesis. Here, I give a brief overview of publications, to which I contributed in the course of my PhD and which are related to lead-resolving sea ice simulations.

***"Predictability of Arctic sea ice on weather time scales"*** by Mohammadi-Aragh, Goessling, Losch, Hutter & Jung (2018) in the Journal *Scientific Reports*: This study explores the potential of lead-resolving sea-ice simulation to forecast sea ice deformation fields. The potential predictability of Arctic wintertime deformation is determined by means of different metrics and found to be strongly affected by the chaotic behavior of the atmospheric forcing. I contributed to the design of the experiments with my expertise in lead-resolving sea-ice simulations and my knowledge from preliminary studies on the predictability of LKFs (Hutter, 2015). In addition, I contributed to the discussion of the results with a focus on the physical processes of sea-ice deformation and its representation in the model.

***"Fast EVP solutions in a high-resolution sea ice model"*** by Koldunov, Danilov, Sidorenko, Hutter *et al.* (2019) in the Journal *Journal of Advances in Modeling Earth Systems*: This study shows how accurate solutions of the dynamic equations in sea-ice models can be obtained with the Elastic Viscous Plastic (EVP) rheology in high resolution configurations. The parameters of two modified versions of this solver are optimized with respect to the number of resolved LKFs. I implemented a version of the LKF

detection algorithm that uses the FESOM model output that is provided on a unstructured grid. I contributed to the discussion of the obtained results and their implications on choosing the appropriate model parameters.

***"Simulating intersection angles between conjugate faults in sea ice with different viscous–plastic rheologies"*** by Ringeisen, Losch, Tremblay & Hutter (2019) in the Journal *The Cryosphere*: This study focuses on the overestimation of intersection angles of LKFs in VP models that is presented in Chapter 3 and 4 of this thesis. The intersection angle between two LKFs forming under compressive forcing is simulated in idealized experiments with a grid spacing of 25 m using the elliptical and the Mohr Coulomb yield curve. The simulated intersection angles are compared to the analytical solutions. I contributed to the outline of this study and to the discussion on LKFs in simulations and observations.

I contributed to the writing of all three papers.

# Acknowledgments

After finishing this thesis, I want to express my thanks to many people for supporting and accompanying me during the last three years. First and foremost, to Martin Losch for his advise, guidance, and supervision that let me develop my own scientific ideas, but also prevented me from pursuing dead ends. I enjoyed our discussions, your sense of humor and the shared trips abroad. And to Thomas Jung for drawing my attention on his working group, and supporting and encouraging me whenever it was possible. I thank Michael Karcher, Christof Lüpkes, and Thomas Rackow for sharing their expertise in my PhD committee.

I would like to thank all my co-authors for turning interesting research questions into great team work. Especially, I thank Dimitris Menemenlis for providing me the opportunity to work on this unique simulation and to get to know many people at JPL. Special thanks to Amélie Bouchat for setting up FAMOS SIREx together, and spending time on getting our heads in so many tiny but important details. I thank Mischa Ungermann for accompanying me so many years at AWI as a "sea-ice PhD", for listening to me thinking out loud, and just being such a good friend.

I would like to acknowledge Anne Hutter, Mischa Ungermann, and Martin Losch for dedicated proof-reading parts of this thesis and supporting me with helpful discussions. Thanks to Thomas Rackow and Mischa Ungermann for their help with LaTeX. Finally, I would like to express my gratitude to Prof. Dr. Christian Haas for accepting to review my thesis.

Furthermore, I thank my colleagues: Mischa Ungermann, Camila Campos, and Özgür Gürses for being great and supportive office mates. Damien Ringeisen, Lorenzo Zampieri, Helge Goessling, and Thomas Rackow for inspiring discussions on sea ice and a lot of other topics. Nikolay Koldunov for sharing the passion of finding new ways to visualize data. And the whole Climate Dynamics section for a friendly and stimulating working environment

and for eating chocolate with me.

Most sincere thanks to my family for their unconditional supporting at all times. My deepest gratitude goes to Hannah and Keke for sharing a live full of joy and happiness.

# List of Figures

# List of Tables

# Abbreviations

**Table C.1:** Abbreviations

| | |
|---|---|
| AIDJEX | Arctic Ice Dynamics Join Experiment |
| AMSR-E | Advanced Microwave Scanning Radiometer - Earth Observing System |
| AVHRR | Advanced Very High Resolution Radiometer |
| DoG | Difference of Gaussian filter |
| EAP | Elastic anisotropic plastic |
| EB | Elasto-brittle |
| ECCO2 | Estimating the Circulation and Climate of the Ocean, Phase II |
| ECMWF | European Center for Medium-Range Weather Forecasts |
| EGPS | ENIVSAT geophysical processor system |
| ENVISAT | Environmental Satellite |
| ERA-Interim | ECMWF reanalysis |
| EUL | strain rate computation on Eulerian grid |
| EVP | Elastic viscous plastic |
| FAMOS | Forum of Arctic Modeling and Observational Synthesis |
| FSD | Floe size distribution |
| GCM | Global Climate Model |
| IABP | International Arctic Buoy Program |
| IBCAO | International Bathymetric Chart of the Arctic Ocean |
| ITD | Ice thickness distribution |
| ITD | simulation using an active ice thickness distribution model |
| JPL | Jet Propulsion Laboratory |
| JRA-55 | Japanese 55-year Reanalysis |
| KDE | Kernel density estimation |

*Continued on next page*

Table C.1 – *Continued from previous page*

| | |
|---|---|
| LAG | strain rate computation on Lagrangian grid |
| LKF | Linear Kinematic Feature |
| LLC | Latitude-longitude polar cap (grid configuration of MITgcm) |
| LLC4320 | LLC configuration with 4320×4320 grid points |
| LSE | Lagrangian Sampling of Eulerian gridded data |
| LSR | Line Successive Relaxation |
| MEB | Maxwell elasto-brittle |
| MHD | Modified Hausdorff Distance |
| MITgcm | Massachusetts Institute of Technology general circulation model |
| MODIS | Moderate Resolution Imaging Spectroradiometer |
| NASA | National Aeronautics and Space Agency |
| noiTD | simulation using the two ice class model |
| PDF | Probability Density Functions |
| RGPS | RADARSAT geophysical processor system |
| SAR | Synthetic-aperture radar |
| SIREx | Sea Ice Rheology Experiment |
| VP | Viscous plastic |

# Bibliography

Antonov, J. I., Locarnini, R. A., Boyer, T. P., Mishonov, A. V., & Garcia, H. E. 2006. *World Ocean Atlas 2005, Volume 2: Salinity.*

Arya, S. P. S. 1973. Contribution of form drag on pressure ridges to the air stress on Arctic ice. *Journal of Geophysical Research (1896-1977)*, **78**(30), 7092–7099.

Ashkezari, M. D., Hill, C. N., Follett, C. N., Forget, G., & Follows, M. J. 2006. Oceanic eddy detection and lifetime forecast using machine learning methods. *Geophysical Research Letters*, **43**(23), 12,234–12,241.

Asplin, M. G., Galley, R., Barber, D. G., & Prinsenberg, S. 2012. Fracture of summer perennial sea ice by ocean swell as a result of Arctic storms. *Journal of Geophysical Research: Oceans*, **117**(C6), 1–12. C06025.

Banfield, J. 1992. Skeletal modeling of ice leads. *IEEE Transactions on Geoscience and Remote Sensing*, **30**, 918–923.

Bird, K. J., Charpentier, R. R., Gautier, D. L., Houseknecht, D. W., Klett, T. R., Pitman, J. K., Moore, T. E., Schenk, C. J., Tennyson, M. E., & Wandrey, C. J. 2008. *Circum-Arctic Resource Appraisal: Estimates of Undiscovered Oil and Gas North of the Arctic Circle.*

Blanke, B., & Raynaud, S. 1997. Kinematics of the Pacific Equatorial Undercurrent: An Eulerian and Lagrangian Approach from GCM Results. *Journal of Physical Oceanography*, **27**(6), 1038–1053.

Borradaile, G. J. 2003. *Statistics of Earth Science Data: Their Distribution in Time, Space and Orientation.* Springer-Verlag Berlin Heidelberg.

BOUCHAT, A., & TREMBLAY, B. 2017. Using sea-ice deformation fields to constrain the mechanical strength parameters of geophysical sea ice. *Journal of Geophysical Research: Oceans*, **122**(7), 5802–5825.

BOUCHAT, A., & HUTTER, N. 2018. Scaling and statistical properties of sea-ice deformation fields from models participating in the FAMOS Sea-Ice Rheology Experiment. *Poster presentation on the Forum of Arctic Modeling and Observational Synthesis Meeting, Bergen, Norway, 24 October 2018 - 26 October 2018.*

BOUILLON, S., & RAMPAL, P. 2015a. On producing sea ice deformation data sets from SAR-derived sea ice motion. *The Cryosphere*, **9**(2), 663–673.

BOUILLON, S., & RAMPAL, P. 2015b. Presentation of the dynamical core of neXtSIM, a new sea ice model. *Ocean Modelling*, **91**, 23 – 37.

BRÖHAN, D., & KALESCHKE, L. 2014. A Nine-Year Climatology of Arctic Sea Ice Lead Orientation and Frequency from AMSR-E. *Remote Sensing*, **6**(2), 1451–1475.

CASTELLANI, G., LOSCH, M., UNGERMANN, M., & GERDES, R. 2018. Sea-Ice Drag as Function of Deformation and Ice Cover: Effects on Simulated Sea Ice and Ocean Circulation in the Arctic. *Ocean Modelling*, **128**, 48–66.

CHEVALLIER, M., MASSONNET, F., GOESSLING, H., GUÉMAS, V., & JUNG, T. 2019. Chapter 10 - The Role of Sea Ice in Sub-seasonal Predictability. *Pages 201 – 221 of:* ROBERTSON, A. W., & VITART, F. (eds), *Sub-Seasonal to Seasonal Prediction.* Elsevier.

CLAUSET, A., SHALIZI, C., & NEWMAN, M. 2009. Power-Law Distributions in Empirical Data. *SIAM Review*, **51**(4), 661–703.

COON, M. D., MAYKUT, G. A., PRITCHARD, R. S., ROTHROCK, D. A., & THORNDIKE, A. S. 1974. Modeling the pack ice as an elastic-plastic material. *AIDJEX Bull.*, **24**, 1–105.

COON, M., KWOK, R., LEVY, G., PRUIS, M., SCHREYER, H., & SULSKY, D. 2007. Arctic Ice Dynamics Joint Experiment (AIDJEX) assumptions revisited and found inadequate. *Journal of Geophysical Research: Oceans*, **112**(C11).

DANSEREAU, V., WEISS, J., SARAMITO, P., & LATTES, P. 2016. A Maxwell elasto-brittle rheology for sea ice modelling. *The Cryosphere*, **10**(3), 1339–1359.

DEE, D. P., UPPALA, S. M., SIMMONS, A. J., BERRISFORD, P., POLI, P., KOBAYASHI, S., ANDRAE, U., BALMASEDA, M. A., BALSAMO, G., BAUER, P., BECHTOLD, P., BELJAARS, A. C. M., VAN DE BERG, L., BIDLOT, J., BORMANN, N., DELSOL, C., DRAGANI, R., FUENTES, M., GEER, A. J., HAIMBERGER, L., HEALY, S. B., HERSBACH, H., HOLM, E. V., ISAKSEN, L., KÅLLBERG, P., KÖHLER, M., MATRICARDI, M., MCNALLY, A. P., MONGE-SANZ, B. M., MORCRETTE, J.-J., PARK, B. K., PEUBEY, C., DE ROSNAY, P., TAVOLATO, C., THÉPAUT, J.-N., & VITART, F. 2011. The ERA-Interim reanalysis: Configuration and performance of the data assimilation system. *Q. J. R. Meteorol. Soc.*, **137**(656), 553–597.

DEMPSEY, J., XIE, Y., ADAMSON, R., & FARMER, D. 2012. Fracture of a ridged multi-year Arctic sea ice floe. *Cold Regions Science and Technology*, **76-77**, 63 – 68. Max Coon Special issue.

DUBUISSON, M.-P., & JAIN, A. 1994. A modified Hausdorff distance for object matching. *Pages 566–568 of: Proceedings of 12th International Conference on Pattern Recognition*, vol. 1. IEEE Comput. Soc. Press.

DUKHOVSKOY, D. S., UBNOSKE, J., BLANCHARD-WRIGGLESWORTH, E., HIESTER, H. R., & PROSHUTINSKY, A. 2015. Skill metrics for evaluation and comparison of sea ice models. *Journal of Geophysical Research: Oceans*, **120**(9), 5910–5931.

EGUÍLUZ, V. M., FERNÁNDEZ-GRACIA, J., IRIGOIEN, X., & DUARTE, C. M. 2016. A quantitative assessment of Arctic shipping in 2010 - 2014. *Scientific Reports*, **6**(30682).

ERLINGSSON, B. 1988. Two-dimensional deformation patterns in sea ice. *Journal of Glaciology*, **34**(118), 301–308.

EUROPEAN CENTRE FOR MEDIUM-RANGE WEATHER FORECASTS. 2011. *ECMWF's Operational Model Analysis, starting in 2011*.

FELTHAM, D. L. 2008. Sea Ice Rheology. *Annual Review of Fluid Mechanics*, **40**(1), 91–112.

FORGET, G., CAMPIN, J.-M., HEIMBACH, P., HILL, C. N., PONTE, R. M., & WUNSCH, C. 2015. ECCO version 4: an integrated framework for non-linear inverse modeling and global ocean state estimation. *Geosci. Model Dev.*, **8**, 3071–3104.

GIRARD, L., WEISS, J., MOLINES, J. M., BARNIER, B., & BOUILLON, S. 2009. Evaluation of high-resolution sea ice models on the basis of statistical and scaling properties of Arctic sea ice drift and deformation. *Journal of Geophysical Research: Oceans*, **114**(C8), 1–15.

GIRARD, L., BOUILLON, S., WEISS, J., AMITRANO, D., FICHEFET, T., & LEGAT, V. 2011. A new modeling framework for sea-ice mechanics based on elasto-brittle rheology. *Annals of Glaciology*, **52**(57), 123–132.

GUEMAS, V., BLANCHARD-WRIGGLESWORTH, E., CHEVALLIER, M., DAY, J. J., DQU, M., DOBLAS-REYES, F. J., FUKAR, N. S., GERME, A., HAWKINS, E., KEELEY, S., KOENIGK, T., SALAS Y MLIA, D., & TIETSCHE, S. 2016. A review on Arctic sea-ice predictability and prediction on seasonal to decadal time-scales. *Quarterly Journal of the Royal Meteorological Society*, **142**(695), 546–561.

HAAS, C., PFAFFLING, A., HENDRICKS, S., RABENSTEIN, L., ETIENNE, J.-L., & RIGOR, I. 2008. Reduced ice thickness in Arctic Transpolar Drift favors rapid ice retreat. *Geophysical Research Letters*, **35**(17).

HAAS, C., HENDRICKS, S., EICKEN, H., & HERBER, A. 2010. Synoptic airborne thickness surveys reveal state of Arctic sea ice cover. *Geophysical Research Letters*, **37**(9).

HALL, C. M., & SAARINEN, J. 2010. Polar Tourism: Definitions and Dimensions. *Scandinavian Journal of Hospitality and Tourism*, **10**(4), 448–467.

HEORTON, H. D. B. S., FELTHAM, D. L., & TSAMADOS, M. 2018. Stress and deformation characteristics of sea ice in a high-resolution, anisotropic sea ice model. *Philosophical Transactions of the Royal Society A: Mathematical, Physical and Engineering Sciences*, **376**(2129), 20170349.

HERMAN, A. 2016. Discrete-Element bonded-particle Sea Ice model DESIgn, version 1.3a – model description and implementation. *Geoscientific Model Development*, **9**(3), 1219–1241.

HERMAN, A. 2017. Wave-induced stress and breaking of sea ice in a coupled hydrodynamic discrete-element wave–ice model. *The Cryosphere*, **11**(6), 2711–2725.

HERMAN, A., & GLOWACKI, O. 2012. Variability of sea ice deformation rates in the Arctic and their relationship with basin-scale wind forcing. *The Cryosphere*, **6**(6), 1553–1559.

HIBLER, W. D. 1979. A Dynamic Thermodynamic Sea Ice Model. *J. Phys. Oceanogr.*, **9**, 815–846.

HOLLOWAY, G., & PROSHUTINSKY, A. 2007. Role of tides in Arctic ocean/ice climate. *Journal of Geophysical Research: Oceans*, **112**(C4), 1–10. C04S06.

HOPKINS, M. A., & THORNDIKE, A. S. 2006. Floe formation in Arctic sea ice. *Journal of Geophysical Research: Oceans*, **111**(C11).

HORVAT, C., & TZIPERMAN, E. 2015. A prognostic model of the sea-ice floe size and thickness distribution. *The Cryosphere*, **9**(6), 2119–2134.

HORVAT, C., TZIPERMAN, E., & CAMPIN, J.-M. 2016. Interaction of sea ice floe size, ocean eddies, and sea ice melting. *Geophysical Research Letters*, **43**(15), 8083–8090.

HUNKE, E. C., LIPSCOMB, W. H., & TURNER, A. K. 2010. Sea-ice models for climate study: retrospective and new directions. *Journal of Glaciology*, **56**(200), 11621172.

HUTCHINGS, J. K., HEIL, P., STEER, A., & HIBLER, W. D. 2012. Sub-synoptic scale spatial variability of sea ice deformation in the western Weddell Sea during early summer. *Journal of Geophysical Research: Oceans*, **117**(C1), 1–16. C01002.

HUTCHINGS, J. K., HEIL, P., & HIBLER, W. D. 2005. Modeling Linear Kinematic Features in Sea Ice. *Monthly Weather Review*, **133**, 3481–3497.

HUTCHINGS, J. K., ROBERTS, A., GEIGER, C., & RICHTER-MENGE, J. 2011. Spatial and temporal characterization of sea-ice deformation. *Annals of Glaciology*, **52**(57), 360–368.

HUTTER, N., & LOSCH, M. 2019. Feature-based comparison of sea-ice deformation in lead-resolving sea-ice simulations. *submitted to The Cryosphere.*

HUTTER, N., ZAMPIERI, L., & LOSCH, M. 2019. Leads and ridges in Arctic sea ice from RGPS data and a new tracking algorithm. *The Cryosphere,* **13**(2), 627–645.

HUTTER, N. 2015 (September). *Viscous-plastic sea-ice models at very high resolution.* Master's Thesis, University of Bremen, Alfred Wegener Institute, Helmholtz Centre for Polar and Marine research.

HUTTER, N. 2019. lkf_tools: a code to detect and track Linear Kinematic Features (LKFs) in sea-ice deformation data. *Zenodo,* doi: 10.5281/zenodo.2560078.

HUTTER, N., & BOUCHAT, A. 2018. Comparing deformation features of sea ice models contributing to the FAMOS Sea-Ice Rheology Experiment. *Oral presentation on the Forum of Arctic Modeling and Observational Synthesis Meeting, Bergen, Norway, 24 October 2018 - 26 October 2018.*

HUTTER, N., LOSCH, M., & MENEMENLIS, D. 2018. Scaling Properties of Arctic Sea Ice Deformation in a High-Resolution Viscous-Plastic Sea Ice Model and in Satellite Observations. *Journal of Geophysical Research: Oceans,* **123**(1), 672–687.

HUTTER, N., ZAMPIERI, L., & LOSCH, M. 2019. *Linear Kinematic Features (leads & pressure ridges) detected and tracked in RADARSAT Geophysical Processor System (RGPS) sea-ice deformation data from 1997 to 2008.* Supplement to: Hutter, N et al. (2019): Leads and ridges in Arctic sea ice from RGPS data and a new tracking algorithm. The Cryosphere, https://doi.org/10.5194/tc-2018-207.

IACOZZA, J., & BARBER, D. G. 1999. An examination of the distribution of snow on seaice. *Atmosphere-Ocean,* **37**(1), 21–51.

JAKOBSSON, M., MACNAB, R., MAYER, L., ANDERSON, R., EDWARDS, M., HATZKY, J., SCHENKE, H. W., & JOHNSON, P. 2008. An improved bathymetric portrayal of the Arctic Ocean: Implications for ocean modeling and geological, geophysical and oceanographic analyses. *Geophysical Research Letters,* **35**(7).

JUNG, T., GORDON, N. D., BAUER, P., BROMWICH, D. H., CHEVALLIER, M., DAY, J. J., DAWSON, J., DOBLAS-REYES, F., FAIRALL, C., GOESSLING, H. F., HOLLAND, M., INOUE, J., IVERSEN, T., KLEBE, S., LEMKE, P., LOSCH, M., MAKSHTAS, A., MILLS, B., NURMI, P., PEROVICH, D., REID, P., RENFREW, I. A., SMITH, G., SVENSSON, G., TOLSTYKH, M., & YANG, Q. 2016. Advancing Polar Prediction Capabilities on Daily to Seasonal Time Scales. *Bulletin of the American Meteorological Society*, **97**(9), 1631–1647.

KOBAYASHI, S., OTA, Y., HARADA, Y., EBITA, A., MORIYA, M., ONODA, H., ONOGI, K., KAMAHORI, H., KOBAYASHI, C., ENDO, H., MIYAOKA, K., & TAKAHASHI, K. 2015. The JRA-55 Reanalysis: General Specifications and Basic Characteristics. *Journal of the Meteorological Society of Japan. Ser. II*, **93**(1), 5–48.

KOLDUNOV, N. V., DANILOV, S., SIDORENKO, D., HUTTER, N., LOSCH, M., GOESSLING, H., RAKOWSKY, N., SCHOLZ, P., SEIN, D., WANG, Q., & JUNG, T. 2019. Fast EVP solutions in a high-resolution sea ice model. *Journal of Advances in Modeling Earth Systems*.

KWOK, R. 1998. The RADARSAT Geophysical Processor System. *Pages 235–257 of: Analysis of SAR Data of the Polar Oceans*. Springer Berlin Heidelberg.

KWOK, R. 2006. Contrasts in sea ice deformation and production in the Arctic seasonal and perennial ice zones. *Journal of Geophysical Research: Oceans*, **111**(C11). C11S22.

KWOK, R. 2010. Satellite remote sensing of sea-ice thickness and kinematics: a review. *Journal of Glaciology*, **56**(200), 11291140.

KWOK, R., HUNKE, E. C., MASLOWSKI, W., MENEMENLIS, D., & ZHANG, J. 2008. Variability of sea ice simulations assessed with RGPS kinematics. *Journal of Geophysical Research: Oceans*, **113**(C11), 1–20. C11012.

KWOK, R. 2001. Deformation of the Arctic Ocean Sea Ice Cover between November 1996 and April 1997: A Qualitative Survey. *Pages 315–322 of:* DEMPSEY, J., & SHEN, H. (eds), *IUTAM Symposium on Scaling Laws in*

*Ice Mechanics and Ice Dynamics.* Solid Mechanics and Its Applications, vol. 94. Springer Netherlands.

LAHERRÈRE, J., & SORNETTE, D. 1998. Stretched exponential distributions in nature and economy: "fat tails" with characteristic scales. *The European Physical Journal B - Condensed Matter and Complex Systems*, **2**(4), 525–539.

LARGE, W. G., & YEAGER, S. G. 2004. *Diurnal to decadal global forcing for ocean and sea-ice models: The data sets and flux climatologies.* Tech. Note TN-460+STR. NCAR, Boulder, CO.

LARGE, W. G., MCWILLIAMS, J. C., & DONEY, S. 1994. Oceanic vertical mixing: A review and a model with a nonlocal boundary layer parameterization. *Rev. Geophysics*, **32**(4), 363–403.

LEMIEUX, J.-F., TREMBLAY, L. B., DUPONT, F., PLANTE, M., SMITH, G. C., & DUMONT, D. 2015. A basal stress parameterization for modeling landfast ice. *Journal of Geophysical Research: Oceans*, **120**(4), 3157–3173.

LEMIEUX, J.-F., BOUILLON, S., DUPONT, F., FLATO, G., LOSCH, M., RAMPAL, P., TREMBLAY, L.-B., VANCOPPENOLLE, M., & WILLIAMS, T. 2017. *Sea Ice Physics and Modelling.* Cambridge University Press. Page 1050.

LEPPÄRANTA, M. 2011. *The Drift of Sea Ice.* Springer Berlin Heidelberg.

LINDSAY, R., & SCHWEIGER., A. J. 2013. updated 2017. Unified Sea Ice Thickness Climate Data Record, 1947 Onward, Version 1. *NSIDC: National Snow and Ice Data Center,Boulder, Colorado USA.*

LINDSAY, R. W., & ROTHROCK, D. A. 1995. Arctic sea ice leads from advanced very high resolution radiometer images. *Journal of Geophysical Research: Oceans*, **100**(C3), 4533–4544.

LINDSAY, R. W., & STERN, H. L. 2003. The RADARSAT Geophysical Processor System: Quality of Sea Ice Trajectory and Deformation Estimates. *Journal of Atmospheric and Oceanic Technology*, **20**(9), 1333–1347.

LINDSAY, R. W., ZHANG, J., & ROTHROCK, D. A. 2003. Sea-ice deformation rates from satellite measurements and in a model. *Atmosphere-Ocean*, **41**(1), 35–47.

LINOW, S., & DIERKING, W. 2017. Object-Based Detection of Linear Kinematic Features in Sea Ice. *Remote Sensing*, **9**(5).

LIPSCOMB, W. H., HUNKE, E. C., MASLOWSKI, W., & JAKACKI, J. 2007. Ridging, strength, and stability in high-resolution sea ice models. *Journal of Geophysical Research: Oceans*, **112**(C3).

LOCARNINI, R. A., MISHONOV, A. V., ANTONOV, J. I., BOYER, T. P., & GARCIA, H. E. 2006. *World Ocean Atlas 2005, Volume 1: Temperature.*

LOSCH, M., MENEMENLIS, D., CAMPIN, J.-M., HEIMBACH, P., & HILL, C. 2010. On the formulation of sea-ice models. Part 1: Effects of different solver implementations and parameterizations. *Ocean Modelling*, **33**, 129–144.

LOSCH, M., FUCHS, A., LEMIEUX, J.-F., & VANSELOW, A. 2014. A parallel Jacobian-free Newton-Krylov solver for a coupled sea ice-ocean model. *Journal of Computational Physics*, **257, Part A**, 901–911.

MAHER, P. T. 2017. *Tourism Futures in the Arctic.* Cham: Springer International Publishing. Pages 213–220.

MAHONEY, A., EICKEN, H., & SHAPIRO, L. 2007. How fast is landfast sea ice? A study of the attachment and detachment of nearshore ice at Barrow, Alaska. *Cold Regions Science and Technology*, **47**(3), 233 – 255.

MAHONEY, A. R., EICKEN, H., SHAPIRO, L. H., HEINRICHS, T., MEYER, F. J., & GAYLORD, A. G. 2012. *Mapping and Characterization of Recurring Spring Leads and Landfast Ice in the Beaufort and Chukchi Seas.* Final Report: OCS Study BOEM 2012-067.

MARKO, J. R., & THOMSON, R. E. 1977. Rectilinear leads and internal motions in the ice pack of the Western Arctic Ocean. *Journal of Geophysical Research*, **82**(6), 979–987.

MARSAN, D., & WEISS, J. 2010. Space/time coupling in brittle deformation at geophysical scales. *Earth and Planetary Science Letters*, **296**(34), 353 – 359.

MARSAN, D., STERN, H., LINDSAY, R., & WEISS, J. 2004. Scale Dependence and Localization of the Deformation of Arctic Sea Ice. *Phys. Rev. Lett.*, **93**(Oct), 178501.

MARSHALL, J., ADCROFT, A., HILL, C., PERELMAN, L., & HEISEY, C. 1997. A Finite-Volume, Incompressible Navier Stokes Model for Studies of the Ocean on Parallel Computers. *J. Geophys. Res.*, **102**(C3), 5753–5766.

MASSONNET, F., GOOSSE, H., FICHEFET, T., & COUNILLON, F. 2014. Calibration of sea ice dynamic parameters in an ocean-sea ice model using an ensemble Kalman filter. *Journal of Geophysical Research: Oceans*, **119**(7), 4168–4184.

MAYKUT, G. A., & UNTERSTEINER, N. 1971. Some results from a time-dependent thermodynamic model of sea ice. *Journal of Geophysical Research (1896-1977)*, **76**(6), 1550–1575.

MENEMENLIS, D., CAMPIN, J., HEIMBACH, P., HILL, C., LEE, T., NGUYEN, A., SCHODLOK, M., & ZHANG, H. 2008a. ECCO2: High Resolution Global Ocean and Sea Ice Data Synthesis. *Merc. Oc. Quart. News.*, **31**, 13–21.

MENEMENLIS, D., CAMPIN, J., HEIMBACH, P., HILL, C., LEE, T., NGUYEN, A., SCHODLOK, M., & ZHANG, H. 2008b. ECCO2: High Resolution Global Ocean and Sea Ice Data Synthesis. *Merc. Oc. Quart. News.*, **31**, 13–21.

MILES, M. W., & BARRY, R. G. 1998. A 5-year satellite climatology of winter sea ice leads in the western Arctic. *Journal of Geophysical Research: Oceans*, **103**(C10), 21723–21734.

MITGCM GROUP. 2017. *MITgcm User Manual.* Online documentation. MIT/EAPS, Cambridge, MA 02139, USA. `http://mitgcm.org/public/r2_manual/latest/online_documents`.

MOHAMMADI-ARAGH, M., GOESSLING, H. F., LOSCH, M., HUTTER, N., & JUNG, T. 2018. Predictability of Arctic sea ice on weather time scales. *Scientific reports*, **8**.

MOURRE, B., AGUIAR, E., JUZA, M., HERNANDEZ-LASHERAS, J., REYES, E., HESLOP, E., ESCUDIER, R., CUTOLO, E., RUIZ, S., MASON, E., PASCUAL, A., & TINTORÉ, J. 2018. Assessment of High-Resolution Regional Ocean Prediction Systems Using Multi-Platform Observations: Illustrations in the Western Mediterranean Sea. *Pages 663–694*

*of:* CHASSIGNET, E., PASCUAL, A., TINTORÉ, J., & VERRON, J. (eds), *New Frontiers in Operational Oceanography.* GODAE Ocean View.

MURASHKIN, D., SPREEN, G., HUNTEMANN, M., & DIERKING, W. 2018. Method for detection of leads from Sentinel-1 SAR images. *Annals of Glaciology,* **59**, 124136.

NANSEN, F. 1897. *Farthest North: Being the Record of a Voyage of Exploration of the Ship Fram, 189396, and of a Fifteen Months' Sleigh Journey by Dr. Nansen and Lieut. Johansen.* Vol. 2. Harper & Brothers Publishers.

NGUYEN, A. T., MENEMENLIS, D., & KWOK, R. 2009. Improved modeling of the Arctic halocline with a subgrid-scale brine rejection parameterization. *J. Geophys. Res.,* **114**, C11014.

NGUYEN, A. T., MENEMENLIS, D., & KWOK, R. 2011a. Arctic ice-ocean simulation with optimized model parameters: approach and assessment. *J. Geophys. Res.,* **116**, C04025.

NGUYEN, A. T., MENEMENLIS, D., & KWOK, R. 2011b. Arctic ice-ocean simulation with optimized model parameters: approach and assessment. *J. Geophys. Res.,* **116**, C04025.

NGUYEN, A. T., KWOK, R., & MENEMENLIS, D. 2012. Source and Pathway of the Western Arctic Upper Halocline in a Data-Constrained Coupled Ocean and Sea Ice Model. *Journal of Physical Oceanography,* **42**(5), 802–823.

NOMURA, D., AOKI, S., SIMIZU, D., & IIDA, T. 2018. Influence of Sea Ice Crack Formation on the Spatial Distribution of Nutrients and Microalgae in Flooded Antarctic Multiyear Ice. *Journal of Geophysical Research: Oceans,* **123**(2), 939–951.

OIKKONEN, A., HAAPALA, J., LENSU, M., KARVONEN, J., & ITKIN, P. 2017. Small-scale sea ice deformation during N-ICE2015: From compact pack ice to marginal ice zone. *Journal of Geophysical Research: Oceans,* **122**(6), 5105–5120.

OVERLAND, J. E., & WANG, M. 2013. When will the summer Arctic be nearly sea ice free? *Geophysical Research Letters,* **40**(10), 2097–2101.

Pedersen, L. T., Saldo, R., & Fenger-Nielsen, R. 2015 (July). Sentinel-1 results: Sea ice operational monitoring. *Pages 2828–2831 of: 2015 IEEE International Geoscience and Remote Sensing Symposium (IGARSS)*.

Ponte, R. M., Chaudhuri, A. H., & Vinogradov, S. V. 2015. Long-Period Tides in an Atmospherically Driven, Stratified Ocean. *J. Phys. Oceanogr.*, **45**(7), 1917–1928.

Pritchard, R. S. 1988. Mathematical characteristics of sea ice dynamics models. *Journal of Geophysical Research: Oceans*, **93**(C12), 15609–15618.

Rampal, P., Weiss, J., Marsan, D., Lindsay, R., & Stern, H. 2008. Scaling properties of sea ice deformation from buoy dispersion analysis. *Journal of Geophysical Research: Oceans*, **113**(C3), 1–12.

Rampal, P., Weiss, J., & Marsan, D. 2009. Positive trend in the mean speed and deformation rate of Arctic sea ice, 19792007. *Journal of Geophysical Research: Oceans*, **114**(C5).

Rampal, P., Bouillon, S., Ólason, E., & Morlighem, M. 2016. neXtSIM: a new Lagrangian sea ice model. *The Cryosphere*, **10**(3), 1055–1073.

Rampal, P., Dansereau, V., Olason, E., Bouillon, S., Williams, T., & Samaké, A. 2019. On the multi-fractal scaling properties of sea ice deformation. *The Cryosphere Discussions*, **2019**, 1–45.

Richter-Menge, J. A., McNutt, S. L., Overland, J. E., & Kwok, R. 2002. Relating Arctic pack ice stress and deformation under winter conditions. *Journal of Geophysical Research: Oceans*, **107**(C10), SHE 15-1–SHE 15-13.

Ringeisen, D., Losch, M., Tremblay, L. B., & Hutter, N. 2019. Simulating intersection angles between conjugate faults in sea ice with different viscous–plastic rheologies. *The Cryosphere*, **13**(4), 1167–1186.

Roach, L. A., Horvat, C., Dean, S. M., & Bitz, C. M. 2018. An Emergent Sea Ice Floe Size Distribution in a Global Coupled Ocean-Sea Ice Model. *Journal of Geophysical Research: Oceans*, **123**(6), 4322–4337.

Rocha, C. B., Chereskin, T. K., Gille, S. T., & Menemenlis, D. 2016a. Mesoscale to Submesoscale Wavenumber Spectra in Drake Passage. *Journal of Physical Oceanography*, **46**(2), 601–620.

Rocha, C. B., Gille, S. T., Chereskin, T. K., & Menemenlis, D. 2016b. Seasonality of submesoscale dynamics in the Kuroshio Extension. *Geophysical Research Letters*, **43**(21), 11,304–11,311. 2016GL071349.

Röhrs, J., & Kaleschke, L. 2012. An algorithm to detect sea ice leads by using AMSR-E passive microwave imagery. *The Cryosphere*, **6**(2), 343–352.

Rothrock, D. A. 1975. The energetics of the plastic deformation of pack ice by ridging. *Journal of Geophysical Research*, **80**(33), 4514–4519.

Rothrock, D. A., & Thorndike, A. S. 1984. Measuring the sea ice floe size distribution. *Journal of Geophysical Research: Oceans*, **89**(C4), 6477–6486.

Schaffer, J., & Timmermann, R. 2016. *Greenland and Antarctic ice sheet topography, cavity geometry, and global bathymetry (RTopo-2), links to NetCDF files.* Supplement to: Schaffer, Janin; Timmermann, Ralph; Arndt, Jan Erik; Kristensen, Steen Savstrup; Mayer, Christoph; Morlighem, Mathieu; Steinhage, Daniel (2016): A global, high-resolution data set of ice sheet topography, cavity geometry, and ocean bathymetry. Earth System Science Data, 8(2), 543-557, https://doi.org/10.5194/essd-8-543-2016.

Schreyer, H. L., Sulsky, D. L., Munday, L. B., Coon, M. D., & Kwok, R. 2006. Elastic-decohesive constitutive model for sea ice. *Journal of Geophysical Research: Oceans*, **111**(C11).

Schulson, E. M., & Hibler, W. D. 1991. The fracture of ice on scales large and small: Arctic leads and wing cracks. *Journal of Glaciology*, **37**(127), 319–322.

Schulson, E. M., & Hibler, W. D. 2004. Fracture of the winter sea ice cover on the Arctic ocean. *Comptes Rendus Physique*, **5**(7), 753 – 767. Ice: from dislocations to icy satellites.

SERREZE, M. 2009. *Northern Hemisphere Cyclone Locations and Characteristics from NCEP/NCAR Reanalysis Data, Version 1.* Boulder, Colorado USA. NSIDC: National Snow and Ice Data Center. Data retrieved August 2018.

SMITH, L. C., & STEPHENSON, S. R. 2013. New Trans-Arctic shipping routes navigable by midcentury. *Proceedings of the National Academy of Sciences*, **110**(13), E1191–E1195.

SPREEN, G., KWOK, R., MENEMENLIS, D., & NGUYEN, A. T. 2016. Sea Ice Deformation in a Coupled Ocean-Sea Ice Model and in Satellite Remote Sensing Data. *The Cryosphere Discussions*, **2016**, 1–37.

SQUIRE, V. A., DUGAN, J. P., WADHAMS, P., ROTTIER, P. J., & LIU, A. K. 1995. Of Ocean Waves and Sea Ice. *Annual Review of Fluid Mechanics*, **27**(1), 115–168.

STAMOULIS, C., & DYER, I. 2000. Acoustically derived ice-fracture velocity in central Arctic pack ice. *The Journal of the Acoustical Society of America*, **108**(1), 96–104.

STERN, H. L., & LINDSAY, R. W. 2009. Spatial scaling of Arctic sea ice deformation. *Journal of Geophysical Research: Oceans*, **114**(C10), n/a–n/a. C10017.

STERN, H., SCHWEIGER, A., ZHANG, J., & STEELE, M. 2018. On reconciling disparate studies of the sea-ice floe size distribution. *Elementa Science of the Anthropocene*, **6**(49), 1–16.

STROEVE, J., HAMILTON, L. C., BITZ, C. M., & BLANCHARD-WRIGGLESWORTH, E. 2014. Predicting September sea ice: Ensemble skill of the SEARCH Sea Ice Outlook 20082013. *Geophysical Research Letters*, **41**(7), 2411–2418.

STROEVE, J. C., KATTSOV, V., BARRETT, A., SERREZE, M., PAVLOVA, T., HOLLAND, M., & MEIER, W. N. 2012. Trends in Arctic sea ice extent from CMIP5, CMIP3 and observations. *Geophysical Research Letters*, **39**(16).

TAYLOR, P. D., & FELTHAM, D. L. 2004. A model of melt pond evolution on sea ice. *Journal of Geophysical Research: Oceans*, **109**(C12).

THORNDIKE, A. S., ROTHROCK, D. A., MAYKUT, G. A., & COLONY, R. 1975. The thickness distribution of sea ice. *Journal of Geophysical Research (1896-1977)*, **80**(33), 4501–4513.

TREMBLAY, L.-B., & MYSAK, L. A. 1997. Modeling Sea Ice as a Granular Material, Including the Dilatancy Effect. *Journal of Physical Oceanography*, **27**(11), 2342–2360.

TSAMADOS, M., FELTHAM, D. L., SCHROEDER, D., FLOCCO, D., FARRELL, S. L., KURTZ, N., LAXON, S. W., & BACON, S. 2014. Impact of Variable Atmospheric and Oceanic Form Drag on Simulations of Arctic Sea Ice. *Journal of Physical Oceanography*, **44**(5), 1329–1353.

TURNER, A. K., & HUNKE, E. C. 2015. Impacts of a mushy-layer thermodynamic approach in global sea-ice simulations using the CICE sea-ice model. *Journal of Geophysical Research: Oceans*, **120**(2), 1253–1275.

UNGERMANN, M., & LOSCH, M. 2018. An Observationally Based Evaluation of Subgrid Scale Ice Thickness Distributions Simulated in a Large-Scale Sea Ice-Ocean Model of the Arctic Ocean. *Journal of Geophysical Research: Oceans*, **123**(11), 8052–8067.

UNGERMANN, M., TREMBLAY, L. B., MARTIN, T., & LOSCH, M. 2017. Impact of the ice strength formulation on the performance of a sea ice thickness distribution model in the Arctic. *Journal of Geophysical Research: Oceans*.

VAN DER WALT, S., SCHÖNBERGER, J. L., NUNEZ-IGLESIAS, J., BOULOGNE, F., WARNER, J. D., YAGER, N., GOUILLART, E., & YU, T. A. 2014. scikit-image: image processing in Python. *PeerJ*, **2**(June), e453.

VAN DYNE, M., & TSATSOULIS, C. 1993. Extraction and analysis of sea ice leads from SAR images. *Proceedings Geoscience and Remote Sensing Symposium*, **2**, 629631.

VAN DYNE, M., TSATSOULIS, C., & FETTERER, F. 1998. Analyzing lead information from SAR images. *IEEE Transactions on Geoscience and Remote Sensing*, **36**, 647–660.

WALES, D. J., & DOYE, J. P. K. 1997. Global Optimization by Basin-Hopping and the Lowest Energy Structures of Lennard-Jones Clusters Containing up to 110 Atoms. *The Journal of Physical Chemistry A*, **101**(28), 5111–5116.

WALTER, B. A., & OVERLAND, J. E. 1993. The response of lead patterns in the Beaufort Sea to storm-scale wind forcing. *Annals of Glaciology*, **17**, 219–226.

WANG, K. 2007. Observing the yield curve of compacted pack ice. *Journal of Geophysical Research: Oceans*, **112**(C5).

WANG, Q., DANILOV, S., JUNG, T., KALESCHKE, L., & WERNECKE, A. 2016. Sea ice leads in the Arctic Ocean: Model assessment, interannual variability and trends. *Geophysical Research Letters*, **43**(13), 7019–7027.

WEISS, J. 2017. Exploring the solid turbulence of sea ice dynamics down to unprecedented small scales. *Journal of Geophysical Research: Oceans*, **122**(8), 6071–6075.

WEISS, J., & DANSEREAU, V. 2017. Linking scales in sea ice mechanics. *Philosophical Transactions of the Royal Society of London A: Mathematical, Physical and Engineering Sciences*, **375**(2086).

WEISS, J. 2013. Sea Ice Deformation. *Pages 31–51 of: Drift, Deformation, and Fracture of Sea Ice.* SpringerBriefs in Earth Sciences. Springer Netherlands.

WEISS, J. 2003. Scaling of Fracture and Faulting of Ice on Earth. *Surveys in Geophysics*, **24**(2), 185–227.

WERNECKE, A., & KALESCHKE, L. 2015. Lead detection in Arctic sea ice from CryoSat-2: quality assessment, lead area fraction and width distribution. *The Cryosphere*, **9**(5), 1955–1968.

WILCHINSKY, A. V., & FELTHAM, D. L. 2004. A continuum anisotropic model of sea-ice dynamics. *Proceedings of the Royal Society of London. Series A: Mathematical, Physical and Engineering Sciences*, **460**(2047), 2105–2140.

154

WILLIAMS, J., & TREMBLAY, L. B. 2018. The dependence of energy dissipation on spatial resolution in a viscous-plastic sea-ice model. *Ocean Modelling*, **130**, 40 – 47.

WILLMES, S., & HEINEMANN, G. 2016. Sea-Ice Wintertime Lead Frequencies and Regional Characteristics in the Arctic, 2003-2015. *Remote Sensing*, **8**(1).

ZHANG, J., & HIBLER, W. D. 1997. On an efficient numerical method for modeling sea ice dynamics. *Journal of Geophysical Research: Oceans*, **102**(C4), 8691–8702.

ZHANG, J., THOMAS, D. R., ROTHROCK, D. A., LINDSAY, R. W., YU, Y., & KWOK, R. 2003. Assimilation of ice motion observations and comparisons with submarine ice thickness data. *Journal of Geophysical Research: Oceans*, **108**(C6).

ZHANG, T. Y., & SUEN, C. Y. 1984. A Fast Parallel Algorithm for Thinning Digital Patterns. *Commun. ACM*, **27**(3), 236–239.